An Analysis of Three Path-Integral Based Approximations to Quantum Dynamics

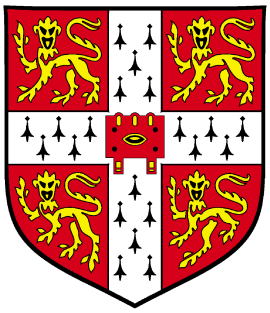

Sundeep Popat

Homerton College
University of Cambridge

A thesis submitted for the degree of Doctor of Philosophy

February, 2021

Declaration

This thesis is the result of my own work and includes nothing which is the outcome of work done in collaboration except where specifically indicated in the text. The number of words in this thesis does not exceed the limit set by the Degree Committee. It is not substantially the same as any that I have submitted, or, is being concurrently submitted for a degree or diploma or other qualification at the University of Cambridge or any other university or similar institution.

Sundeep Popat
February 2021

An Analysis of Three Path-Integral Based Approximations to Quantum Dynamics

Sundeep Popat

Simulating the motion of atoms and molecules is a challenging problem, especially when the dynamics of the atomic nuclei need to be treated quantum mechanically. In this thesis we analyse three path-integral based approximations for computing quantum time-correlation functions: constant-uncertainty molecular dynamics (CUMD), the fitted harmonic approximation (FHA) and windowed centroid molecular dynamics (WCMD).

The CUMD method has been proposed as a simple and efficient method to incorporate nuclear quantum effects in molecular simulations. The method applies a position-momentum constraint between system replicas based on the uncertainty principle. After reproducing the results from the original publication, we show that the method uses an ad hoc fix to apply the constraint which makes it impractical when extended to systems larger than toy models.

The FHA is proposed in this work as a locally harmonic approximation to the linearised-semi classical initial value representation. We find that the FHA results in time correlation functions which are similar to and in some cases better than those obtained from the local gaussian approximation (LGA). In its current implementation, the FHA method is a proof of principle which has been applied to test systems in one and two dimensions, but the results obtained are sufficiently promising to suggest that future implementations of the FHA could compete with the LGA.

The WCMD method is proposed in this work as a simple method for removing contributions from delocalised ring polymers in centroid molecular dynamics calculations, in which they are known to cause artificial red shifts in vibrational spectra. We apply the WCMD method to two dimensional test systems and find that by filtering out the delocalised ring polymers we are able to eliminate the artificial red shift. This result is extremely promising and suggests that the WCMD method should be extendable in future work to treat systems such as gas phase and liquid water.

Acknowledgements

I am grateful to Professor Stuart Althorpe for his guidance and supervision. I would like to thank members of the Althorpe group for insightful discussions. I acknowledge funding from the EPSRC Centre for Doctoral Training in Computational Methods for Materials Science.

On a personal note, I am profoundly grateful to my mum (Shilpa) and dad (Nilesh) for their unwavering support of my academic endeavours, my sister for understanding my struggles and offering moral support and my brother and his family for encouragement and being there to talk to and take my mind off work. I am also grateful to my friends from College and the department who made my experience at Cambridge a more enjoyable one.

Abbreviations

DVR	Discrete Variable Representation
MCTDH	Multi-Configuration Time Dependent Hartree
PIMD	Path-Integral Molecular Dynamics
PIMC	Path-Integral Monte Carlo
MD	Molecular Dynamics
ZPE	Zero-Point Energy
LSC-IVR	Linearised Semiclassical Initial Value Representation
RPMD	Ring-Polymer Molecular Dynamics
CMD	Centroid Molecular Dynamics
QCMD	Quasi-Centroid Molecular Dynamics
CUMD	Constant-Uncertainty Molecular Dynamics
FHA	Fitted Harmonic Approximation
LGA	Local Gaussian Approximation
LHA	Local Harmonic Approximation
WCMD	Windowed Centroid Molecular Dynamics
FB	Free Beads
NC	No Constraint
KCL	Classical Kinetic Energy
KQM	Quantum Kinetic Energy
KQMV	Virial Estimate of Quantum Kinetic Energy
TCF	Time-Correlation Function
ACMD	Adiabatic Centroid Molecular Dynamics
AWCMD	Adiabatic Windowed Centroid Molecular Dynamics

Contents

Chapter 1

Introduction

Computational simulations have become widespread in areas of chemistry, physics and materials science.[1] These simulations aim to calculate either static properties (e.g. heat capacities) or dynamical properties (e.g. infrared spectra or reaction rates) with the ultimate aim of being able to interpret and guide experiments.

Classical molecular dynamics (MD) simulations are one of the most widely used techniques and are often successful in reproducing experimental data. However, for light atoms and at low temperatures it becomes increasingly important to treat the nuclear degrees of freedom quantum mechanically.[2; 3] Solving the Schrödinger equation exactly is not possible beyond the simplest toy systems and so we rely on making various approximations to be able to incorporate quantum effects into the motion of atomic nuclei.

Numerical approximations are routinely made to the Schrödinger equation. For example, one can use a finite basis set such as a discrete variable representation (DVR)[4; 5] and exploit the sparsity of the Hamiltonian matrix.[6] Unfortunately, this type of calculation scales exponentially with respect to the number of degrees of freedom and thus becomes impractical beyond small molecular systems.[7; 8] These calculations however can act as a benchmark with which other approximate methods can be compared. Wavepacket-based approximations to the Schrödinger equation such as Gaussian wavepacket[9–13] and multi-configuration time dependent hartree (MCTDH) methods[14–16] are able to treat systems with up to 20 degrees of freedom for short times.

Remarkably, Feynman was able to show that the exact quantum partition function of a system can be represented by that of a classical ring polymer of N replicas of the system with neighbouring replicas connected via temperature dependent harmonic springs in the $N \to \infty$ limit.[17] This representation is often referred to as the 'classical isomorphism' and forms the basis of techniques such as path-

integral molecular dynamics (PIMD) or path-integral Monte Carlo (PIMC), which were first used in the 1980s to calculate quantum statistical properties of molecular systems.[18; 19] Because classical simulations scale linearly with respect to the number of degrees of freedom, path-integral approaches make it possible to include of nuclear quantum effects in systems with hundreds of degrees of freedom, and thus to simulate liquids and solids. For example, for liquid water, $N = 10 - 100$ is usually sufficient to converge most properties of interest which makes the PIMD calculation approximately $10 - 100$ times more expensive than comparable classical MD calculations (which is computationally managable).[20; 21] Various improvements have been made to improve the efficiency and scaling of methods such as PIMD and PIMC, including time-evolution algorithms based on the generalised Langevin equation and the ring-polymer contraction technique.[22; 23] These advances have made the inclusion of quantum effects in the calculation of complex systems much more affordable.[22; 24–27]

The calculation of dynamical properties is a comparatively much more difficult problem relative to that of static properties, since the 'classical isomorphism' applies only to the quantum statistics. The dynamics require the time-evolution of the system to be computed using standard quantum techniques. Since these are impractical for systems with more than a few degrees of freedom (see above), and since it is assumed that most of the quantum effects reside in the statistics, a number of methods have been developed which attempt to approximate the quantum time-correlation functions (TCFs) by combining quantum statistics with classical dynamics.

One such method is the 'classical Wigner' method also known as the linearised semi-classical initial value representation (LSC-IVR).[28–33] The 'classical Wigner' method uses an integral transform called the 'Wigner transform'[34–38] to convert the quantum Boltzmann operator into a quantum phase space distribution, the dynamics of which is evaluated classically.[39–42] This approach is useful in principle because it includes the quantum statistical effects (zero point energy and tunnelling), and one would expect the relatively fast (typically picosecond) decorrelation of the TCF to ensure that the quantum coherence effects in the real time dynamics are small. This approach has two main disadvantages: a technical disadvantage—that the Wigner transform requires a multi-dimensional Fourier transform which in general cannot be done, so in practise one needs to make a further approximation to permit the Wigner transform to be evaluated[43–47]; and a much more serious theoretical failing, that the classical dynamics does not conserve the quantum Boltzmann distribution. The failure to conserve the quantum Boltzmann distribution leads to

the redistribution of energy between inter and intramolecular modes (i.e. the leakage of initially quantized zero point energy)[48] which in simulations can lead to water spontaneously boiling at room temperature.[49] One can tolerate this failing, provided the TCF decays sufficiently rapidly; e.g. in a LSC-IVR description of ice, one can obtain a reasonable infrared spectrum although it shows signs of erroneous melting caused by the non-conservation of the quantum Boltzmann distribution.[50]

Various path-integral dynamics methods which combine quantum statistics and classical dynamics were introduced primarily to redress the non-conservation of the quantum Boltzmann distribution.[51–69] Two of the most commonly used approaches are centroid molecular dynamics (CMD)[70; 71] and ring-polymer molecular dynamics (RPMD),[56; 72] both of which are based on the 'classical isomorphism'. In contrast to LSC-IVR these methods have the advantage of conserving the quantum Boltzmann distribution and satisfying quantum detailed balance. These methods were both formulated in an ad hoc manner and their relation to the exact quantum TCF was not understood until the development of Matsubara dynamics.[73–76] Matsubara dynamics shows that by restricting the space of ring-polymers to a subspace in which they are smooth, the exact quantum propagator becomes classical such that the theory combines quantum statistics and classical dynamics without violating detailed balance. Matsubara dynamics predominantly acts as a theoretical framework owing to a severe 'sign problem' which arises when calculating quantum TCFs. The theory is completely impractical to implement directly and is just as difficult to solve as the time-dependent Schrödinger equation. Starting with Matsubara dynamics, one can derive CMD and RPMD as approximations to it: CMD is a mean-field approximation and RPMD a short-time approximation.[75] Matsubara dynamics has also been used as the starting point to derive other practical approximate methods.[77–79]

Despite their successes, both RPMD and CMD are known to give poor results for correlation functions which involve observables which are non-linear in position (referred to as the 'non-linear operator problem').[62; 80] Furthermore they are also known to have problems in calculations of infrared spectra in systems such as liquid water at room temperature. In RPMD there is known to be a temperature-dependent coupling between the internal modes of the ring polymer; this leads to the presence of spurious peaks and splittings (referred to as the 'spurious-resonance problem').[72] Thermostatted ring polymer molecular dynamics has been developed to overcome this problem,[63; 81] but the propagation of the non centroid modes using the Langevin equation introduces artificial friction into the dynamics of the ring-polymer centroid which leads to the broadening of spectral peaks, in particular

at low temperature. CMD suffers from the 'curvature' problem[82; 83] which produces artificial temperature-dependent red-shifts in the positions of stretch bands in infrared spectra. This curvature problem has been investigated[78; 84] and a new method has been developed (Quasi Centroid Molecular Dynamics - QCMD)[79; 84] which corrects the artificial red-shifts; however QCMD is computationally and algorithmically more difficult to implement than CMD.

In this thesis we analyse three approximate methods for computing quantum time-correlation functions. In Chapter 2 we analyse the constant uncertainty molecular dynamics (CUMD) method[85] which has been presented as a simple and efficient method for including quantum effects in real time trajectories and is based on the position-momentum uncertainty principle. In CUMD, a quantum particle is represented by N particles which are initiated such that the position and momentum distributions of these particles are consistent with the uncertainty principle. The particles are then propagated subject to a constraint which holds the uncertainty constant. We show that the method uses an ad hoc fix to incorporate the constant-uncertainty constraint which makes the method unstable, with trajectories not conserving energy and requiring extremely small time steps. We then take the initial momenta rescaling step of the method and evolve the system replicas using classical dynamics. This works well for toy systems but fails for more realistic test systems.

In Chapter 3 , we develop a new local harmonic approximation, called the fitted harmonic approximation (FHA) to LSC-IVR. We implement this approach on one and two dimensional systems and find that the results obtained are comparable with one of the most widely used harmonic approximations to LSC-IVR, the Local Gaussian approximation (LGA). At its current stage of implementation, the FHA method is not practical as we use the exact wavefunctions to evaluate the Wigner transforms and need to solve nonlinear equations, the number of which scales linearly with the number of degrees of freedom of the system. Nonetheless, this preliminary version of the method serves as a useful proof of principle, by showing that it may be possible to improve on the commonly used LGA method.

In Chapter 4, we develop a path-integral method called windowed centroid molecular dynamics (WCMD). In WCMD we apply a window function to centroid molecular dynamics (CMD) to prevent the formation of delocalised ring polymers which which are responsible for the curvature problem. The window function prevents the spread of the ring polymer in the direction tangential to the motion of the centroid. We apply the window function in two dimensions to the champagne-bottle Morse potential which shows that the method corrects the red shift due to CMD and gives

excellent agreement with quasi-centroid Molecular dynamics (QCMD). The WCMD method is also tested on two angular dependent potentials to further verify the method and comparisons are made with classical dynamics, the exact quantum result and CMD. These are promising results, since the WCMD method should be straightforward to generalise to multi-dimensions where it would provide a cheap alternative to QCMD.

Finally, Chapter 5 concludes the thesis and suggests possible avenues for future work.

The CUMD codes implemented within Chapter 2 were written in Fortran with the 1D constrained simulations calculated with a parallel implementation. The FHA calculations in Chapter 3 were performed using Fortran with the numerical derivatives and interpolation calculated using Python. The WCMD calculations of Chapter 4 were implemented using Fortran.

Chapter 2

Constant-Uncertainty Molecular Dynamics

2.1 Background Theory

2.1.1 Quantum Mechanical Correlation Functions

Calculating quantum real-time correlation functions is a difficult problem, but the calculation of static equilibrium properties is comparatively much easier. This is due to the isomorphism between the path integral representation of a quantum mechanical partition function and the classical partition function of a fictitious ring polymer. The real-time correlation function is of the form[72]

$$C_{AB}(t) = \frac{1}{Z}\,\mathrm{Tr}\Big[e^{-\beta\hat{H}}\hat{A}e^{+i\hat{H}t/\hbar}\hat{B}e^{-i\hat{H}t/\hbar}\Big] \tag{2.1}$$

Eq.(2.1) is often referred to as the 'asymmetric split' correlation function[74] because the Boltzmann operator is placed asymmetrically on one side of $\hat{A}$. By inserting identities, Eq. (2.1) can be represented diagrammatically (Fig.(2.1)) which when $\hat{A}$ and $\hat{B}$ are functions of position only can be written as

$$C_{AB}(t) = \frac{1}{Z}\int dx \int dy \int dz\, \langle x|\, e^{-\beta\hat{H}}\, |y\rangle\, A(y)\, \langle y|\, e^{i\hat{H}t/\hbar}\, |z\rangle\, B(z)\, \langle z|\, e^{-i\hat{H}t/\hbar}\, |x\rangle \tag{2.2}$$

Comparing the forms of the real-time evolution operator $e^{-i\hat{H}t/\hbar}$ with that of the quantum Boltzmann operator $e^{-\beta\hat{H}}$, it can be seen that they take the same form but with time $t = -i\beta\hbar$ in the quantum Boltzmann operator, i.e. the quantum Boltzmann operator can be thought of as taking an imaginary-time path of length

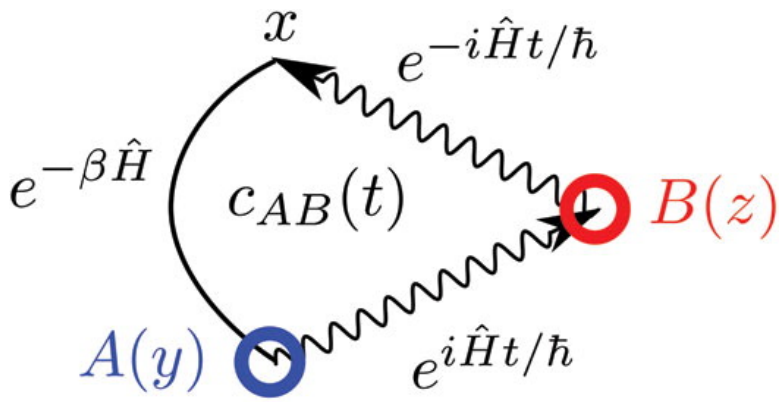

Figure 2.1: Diagrammatic representation of the asymmetric-split correlation function of Eq.(2.2). (Figure reproduced from ref.[74].)

$\beta\hbar$. Starting at point x in Fig.(2.1), we take an imaginary-time path ending at point y, where the quantity $A(y)$ is evaluated. We then take a backward real-time path to the point z, where the quantity $B(z)$ is evaluated. Finally, a forward real time path is taken back to point x which completes the trace. Imaginary-time propagation is represented by the solid curved line and the forward/backward real time propagation by wavy arrows.

Splitting of the Boltzmann operator about $\hat{A}$ gives the Kubo-transformed time correlation function

$$\widetilde{C}_{AB}(t) = \frac{1}{\beta Z}\int_0^\beta d\lambda \ \mathrm{Tr}\left[e^{-\lambda\hat{H}}\hat{A}e^{-(\beta-\lambda)\hat{H}}e^{+i\hat{H}t/\hbar}\hat{B}e^{-i\hat{H}t/\hbar}\right] \tag{2.3}$$

where λ is a variable which indicates that the quantity $\hat{A}$ is evaluated across the ring polymer.

The Kubo-transformed time-correlation function has the same symmetries as a classical correlation function.[72] Furthermore by changing integration limits it can be shown that the Kubo-transformed TCF is always real:

$$\widetilde{C}_{AB}(t) = \widetilde{C}_{AB}(t)^* \tag{2.4}$$

and that it satisfies the detailed balance condition

$$\widetilde{C}_{AB}(t) = \widetilde{C}_{BA}(-t) \tag{2.5}$$

Let the fourier transforms of the standard time-correlation functions and the Kubo-transformed time-correlation functions be

$$C_{AB}(\omega) = \int_{-\infty}^{\infty} e^{-i\omega t}C_{AB}(t)dt \tag{2.6}$$

and

$$\widetilde{C}_{AB}(\omega) = \int_{-\infty}^{\infty} e^{-i\omega t} \tilde{C}_{AB}(t) dt \tag{2.7}$$

respectively. The relation between the two is then given by

$$C_{AB}(\omega) = \frac{\beta\hbar\omega}{1 - e^{-\beta\hbar\omega}} \widetilde{C}_{AB}(\omega) \tag{2.8}$$

and so knowledge of either one means that the other can be calculated from it.[72] One therefore has a choice of which TCF to calculate, and the Kubo transformed TCF is chosen when developing classical like methods because it shares properties (2.4) and (2.5) with the classical TCF.

2.1.2 Path Integrals - The Classical Isomorphism

Feynman path-integral theory is an alternative but rigorous formulation of quantum theory in which paths are used instead of wavefunctions. Here we consider imaginary time path integrals. which give a powerful way of simulating quantum static properties which resemble classical MD in an extended phase space.[86]

The quantum partition function for the NVT ensemble is given by the expression:

$$Z(\beta) = \sum_n e^{-\beta E_n} \tag{2.9}$$

where the energy levels E_n are the solutions of the time independent Schrödinger equation $\hat{H}\,|n\rangle = E_n\,|n\rangle$ and β is the inverse temperature $1/(k_b\mathrm{T})$. For anything other than toy systems, evaluating $Z(\beta)$ by calculating all of the energy levels of the system is not possible and so alternative approaches are required, one of which is the path-integral approach. We restrict the theory here to one dimension (1D) to simplify the algebra, but the following can be generalised straightforwardly to multi-dimensions. The 1D Hamiltonian of a system is of the form

$$\hat{H} = \hat{p}^2/2m + \hat{V} \tag{2.10}$$

with m being the mass of the system, $\hat{V} = V(x)$ the potential energy and $\hat{p} = -i\hbar\frac{\partial}{\partial x}$ the momentum operator. The partition function can be defined equivalently as

$$Z(\beta) = \mathrm{Tr}\left[e^{-\beta\hat{H}}\right] \tag{2.11}$$

where the trace (Tr) is the sum of the diagonal elements of the matrix. Eq. (2.11) reduces to Eq. (2.9) in the basis set of eigenstates of the Hamiltonian $|n\rangle$. However

Eq. (2.11) can be expanded in any complete set of basis states. For example in the position representation

$$Z(\beta) = \int_{-\infty}^{\infty} dx \, \langle x | \, e^{-\beta \hat{H}} \, | x \rangle \tag{2.12}$$

The kinetic energy part of the total Hamiltonian can be evaluated in the momentum representation and the potential energy part can be evaluated in the position representation respectively.

$$e^{-\beta \hat{p}^2/2m} \, |p\rangle = e^{-\beta p^2/2m} \, |p\rangle \tag{2.13}$$

$$e^{-\beta \hat{V}} \, |x\rangle = e^{-\beta V(x)} \, |x\rangle \tag{2.14}$$

The total Hamiltonian cannot be evaluated in either the position or momentum representations as $\hat{p}$ and $\hat{V}$ do not commute. Therefore an approximation to the Boltzmann operator is made called the split-operator method or Trotter splitting. Writing $\hat{T} = \hat{p}^2/2m$, the density matrix is

$$\langle x' | \, e^{-\beta \hat{H}} \, | x \rangle \approx \langle x' | \, e^{-\beta \hat{V}/2} e^{-\beta \hat{T}} e^{-\beta \hat{V}/2} \, | x \rangle \tag{2.15a}$$

$$= e^{-\beta V(x')/2} \, \langle x' | \, e^{-\beta \hat{T}} \, | x \rangle \, e^{-\beta V(x)/2} \tag{2.15b}$$

Note that Eq.(2.15a) is not an equality as $\hat{T}$ and $\hat{V}$ do not commute; it is an approximation that simplifies the problem but introduces an error $\mathcal{O}(\beta^3)$.

Using the identity operator for the momentum eigenstates,

$$\int_{-\infty}^{\infty} dp \, |p\rangle \, \langle p| = 1 \tag{2.15c}$$

Eq. (2.15b) becomes

$$\begin{aligned} & e^{-\beta V(x')/2} \, \langle x' | \, e^{-\beta \hat{T}} \, | x \rangle \, e^{-\beta V(x)/2} \\ = & \int_{-\infty}^{\infty} dp \, \langle x' | \, e^{-\beta \hat{T}} \, | p \rangle \, \langle p | x \rangle \, e^{-\beta [V(x') + V(x)]/2} \end{aligned} \tag{2.15d}$$

$$= \int_{-\infty}^{\infty} dp \, \langle x' | p \rangle \, e^{-\beta p^2/2m} \, \langle p | x \rangle \, e^{-\beta [V(x') + V(x)]/2} \tag{2.15e}$$

Using the relation $\langle x | p \rangle = \frac{1}{\sqrt{2\pi\hbar}} e^{ipx/\hbar}$, we obtain

$$\begin{aligned} & \int_{-\infty}^{\infty} dp \, \langle x' | p \rangle \, e^{-\beta p^2/2m} \, \langle p | x \rangle \, e^{-\beta [V(x') + V(x)]/2} \\ = & \frac{1}{2\pi\hbar} \int_{-\infty}^{\infty} dp \; e^{-\beta p^2/2m} e^{ip(x'-x)/\hbar} e^{-\beta [V(x') + V(x)]/2} \end{aligned} \tag{2.15f}$$

$$= \frac{1}{2\pi\hbar}\int_{-\infty}^{\infty} dp\; e^{[(i\sqrt{\frac{\beta}{2m}}p+\sqrt{\frac{m}{2\beta\hbar^2}}(x'-x))^2-\frac{m}{2\beta\hbar^2}(x'-x)^2]}e^{-\beta[V(x')+V(x)]/2} \tag{2.15g}$$

$$= \frac{1}{2\pi\hbar}\int_{-\infty}^{\infty} dp\; e^{-\beta p^2/2m}e^{\frac{-m}{2\beta\hbar^2}(x'-x)^2}e^{-\beta[V(x')+V(x)]/2} \tag{2.15h}$$

$$= \sqrt{\frac{m}{2\pi\beta\hbar^2}}e^{\frac{-m}{2\beta\hbar^2}(x'-x)^2-\beta[V(x')+V(x)]/2} \tag{2.15i}$$

where we have changed the momentum variables to $p = p + 2im(x' - x)/\beta\hbar$ and shifted the integration contour onto the real axis between (2.15g) and (2.15h). In order to calculate the quantum trace, the Boltzmann operator is factorised and a complete set of states inserted over which we can integrate. Repeating this procedure $N - 1$ times, the partition function can be written as

$$\begin{aligned} Z(\beta) = &\int_{-\infty}^{\infty} dx_1 \int_{-\infty}^{\infty} dx_2 \cdots \int_{-\infty}^{\infty} dx_N \,\langle x_1|\, e^{-\beta_N \hat{H}}\,|x_2\rangle \\ &\langle x_2|\, e^{-\beta_N \hat{H}}\,|x_3\rangle \;\ldots \langle x_{N-1}|\, e^{-\beta_N \hat{H}}\,|x_N\rangle \,\langle x_N|\, e^{-\beta_N \hat{H}}\,|x_1\rangle \end{aligned} \tag{2.16}$$

where $\beta_N = \beta/N$. The error is $\mathcal{O}(\beta_N^3)$ and hence the overall error in Z is $\mathcal{O}(\beta_N^2)$ ensuring that Eq. (2.16) gives the exact partition function in the limit $N \to \infty$. The partition function can therefore be written in the form

$$Z(\beta) \approx \left(\frac{m}{2\pi\beta_N\hbar^2}\right)^{N/2} \int d\mathbf{x}\, e^{-\beta_N U_N(\mathbf{x})} \tag{2.17}$$

where $\mathbf{x} = (x_1, x_2, \ldots, x_N)$ and

$$U_N(\mathbf{x}) = \sum_{i=1}^{N}\left[\frac{m}{2\beta_N^2\hbar^2}(x_i - x_{i-1})^2 + V(x_i)\right] \tag{2.18}$$

This sum is cyclic i.e. $x_0 = x_N$ as a result of representing a quantum trace. The partition function given in Eq.(2.17) is equivalent to to a classical partition function for an extended system with the hamiltonian of the system given by

$$\hat{H}_N(\mathbf{p},\mathbf{x}) = \sum_{i=1}^{N}\frac{p_i^2}{2m} + U_N(\mathbf{x}) \tag{2.19}$$

This describes a 'ring polymer' or 'necklace' of N beads which are connected together via temperature-dependent harmonic springs. The representation of a quantum Boltzmann distribution system in this way is known as the classical isomorphism.[17] The springs act to pull together neighbouring beads within the ring polymer whereas the external potential $V(x)$ acts individually on each bead. In the high temperature

limit, the springs become very strong, which reduces the radius of gyration of the polymer and causes the beads to 'shrink' to a single point. Therefore the dynamics of the polymer tend towards the dynamics of a classical particle ($N = 1$). In the low temperature regime the beads are more weakly held together and so the radius of gyration increases allowing for a larger range of configurations. This 'swelling' is analogous to quantum effects becoming of greater importance at lower temperatures as the uncertainty in the position of the particle increases. In the limit of $N \to \infty$ this ring-polymer representation tends towards the exact Feynman path integral representation; in practise a value of N has to be chosen which gives results to a required level of accuracy.

2.1.3 Ring-Polymer Molecular Dynamics

Ring-polymer molecular dynamics (RPMD)[87] is one of the simplest and most widely used approximations to quantum dynamics at present.[62] The method has been tested on a large number of systems and to date is one of the most successful methods for combining quantum statistics with classical dynamics, although it has some serious drawbacks (see below).

The idea behind RPMD is to evolve the N-bead ring polymer using classical dynamics, i.e. to carry out a classical simulation in the extended ring-polymer phase space $(\mathbf{p}, \mathbf{q})$. As such, the RPMD equations of motion can be written as

$$\dot{\mathbf{p}} = -\frac{\partial \hat{H}_N(\mathbf{p},\mathbf{x})}{\partial \mathbf{x}}, \qquad \dot{\mathbf{q}} = +\frac{\partial \hat{H}_N(\mathbf{p},\mathbf{x})}{\partial \mathbf{p}} \tag{2.20}$$

where the Hamiltonian, $\hat{H}_N(\mathbf{p},\mathbf{x})$ is given in Eq.(2.19) above. The TCF can then be written as

$$\tilde{C}_{AB}(t) = \frac{1}{(2\pi\hbar)^N Z_N} \int d^N\mathbf{p}(0) \int d^N\mathbf{x}(0)\; e^{-\beta_N H_N(\mathbf{p}(0),\mathbf{x}(0))} A_N(\mathbf{x}(0)) B_N(\mathbf{x}(t)) \tag{2.21}$$

where the functions $A_N(\mathbf{x}(0))$ and $B_N(\mathbf{x}(t))$ are averaged over the ring polymer beads, denoted by i, at times 0 and t respectively:

$$A_N(\mathbf{x}) = \frac{1}{N}\sum_{i=1}^{N} A(x_i), \qquad B_N(\mathbf{x}) = \frac{1}{N}\sum_{i=1}^{N} B(x_i) \tag{2.22}$$

The RPMD correlation function of Eq.(2.21) is simply the classical correlation function in the extended phase space of the ring polymer of N beads. The method has been shown to agree with the exact quantum result in certain limits. These

include the high temperature limit, the short time limit, the harmonic limit and the static equilibrium limit. The last of these is important as it confirms that the fictitious classical dynamics of the ring-polymer is consistent with the quantum Boltzmann distribution.

Despite the successes of the method one of the main drawbacks associated with RPMD is the spurious resonances that it gives in vibrational spectra. If we consider the ring polymer in a harmonic potential, the centroid or centre of mass of this ring polymer will oscillate at the harmonic frequency, however the other normal modes of the ring polymer oscillate at higher frequencies which are dependent on the temperature and number of beads in the simulation. These higher frequencies are artificial and arise due to the extended phase space and contaminate spectra in the region describing high frequency vibrational peaks by causing spurious temperature dependent peaks.[62]

2.2 Constant-Uncertainty Molecular Dynamics

The CUMD method[85] is based on one of the fundamental ideas of quantum mechanics—the uncertainty principle between position and momentum. The basic idea is to apply a constant-uncertainty constraint to the equations of motion for an ensemble of classical systems, in order to take into account the quantum nature in the real-time evolution. The method was found to generate approximate Kubo-transformed position autocorrelation functions for model potentials that were in better agreement than RPMD with the exact quantum results.

We consider an ensemble of N replicas of a 1D system, each of mass m being acted on by a potential $V(x)$. The time evolution of each of the replicas is described using Hamilton's equations,

$$\dot{p_i} = -\frac{\partial V(q_i)}{\partial q_i}, \qquad \dot{q_i} = \frac{p_i}{m} \tag{2.23}$$

where $i = 1, 2, \ldots, N$ labels the replicas. The ensemble average of the function $A(p, q)$ at time t is defined as

$$\langle A \rangle (t) = \langle A \rangle (\mathbf{p}^0, \mathbf{q}^0, t) = \frac{1}{N} \sum_{i=1}^{N} A(p_i(p_i^0, q_i^0, t), q_i(p_i^0, q_i^0, t)) \tag{2.24a}$$

where

$$\mathbf{p}^0 = (p_1^0, p_2^0, \ldots, p_N^0) \tag{2.24b}$$

and

$$\mathbf{q}^0 = (q_1^0, q_2^0, \ldots, q_N^0) \tag{2.24c}$$

and the superscript 0 denotes time $t = 0$. The uncertainty of the ensemble of the classical particles is defined to be the Schrödinger uncertainty principle.[88]

$$g(t) = \left(\left\langle p^2 \right\rangle (t) - (\langle p \rangle (t))^2\right) \left(\left\langle q^2 \right\rangle (t) - (\langle q \rangle (t))^2\right) - (\langle pq \rangle (t) - \langle p \rangle (t) \langle q \rangle (t))^2 \tag{2.25a}$$

$$= \mathrm{Var}(p)\mathrm{Var}(q) - (\mathrm{Cov}(p, q))^2 \tag{2.25b}$$

where $\langle ... \rangle$ denotes the ensemble average over N replicas. Clearly the Schrödinger uncertainty is a generalisation of the Heisenberg uncertainty $\mathrm{Var}(p)\mathrm{Var}(q)$ which includes the correlation between position and momenta. The Schrödinger's uncertainty principle is

$$g(t) = \mathrm{Var}(p)\mathrm{Var}(q) - (\mathrm{Cov}(p, q))^2 \geq \hbar^2/4 \tag{2.26}$$

It is trivial to show that if the Schrödinger uncertainty principle is satisfied then the Heisenberg uncertainty principle is also satisfied. We note that the uncertainty is usually defined to be the standard deviation (i.e. the square root of the variance), whereas in CUMD it is defined to be the variance.

The uncertainty condition Eq. (2.26) will not necessarily be satisfied by an ensemble of particles which are evolved using classical dynamics. Consequently, a modified version of classical dynamics is used in which the uncertainty constraint is imposed upon the dynamics of the system replicas. The Schrödinger uncertainty principle does not give the exact value of the uncertainty at any given time, but states that the value of the uncertainty is at least $\hbar^2/4$. In CUMD one makes the ad hoc assumption that $g(t)$ remains constant throughout the trajectory. This constant-uncertainty constraint is written as

$$g(t) - g(0) = 0 \tag{2.27}$$

where $g(t)$ and $g(0)$ are the values of the uncertainty of the ensemble at time t and 0 respectively (calculated using Eq.(2.25a)). The initialisation of the position and momentum of the N replicas is chosen such that the uncertainty at a given time, averaged over all trajectories takes the minimum value, i.e. it can be written as

$$\langle g(t) \rangle = \langle g(0) \rangle = \hbar^2/4 \tag{2.28}$$

Taking the derivative of the uncertainty constraint with respect to time gives the following equation[85][see Appendix B]

$$\dot{g} = \left(\left\langle p \frac{\partial V}{\partial q} \right\rangle - \langle p \rangle \left\langle \frac{\partial V}{\partial q} \right\rangle \right) \left(\langle q^2 \rangle - \langle q \rangle^2 \right) - \left(\left\langle q \frac{\partial V}{\partial q} \right\rangle - \langle q \rangle \left\langle \frac{\partial V}{\partial q} \right\rangle \right) \left(\langle pq \rangle - \langle p \rangle \langle q \rangle \right) \tag{2.29}$$

Since the time derivative of the constraint is linear with respect to momentum the Lagrange multiplier method is used to apply the constraint.[89] The equations of motion for the constant-uncertainty dynamics can then be written as follows.[85; 90]

$$\begin{aligned} \dot{p_i}^{\mathrm{CU}} = -\frac{\partial V}{\partial q_i^{\mathrm{CU}}} + \lambda \Bigg[& \left(\frac{\partial V}{\partial q_i^{\mathrm{CU}}} - \left\langle \frac{\partial V}{\partial q} \right\rangle^{\mathrm{CU}} \right) \times \left(\langle q^2 \rangle^{\mathrm{CU}} - (\langle q \rangle^{\mathrm{CU}})^2 \right) \\ & - \left(\left\langle q \frac{\partial V}{\partial q} \right\rangle^{\mathrm{CU}} - \langle q \rangle^{\mathrm{CU}} \left\langle \frac{\partial V}{\partial q} \right\rangle \right) \times (q_i^{\mathrm{CU}} - \langle q \rangle^{\mathrm{CU}}) \Bigg] \end{aligned} \tag{2.30a}$$

$$\dot{q}_i^{\mathrm{CU}} = \frac{p_i^{\mathrm{CU}}}{m} \tag{2.30b}$$

where the CU superscript is used to show that the time evolution of the variable obeys Eq. (2.30a) and (2.30b). The Lagrange multiplier, λ, is calculated to satisfy the uncertainty constraint

$$g^{\mathrm{CU}}(t) - g(0) = 0 \tag{2.31}$$

$\langle A \rangle^{\mathrm{CUMD}}(t)$ is defined to be the time-dependent expectation value of A in the CUMD simulation. Which can be written as

$$\langle A \rangle^{\mathrm{CU}}(t) = \langle A \rangle^{\mathrm{CU}}\left(\mathbf{p}^0, \mathbf{q}^0, t\right) = \frac{1}{N}\sum_{i=1}^{N} A\left(p_i^{\mathrm{CU}}\left(\mathbf{p}^0, \mathbf{q}^0, t\right), q_i^{\mathrm{CU}}\left(\mathbf{p}^0, \mathbf{q}^0, t\right)\right) \tag{2.32}$$

where p_i^{CU} and q_i^{CU} are the momenta and positions of the N replicas at time t in the CUMD simulation.

The CUMD approximation to the Kubo-transformed time correlation function is therefore

$$\tilde{C}_{AB}(t) = \frac{1}{(2\pi\hbar)^N Z_N}\int d\mathbf{p}\int d\mathbf{q}\exp(-\beta_N H_N(\mathbf{p},\mathbf{q}))\langle A\rangle(\mathbf{p},\mathbf{q},0)\langle B\rangle^{\mathrm{CU}}(\mathbf{p}^0(\mathbf{p},\mathbf{q},\alpha),\mathbf{q},t) \tag{2.33}$$

where $H_N(\mathbf{p},\mathbf{q})$ is the usual ring-polymer Hamiltonian and Z_N the partition function. A schematic representation of a CUMD calculation is given in Fig. (2.2).

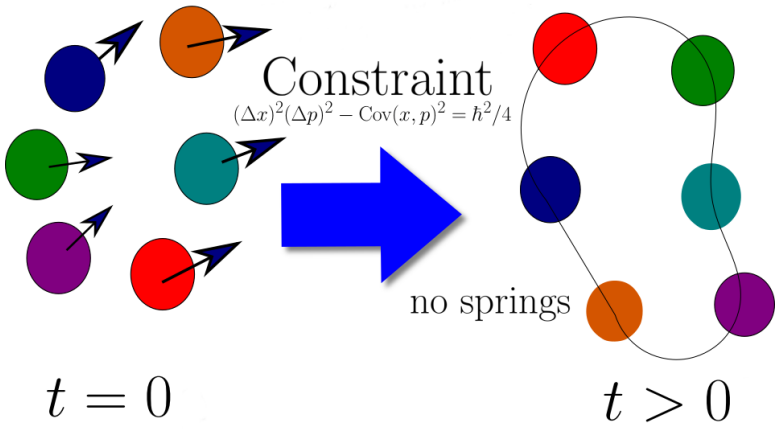

Figure 2.2: Schematic representation of the constant-uncertainty molecular dynamics method. An ensemble of particles is initialised $t = 0$ using a ring polymer to distribute the positions and Eq.(2.35) to distribute the momenta. For $t > 0$, the particles follow classical dynamics subject to a constant-uncertainty constraint in the momentum-position uncertainty.

We break down the CUMD method into three steps: the free beads approximation, the initialisation step (no constraints) and CUMD (i.e. the initialisation with the constraint added).

2.2.1 The Free Beads Method

We begin by making a modification to the RPMD method. After equilibrating the ring polymer at a given temperature, the springs connecting the system replicas are removed and the remaining beads are allowed to evolve classically.[91] We call this the 'free beads' method. The motivation for this modification is to find a simple method that is able to incorporate quantum statistical effects into classical dynamics and that is also efficient and scalable (i.e., a method that does not contain any phase factor or springs connecting system replicas). The idea behind the free-beads method serves as a precursor to the CUMD method and it is useful to understand the differences between the two. In the calculation of the free-beads TCF, the centroid of the ensemble at time zero ($t = 0$) is correlated with the centroid at a later time ($t > 0$).

2.2.2 Initialisation - No Constraint

Before the constraint can be applied in CUMD, the positions and momenta of the initial set of N particles are prepared such that, on average, they satisfy $g(0) = \hbar^2/4$. This is achieved by carrying out an RPMD simulation with N beads and sampling the constant-uncertainty ensemble from the RPMD trajectory. The initial positions of the system replicas in the CUMD ensemble are given as

$$q_i^0 = q_i^{\mathrm{RPMD}} \tag{2.34}$$

where q_i^{RPMD} is the position of the i^{th} bead of the ring polymer. To satisfy the initial condition that $\langle g(0)\rangle = \hbar^2/4$, the initial momenta of the ring-polymer beads are discarded and the following formula is used to calculate the momenta of the ensemble of beads.

$$p_i^0 = \sqrt{\frac{2mK^{CL}}{N}}\frac{\langle p^{\mathrm{RPMD}}\rangle}{|\langle p^{\mathrm{RPMD}}\rangle|} + \alpha s_i \tag{2.35}$$

where

$$s_i = q_{i-1}^{\mathrm{RPMD}} - q_{i+1}^{\mathrm{RPMD}} \tag{2.36}$$

the cyclic boundary condition $q_0^{\mathrm{RPMD}} = q_N^{\mathrm{RPMD}}$ has been applied as with RPMD. The variable α are has pair of solutions

$$\alpha = \pm\sqrt{\frac{2mNK^{QM}}{\mathbf{S}^2}} \tag{2.37}$$

where $\mathbf{S} = (s_1, s_2, ..., s_N)$. The positive solution of α is used in the calculations. In the calculation of the quantum mechanical kinetic energy, K^{QM}, a time average of the centroid virial estimator over the ring-polymer trajectory is used.[92; 93]

$$K^{\mathrm{QM,virial}} = \frac{1}{2N}\sum_{i=1}^{N}(q_i - \langle q \rangle) \cdot \frac{\partial V(q_i)}{\partial q_i} \tag{2.38}$$

Calculating the initial momenta of the N system replicas as in Eq. (2.35) ensures that the expectation value of the kinetic energy is equal to the sum of the quantum mechanical kinetic energy (K^{QM}) plus the instantaneous classical kinetic energy ($K^{\mathrm{CL}} = \left\langle (p^{\mathrm{RPMD}})^2 \right\rangle / 2m$), i.e

$$\frac{\langle (p^0)^2 \rangle}{2m} = K^{\mathrm{QM}} + K^{\mathrm{CL}} \tag{2.39}$$

In other words, the choice of the bead positions and momenta are chosen such that, on average, the minimum uncertainty is satisfied at $t = 0$ (i.e. $\langle g(0) \rangle = \hbar^2/4$). The addition of the constraint ensures that this is also true for $t > 0$ (i.e. $\langle g(t) \rangle = \hbar^2/4$). We refer to the initialisation step with the system replicas evolved using classical dynamics as no constraints (NC).

2.2.3 Constraints

There are different approaches in which molecular dynamics with constraints can be performed. The most well known methods are SHAKE and RATTLE.[1; 89; 94; 95] The SHAKE algorithm is based upon the Verlet Algorithm whereas the RATTLE algorithm is designed for the velocity-Verlet algorithm. The RATTLE algorithm was originally developed by Andersen to implement the dynamics for models with a constraint on the distance between atoms. The method has since been developed for use with more general constraints.[96] The basic idea within the RATTLE algorithm is to approximate the Lagrange multipliers within the equations of motion such that the constraint is satisfied to within a certain tolerance. In practise this is achieved through an iterative procedure in which the Lagrange multiplier is solved to first order after each iteration. This process is repeated until the constraint is satisfied to a given level of accuracy.

For a system with a constraint in the dynamics, the equations of motion can be written as

$$m_i \ddot{x}_i = F_i + G_i = -\nabla_i V(x) - \lambda(t) \nabla_i g(x) \tag{2.40}$$

where F_i are the forces due to the potential $V(x)$ and G_i are the forces due to the

constraint $g(x) = 0$. Application of the velocity-Verlet algorithm to these equations of motion result in the following equations for the updates in position and velocity respectively.[96]

$$x_i(t + \Delta t) = x_i(t) + \dot{x}_i(t)\Delta t + [F_i(t) - \lambda_x(t)\nabla_i g(x(t))] \frac{(\Delta t)^2}{2m_i} \tag{2.41}$$

$$v_i(t+\Delta t) = v_i(t)+[F_i(t)+F_i(t+\Delta t)-\lambda_x(t)\nabla_i g(x(t))-\lambda_v(t+\Delta t)\nabla_i g(x(t+\Delta t))]\frac{(\Delta t)}{2m_i} \tag{2.42}$$

As seen in Eqs.(2.41 and 2.42), the RATTLE algorithm uses a different Lagrange multiplier for the position (λ_x) and velocity updates (λ_v). In ref.[85] it is stated that a 'RATTLE-type' algorithm is used to apply the constraint in CUMD, however it should be noted that the standard RATTLE algorithm described above applies only to constraints which depend on position.

Non-Holonomic Constraints

The Gaussian formulation of classical mechanics[90] (a generalisation of Newtonian mechanics which also includes constraints) enables the study of systems which are subject to holonomic (constraints dependent on particle positions only) or non-holonomic constraints (constraints dependent on particle positions and momenta). The CUMD method deals with a non-holonomic constraint.[90; 97; 98] For a non-holonomic constraint that can be written in the form $g(r, \dot{r}, t) = 0$, the acceleration, $\ddot{r}$, must satisfy

$$\ddot{r}\frac{\partial g}{\partial \dot{r}} + \dot{r}\frac{\partial g}{\partial r} + \frac{\partial g}{\partial t} = 0 \tag{2.43}$$

In this case, the acceleration is constrained to lie on a constant g hypersurface. The unconstrained motion of the system can be written as $m\ddot{r_u} = F$. In the absence of the constraint, the acceleration can leave the constraint hypersurface. Gauss's formulation prevents this from happening by the addition of an acceleration term. This additional term can be expressed in terms of a constraint force[90] F_c

$$\ddot{r}_c = \frac{(F + F_c)}{m} = \frac{F}{m} - \lambda\frac{k}{m} \tag{2.44}$$

where λ is a Lagrange multiplier and k is an additional force term.

Implementation of the Constraint

The RATTLE algorithm can be implemented to treat constraints that depend upon positions of particles only (holonomic constraints). An extension to the RATTLE algorithm to include constraints which depend upon particle momenta (non-holonomic constraints) has been proposed but is limited to constraints which are linear in momenta.[98–100] The integrator for the non-holonomic extension to RATTLE is given as:[99; 100]

$$p_{t+1/2} = p_t - \frac{dt}{2}\left(\frac{\partial V(q_t)}{\partial q} + \mu(q_t)\lambda_t\right) \tag{2.45a}$$

$$q_{t+1} = q_t + \frac{dt}{m}p_{t+1/2} \tag{2.45b}$$

$$0 = \mu(q_t)\frac{p_t}{m} \tag{2.45c}$$

$$p_{t+1} = p_{t+1/2} - \frac{dt}{2}\left(\frac{\partial V(q_{t+1})}{\partial q} + \mu(q_{t+1})\lambda_{t+1}\right) \tag{2.45d}$$

$$0 = \mu(q_{t+1})\frac{p_{t+1}}{m} \tag{2.45e}$$

where the constraint can be written as $\sum_i \mu(q_i)\dot{q}$. The constant-uncertainty constraint is non linear in p and so cannot be treated by the non-holonomic extension to RATTLE. In Sec.(2.3.3) we further discuss the algorithm to treat the constraint in CUMD.

2.3 Tests on One-Dimensional Systems

As described in Sec.(2.2) we break down the CUMD method into three steps, in our analysis of the method below we discuss the results obtained from each of these. The quantum reference calculations in this chapter are calculated using a 1D DVR of Colbert and Miller. [2]. The details of the calculation of the quantum TCF are given in [Appendix A.1].

2.3.1 The Free Beads Approximation

We test the free-beads method as described in Sec.(2.2.1). For the harmonic oscillator ($V(x) = \frac{1}{2}x^2$), we find as expected, the free beads method gives the exact TCF. The TCFs for the mildly anharmonic potential

$$V(x) = \frac{1}{2}x^2 + \frac{1}{10}x^3 + \frac{1}{100}x^4 \tag{2.46}$$

and the strongly anharmonic potential

$$V(x) = \frac{1}{4}x^4 \tag{2.47}$$

exhibit artifactual properties (depicted in Fig.(2.3) and (2.4) respectively). In both figures we see that as N is increased the TCFs diverge.[91] As it can be seen, the method completely fails; this is due to problems with the ring polymer having too much kinetic energy. When the springs are removed, the ensemble of particles are no longer confined to be near each other and so are able to freely move apart. As the ring polymer is being thermostatted at a temperature β_N, rather than β as with the classical simulation, this means that on average, the momenta of some of the beads are too large and the centroid of this ensemble moves too far away from its $t = 0$ value.

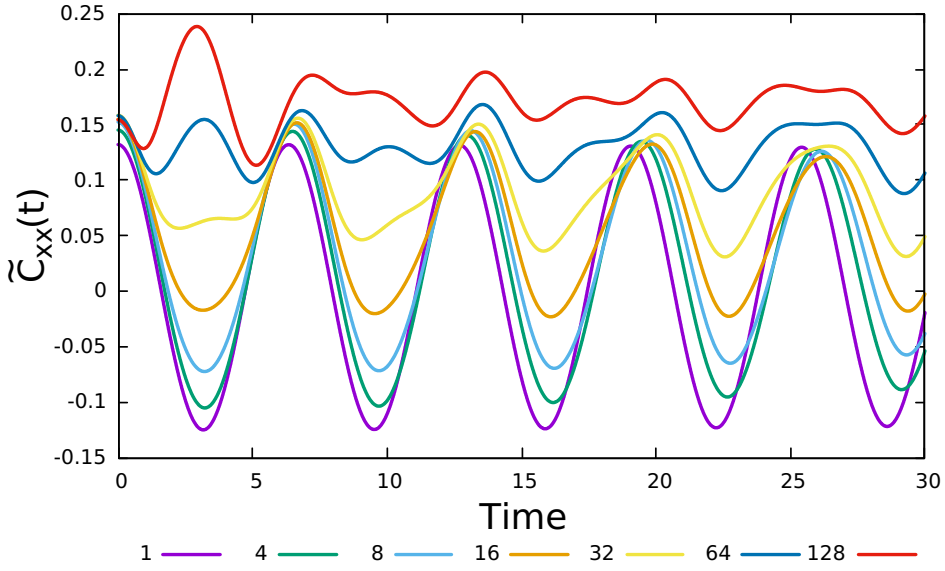

Figure 2.3: Kubo-transformed position TCF for the mildly anharmonic potential of Eq.(2.46) at $\beta = 8$, computed for the free beads method for different numbers of system replicas, N.

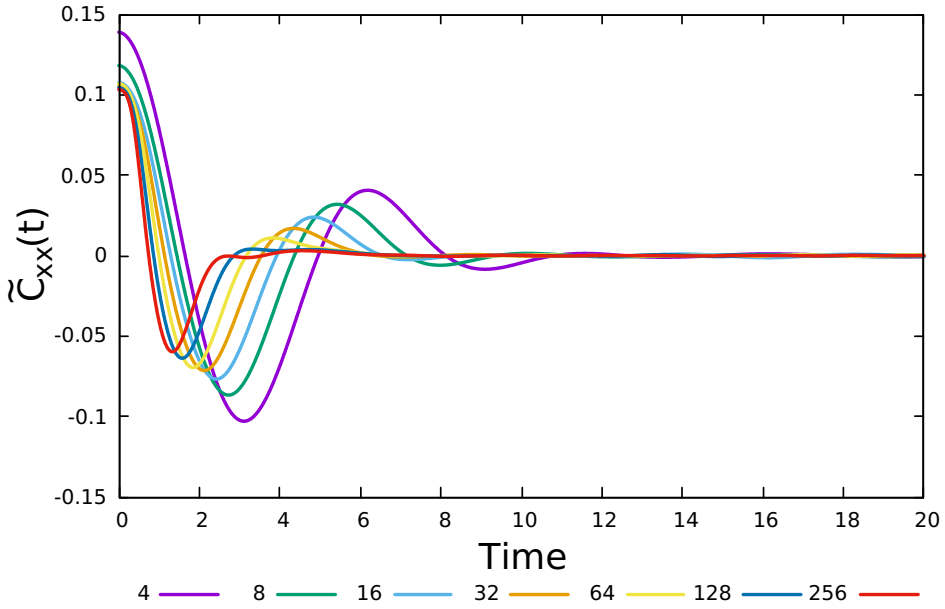

Figure 2.4: Kubo-transformed position TCF for the strongly anharmonic potential of Eq.(2.47) at $\beta = 8$, computed for the free beads method for different numbers of system replicas, N.

2.3.2 No Constraint

The following section describes the initial momenta recalculation step of the CUMD method which we refer to as the no constraint (NC) method. This is the first part of the CUMD method by Hasegawa and differs from the free beads method by using Eq.(2.35) to recalculate the momenta of the individual beads.

The strongly anharmonic Potential

We attempted to reproduce the NC TCF from ref.[85] at temperatures of $\beta = 1$ and $\beta = 8$ for the strongly anharmonic potential. We were able to replicate the result at $\beta = 8$ within graphical accuracy whereas the result for $\beta = 1$ (Fig.(2.5)) shows some disagreement in the TCF at $t > 0$, the amplitude of the TCF calculated in this work decays faster than that of ref.[85], and the two TCFs are out of phase.

After further investigation, it was found that the time averaged virial estimator of the quantum mechanical kinetic energy (KQMV) converges very slowly. Fig.(2.6) shows the convergence of the virial estimator of the quantum mechanical energy for the case of $\beta = 8$ averaged over the number of time steps; it can be seen that at this temperature, evolving for a single thermal time ($= \beta\hbar$) gives a value of KQMV which is approximately equal to that of the converged value. However, for $\beta = 1$, evolving for only a single thermal time in the calculation of the KQMV (Fig(2.7)) does not result in a converged value and leads to an incorrect TCF. Fig.(2.8) shows how the TCF varies as the KQMV is converged; the TCF is converged by 40 thermal times. This slow convergence of the virial estimator results in a significant increase in the computational time when compared to a standard ring-polymer simulation with the same number of beads.

The previous free bead results (Fig.(2.3) and (2.4)) failed to converge with respect to the number of beads. We tested this for the NC result and found that at both high T(Fig.(2.9)) and at low T(Fig.(2.10)) the TCF converges and gives a sensible result. The NC method acts as a filter, removing the spurious momenta from the RPMD distribution. The momenta rescaling prevents the individual beads from moving too far away from each other and so the ensemble of particles are constrained to form a 'blob' which satisfies the uncertainty principle in Eq.(2.26).

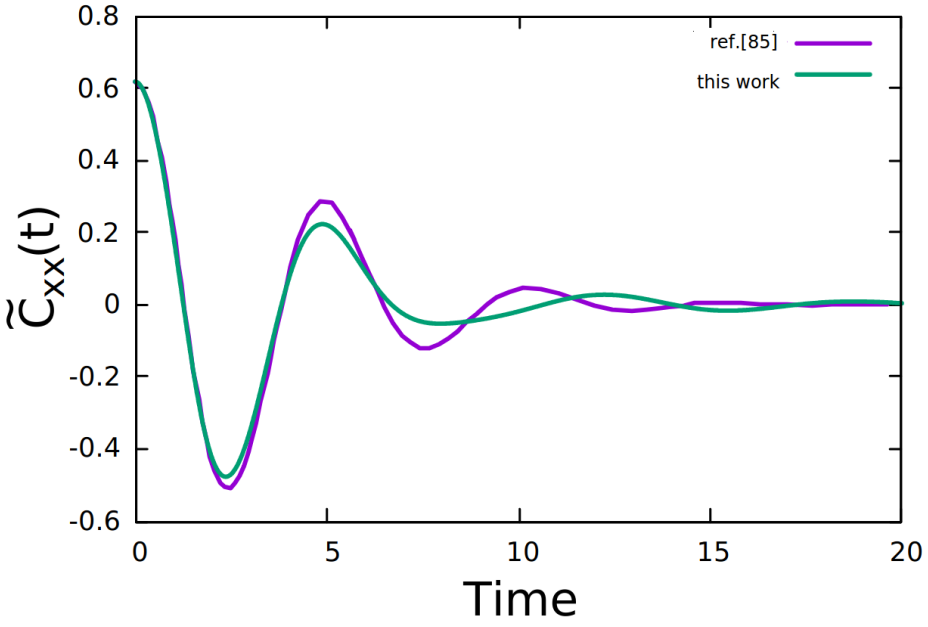

Figure 2.5: Position TCFs for the strongly anharmonic potential at $\beta = 1$ computed using the NC method. KQMV was time averaged over a single thermal time in this work.

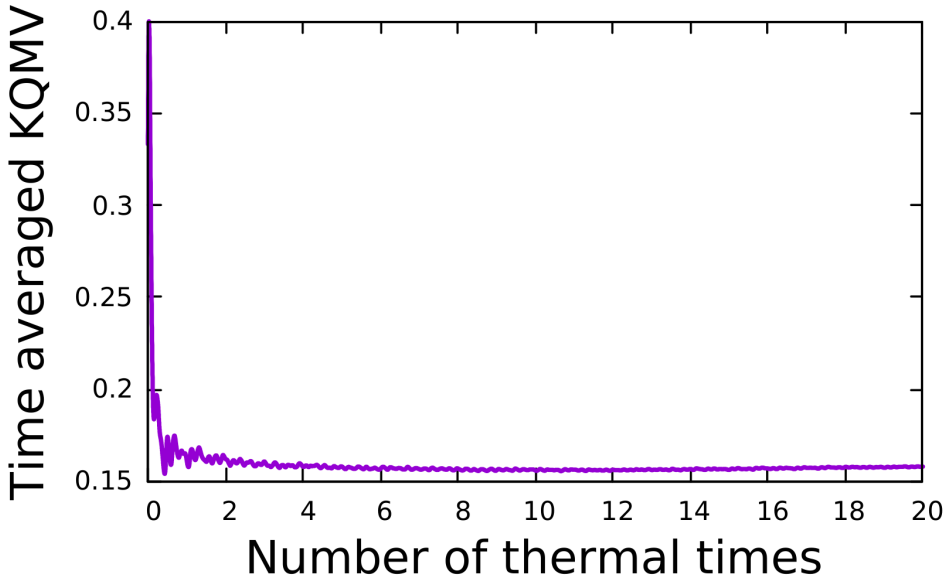

Figure 2.6: Convergence of the time averaged virial estimator of the quantum mechanical kinetic energy (KQMV) with respect to time at $\beta = 8$.

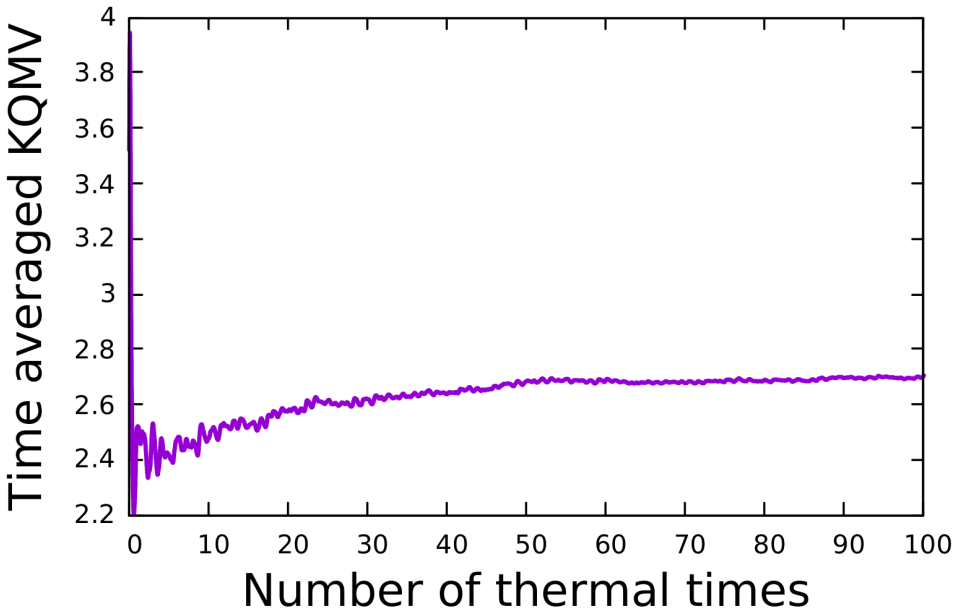

Figure 2.7: Convergence of the time averaged virial estimator of the quantum mechanical kinetic energy (KQMV) with respect to time at $\beta = 1$.

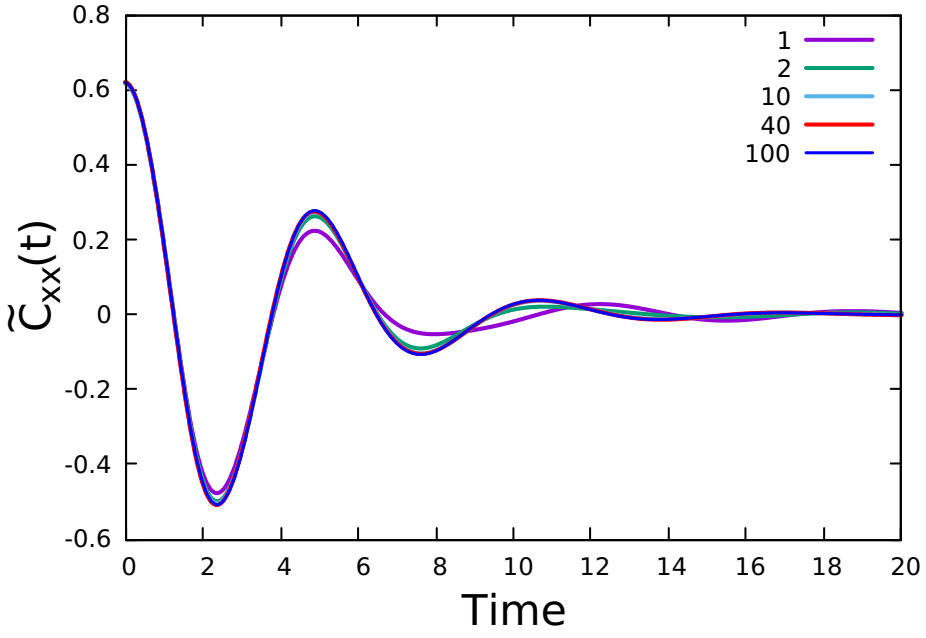

Figure 2.8: Convergence of the position TCF with respect to the number of thermal times that KQMV is time averaged over at $\beta = 1$.

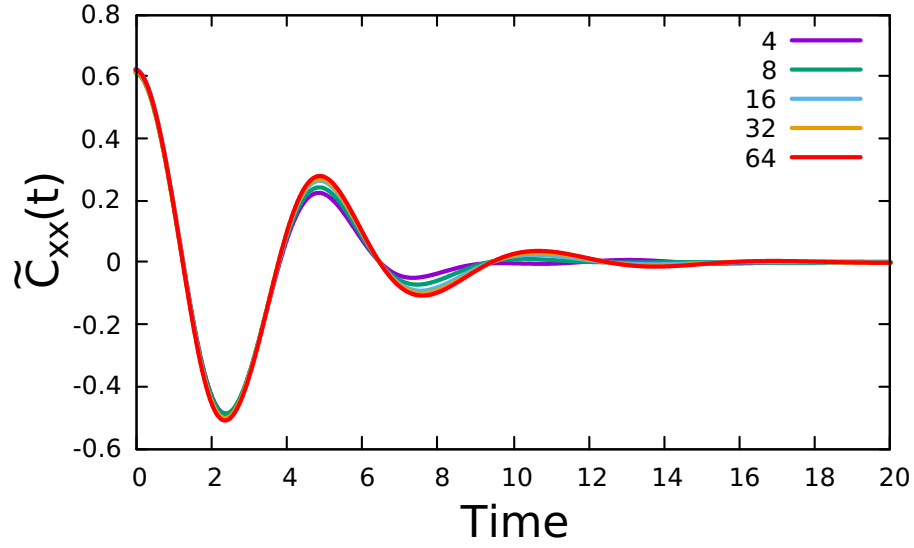

Figure 2.9: Convergence of the position TCF for the NC method with respect to the number of beads for strongly anharmonic potential at $\beta = 1$. For this temperature $N = 32$ is required to converge the TCF.

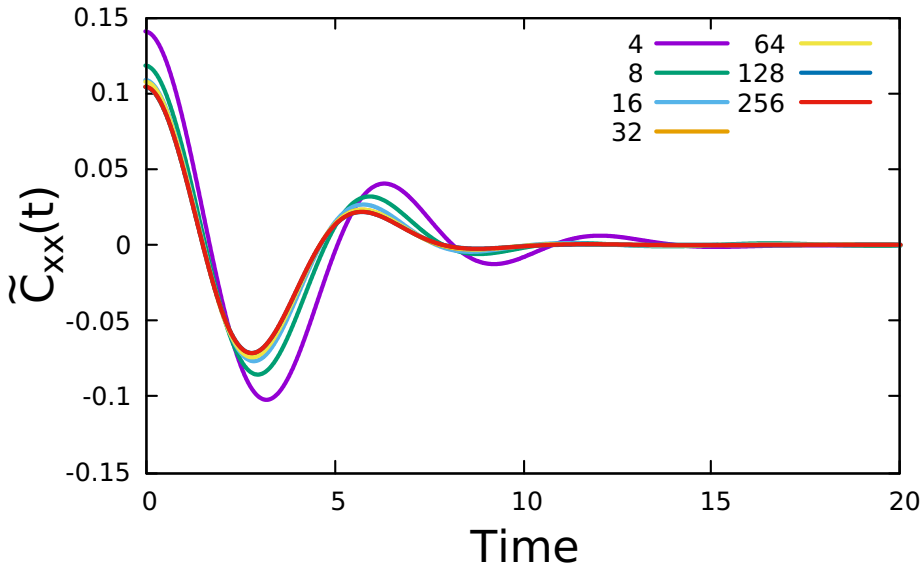

Figure 2.10: Convergence of the position TCF for the NC method with respect to the number of beads for the strongly anharmonic potential at $\beta = 8$. For this temperature $N = 128$ is required to converge the TCF.

The Single Bead Limit

We consider the limit that $N = 1$ in which the 'blob' collapses to a point. First we consider the constraint given by Eq.(2.26). In the limit of one bead, it can be shown that

$$\left\langle p^2 \right\rangle = \left\langle p \right\rangle^2 = p^2 \tag{2.48a}$$

and

$$\left\langle q^2 \right\rangle = \left\langle q \right\rangle^2 = q^2 \tag{2.48b}$$

and

$$\left\langle pq \right\rangle = \left\langle p \right\rangle \left\langle q \right\rangle = pq \tag{2.48c}$$

i.e. the constraint vanishes, and so CUMD reduces to NC in this limit. The momenta rescaling equation of Eq.(2.35) then simplifies to

$$p = \sqrt{p^2} \frac{p}{|p|} = p \tag{2.49}$$

i.e CUMD is equivalent to classical dynamics in the one bead limit.

$N = 2$ calculations

Another interesting simplification for the NC method is to set $N = 2$. For $N = 2$, immediately from Eq. (2.36) it follows that $s_i = 0$. The momenta rescaling equations Eq. (2.35) simplify to:

$$p_i^0 = \sqrt{\frac{2mK^{\mathrm{CL}}}{N}} \frac{\left\langle p^{\mathrm{RPMD}} \right\rangle}{|\langle p^{\mathrm{RPMD}} \rangle|}, \qquad i = 1, 2 \tag{2.50a}$$

$$p_i^0 = \frac{1}{2}\sqrt{p_1^2 + p_2^2} \frac{\left\langle p^{\mathrm{RPMD}} \right\rangle}{|\langle p^{\mathrm{RPMD}} \rangle|} \tag{2.50b}$$

$$p_i^0 = \mathrm{sign}(p_1^{\mathrm{RPMD}} + p_2^{\mathrm{RPMD}}) \frac{1}{2}\sqrt{p_1^2 + p_2^2} \tag{2.50c}$$

i.e., the momenta of both beads are equivalent. These $N = 2$ equations have been tested numerically for the mildly anharmonic potential and the results are shown below in Figs.(2.11-2.14). In the high temperature limit ($\beta = 1$) we see that all the methods tested agree quite well with the exact quantum result (Fig.(2.11)). It is interesting to see that the two bead no constraint result does better than both classical dynamics and RPMD. Fig.(2.12) shows that the position of the NC peak gives the best agreement with the quantum result relative to all of the other approximations and Fig.(2.13) shows that the trough for the two bead NC result matches up slightly better with the quantum result compared to RPMD and classical dynamics. In the low temperature limit, the result is similar to the classical TCF and so does quite poorly (Fig.(2.14)) because N needs to be much larger than 2 to correctly describe the quantum statistics.

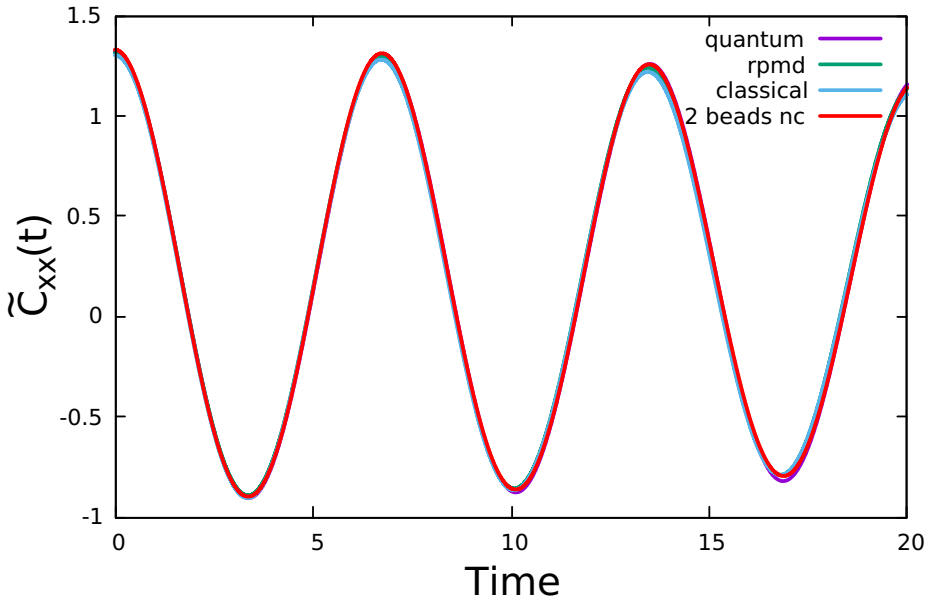

Figure 2.11: Position TCFs computed using $N = 2$ for the NC method (red) at $\beta = 1$ for the mildly anharmonic potential compared with the results of Quantum (purple), RPMD (green) and classical (blue) calculations.

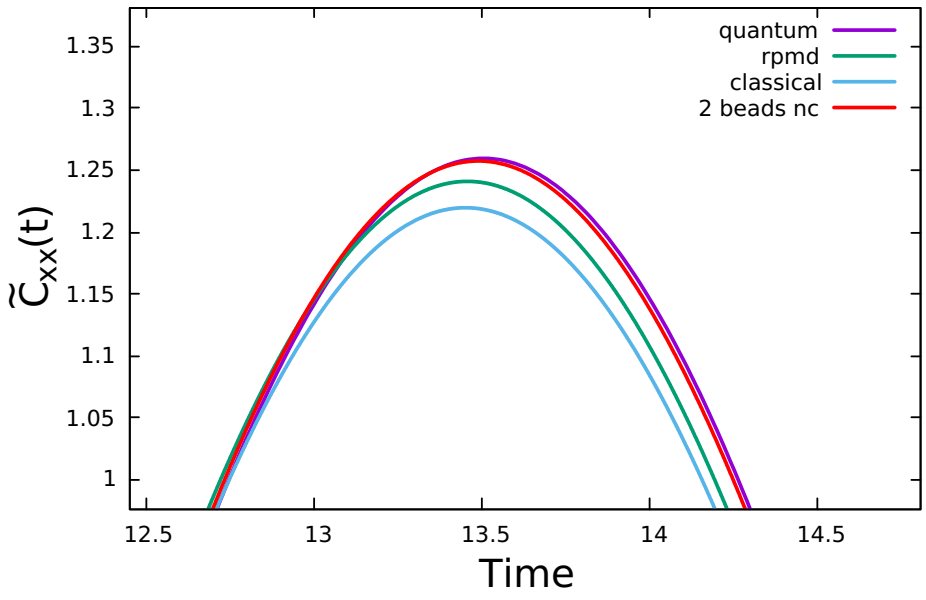

Figure 2.12: Magnified peak of Fig.(2.11) for the mildly anharmonic potential at $\beta = 1$.

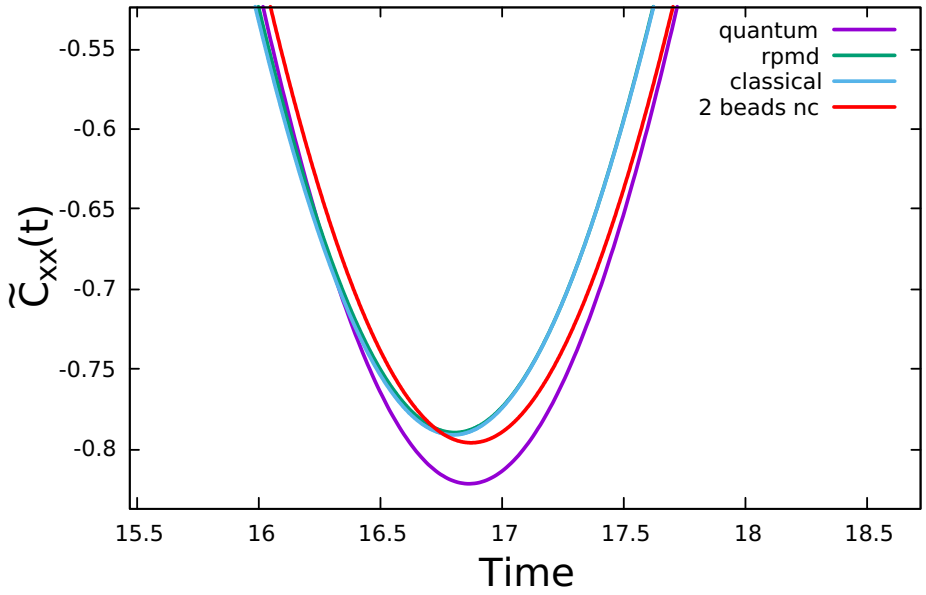

Figure 2.13: Magnified trough of Fig.(2.11) for the mildly anharmonic potential at $\beta = 1$.

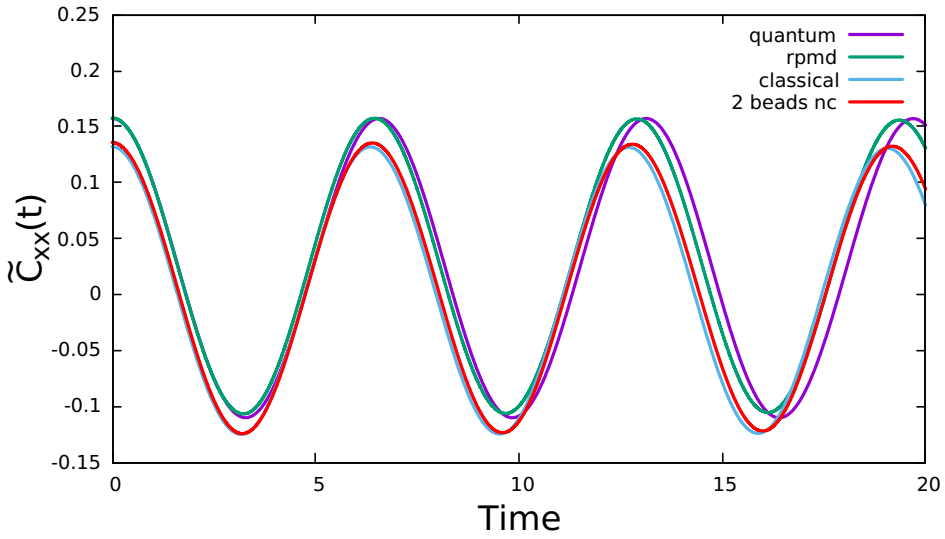

Figure 2.14: Position TCFs computed using $N = 2$ for the NC method (red) at $\beta = 8$ for the mildly anharmonic potential compared with the results of Quantum (purple), RPMD (green) and classical (blue) calculations.

The Harmonic Potential

In the harmonic limit, classical dynamics is exact and the position autocorrelation function can be calculated analytically. In this limit, the evolution of the classical particle can be written as

$$x(t) = x(0)\cos(\omega t) + \frac{p(0)}{m\omega}\sin(\omega t) \tag{2.51}$$

as a result, the position autocorrelation function can be written as

$$\langle x(0)x(t)\rangle = \left\langle x(0)^2\right\rangle \cos(\omega t) + \frac{\langle x(0)p(0)\rangle}{(m\omega)}\sin(\omega t) \tag{2.52}$$

The integral $\langle x(0)p(0)\rangle = 0$ and thus

$$\langle x(0)x(t)\rangle = \left\langle x(0)^2\right\rangle \cos(\omega t) \tag{2.53}$$

Since

$$\left\langle x(0)^2\right\rangle = \frac{1}{Z(2\pi\hbar)}\int dp \int dx \;\; x^2 e^{-\beta H} \tag{2.54}$$

where $H = p^2/(2m) + 1/2m\omega^2 x^2$. It follows that

$$\langle x(0)x(t)\rangle = \frac{\cos(\omega t)}{m\beta\omega^2} \tag{2.55}$$

The same result holds for RPMD in the harmonic limit. The NC method can be thought of as scaling the ring-polymer momenta distribution by α. We let

$$p \to \alpha p \tag{2.56}$$

where α is a constant. We make this substitution in the integral in Eq.(2.51). The factor α can be brought out of the integral as it is a constant, and noting that the partition function Z will also contain this factor, the value of the integral will remain unchanged. As a result, any value of the rescaling factor, α, will also give the correct expression for the TCF in the harmonic limit.

The Mildly Anharmonic Potential

The mildly anharmonic potential was then tested using the NC method, we are also able to converge the TCF with respect to the number of beads for this potential (Fig.(2.15)) shown for $\beta = 1$ (high temperature). The result for the NC method using 256 beads is compared to the classical, RPMD and exact quantum results

(Fig.(2.16)). In the limit $t \to 0$, the NC method is exact as are all the other methods tested. For the NC method the oscillations occur at the correct frequency, however, the troughs are not of the correct amplitude and do slightly worse than classical and RPMD simulations when compared to quantum results (Fig.(2.17)). Hence the NC method gives a modest improvement over RPMD and classical dynamics when considering the amplitudes and positions of the peaks (Fig.(2.18)).

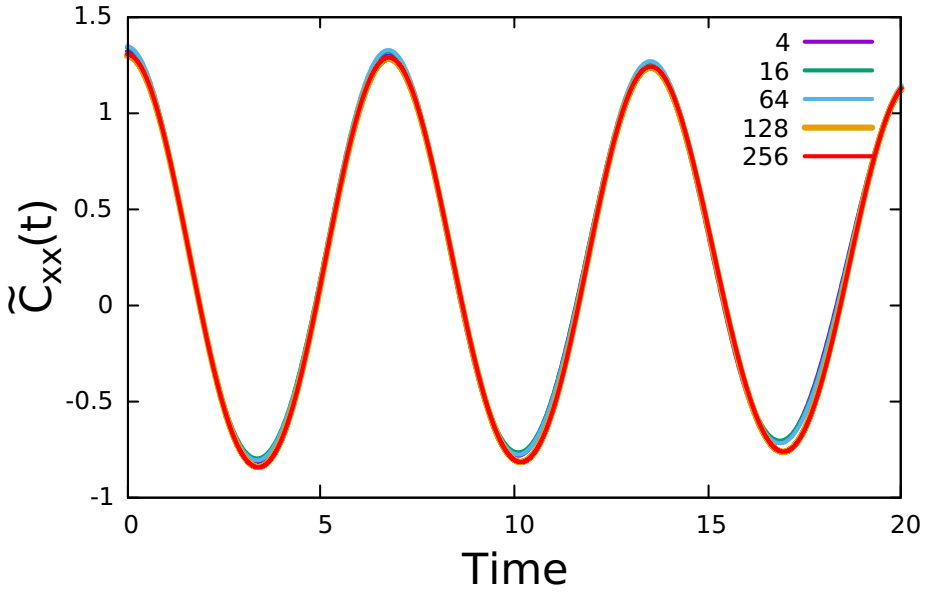

Figure 2.15: Convergence with respect to the number of replicas N of the computed TCF using the NC method at $\beta = 1$ for the mildly anharmonic potential.

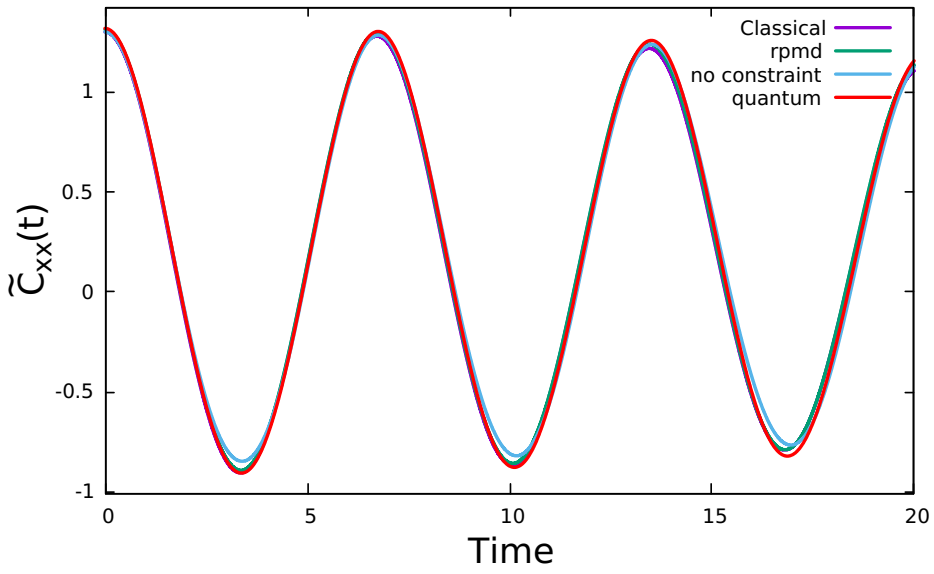

Figure 2.16: Kubo transformed position TCF for the mildly anharmonic potential at $\beta = 1$. Exact quantum (red), classical (purple), NC (blue) and RPMD (green).

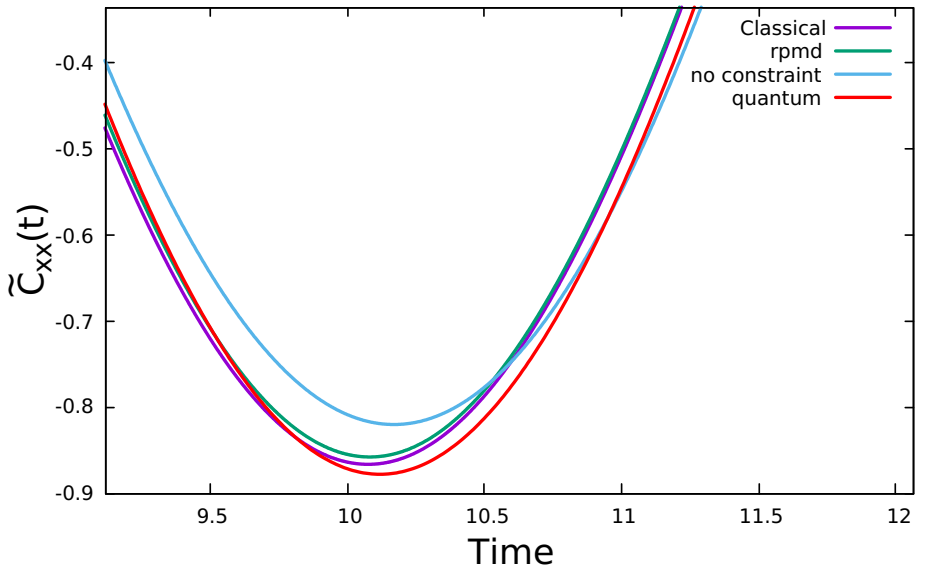

Figure 2.17: Magnified trough of Fig.(2.16) for the mildly anharmonic potential at $\beta = 1$.

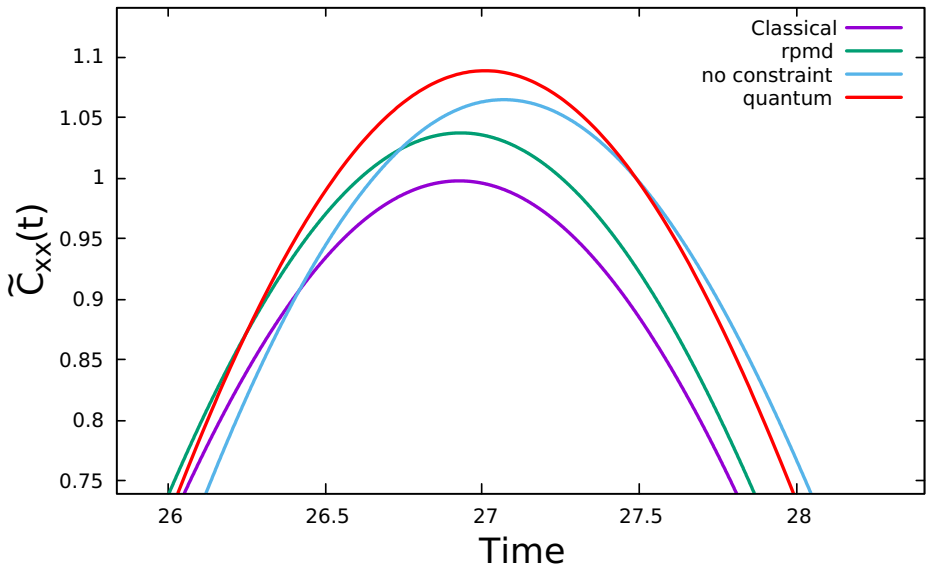

Figure 2.18: Magnified peak of Fig.(2.16) for the mildly anharmonic potential at $\beta = 1$.

For the low temperature case (Fig.(2.19)) the NC result does better than classical dynamics which fails to get the correct $t \to 0$ result. The method is able to get the peak positions better than RPMD (Fig.(2.20)), however, the problem of the method underpredicting the amplitudes of the troughs seen at high T becomes much more noticeable for the low T case as seen in Fig.(2.21).

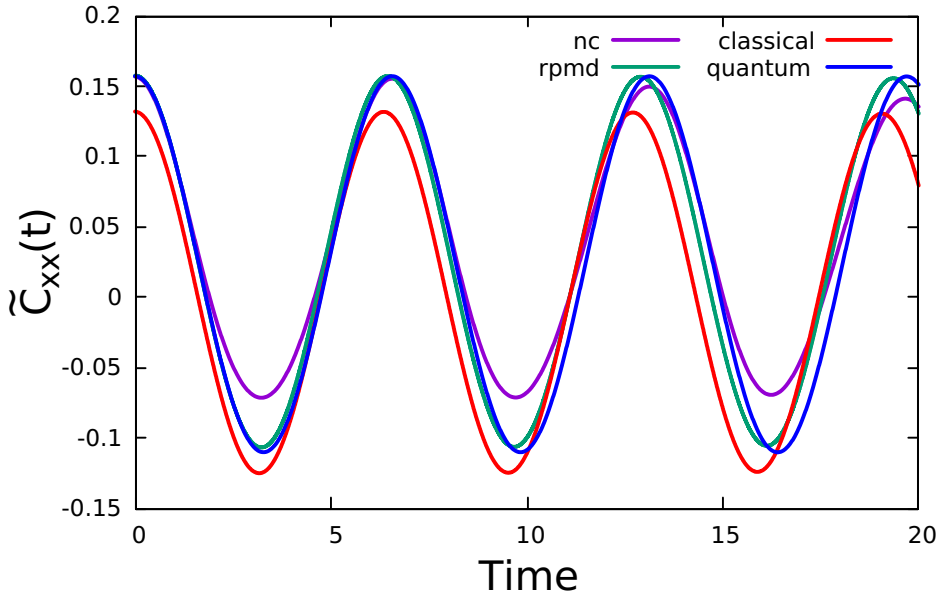

Figure 2.19: Kubo-transformed position TCF at $\beta = 8$ for the mildly anharmonic potential. Exact quantum (blue), NC (purple), classical (red) and RPMD (green).

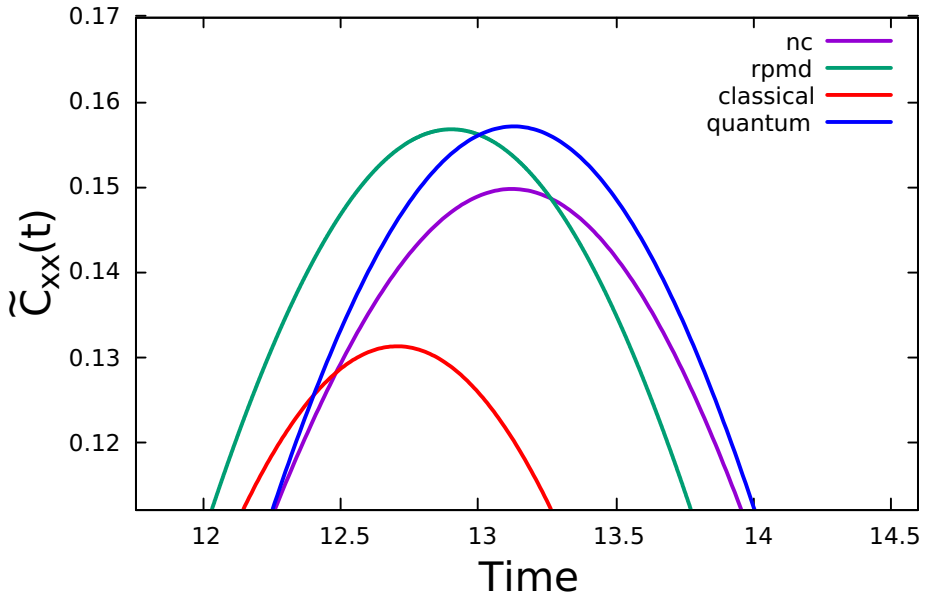

Figure 2.20: As with Fig.(2.20) but magnified at a peak. Exact quantum (blue), NC (purple), classical (red) and RPMD (green).

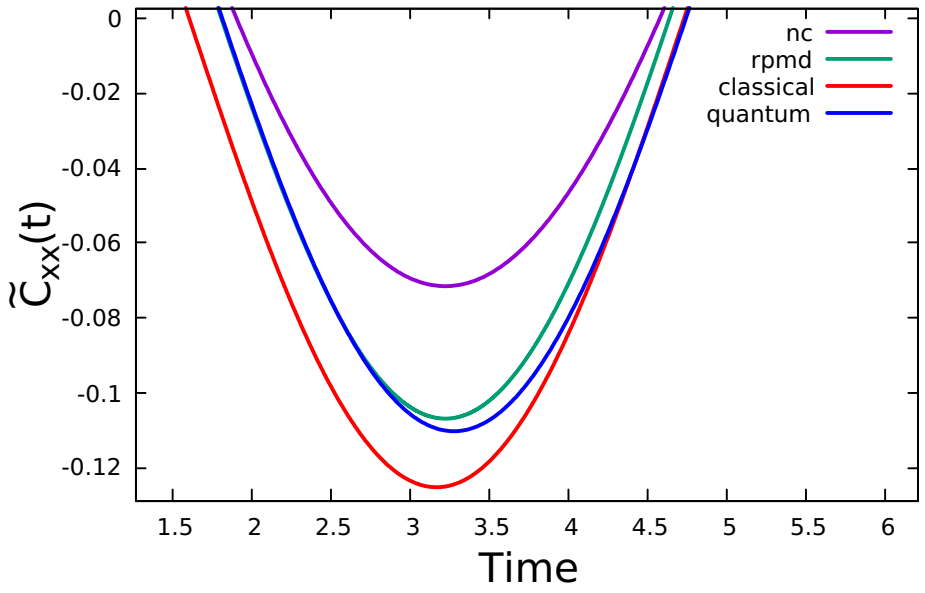

Figure 2.21: As with Fig.(2.20) but magnified at a trough. Exact quantum (blue), NC (purple), classical (red) and RPMD (green).

To further test if the NC method is simply rescaling the RPMD momenta distribution, we considered the mildly anharmonic potential at $\beta = 1$ with $N = 128$ for the free beads method described in Sec. (2.2.1). We rescale the momenta of all beads in a free beads calculation by a constant, α, i.e., we let $p = \alpha p$. Fig.(2.22)

shows this for different values of α, it can be seen that there is an optimal value of α for which the TCF gives the best agreement with the RPMD result.

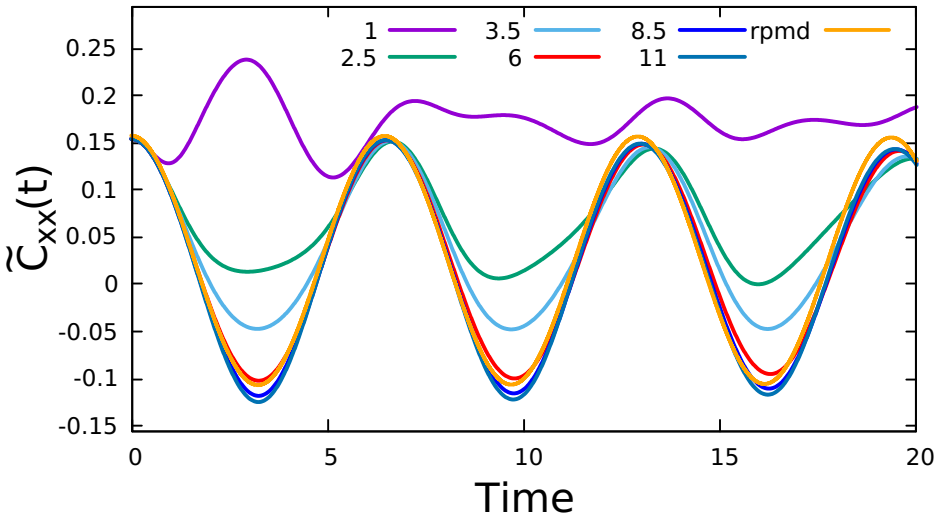

Figure 2.22: Rescaling momenta of free beads at $\beta = 1$ by a factor of α for the mildly anharmonic potential. The numbers in the key are $1/\alpha$.

Individual Trajectories

By investigating individual trajectories we can better understand the motion of the centroid of the system and understand how the components of energy vary along a trajectory. An example trajectory (Fig.(2.23)) shows both the position and momenta of the centroid for the strongly anharmonic potential at $\beta = 8$. Large oscillations in the position/momenta are seen initially, but the amplitudes of these oscillations fade away relatively quickly; this can be visualised as a phase space plot Fig.(2.24). The centroid begins at the point marked with the green triangle. As the oscillations of momenta and position decrease in amplitude we see that the particle accesses a smaller region of phase space. This trajectory is plotted for an extended time period (Fig.(2.25)); after a short period of time the centroid essentially only samples this smaller region of phase space. Initially, the beads have been set up using an RPMD simulation, however after the springs have been removed and the momenta recalculated, the system has been disrupted (i.e. it is no longer equilibrated) and so a short period of time is taken for the system to re-equilibrate, this process presents itself as the large amplitude oscillations in the centroid momenta/position or the spirals in the phase space plot.

Returning to our previous analogy of the ensemble of particles forming a 'blob' which satisfies the uncertainty principle; evolving this 'blob' of particles using purely classical dynamics results in the spread of this 'blob' decreasing. At $t = 0$, there

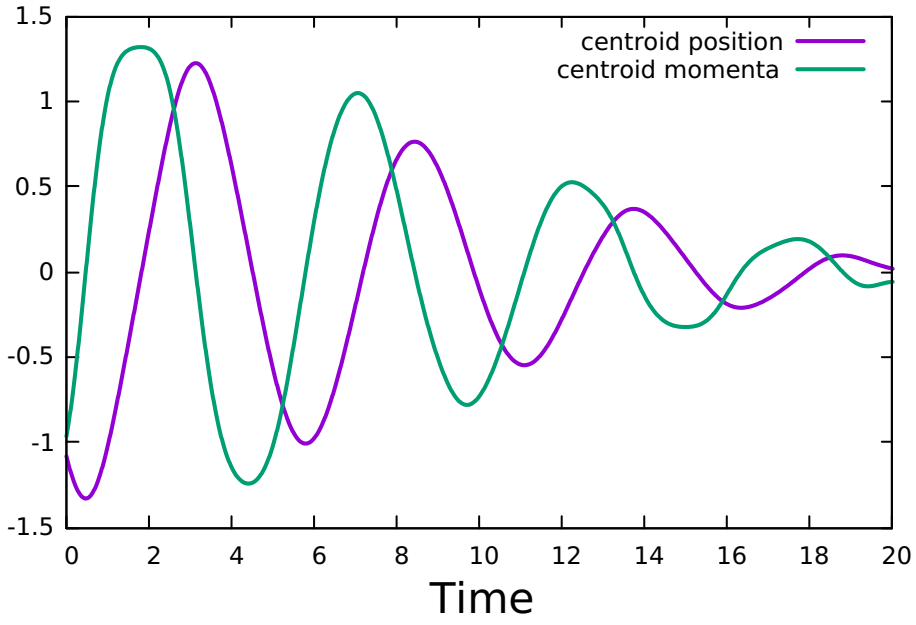

Figure 2.23: Individual trajectory for the strongly anharmonic potential at $\beta = 8$. Centroid position (purple) and centroid momenta (green).

is a distribution of x and p in the 'blob' which represents a quantum particle but at $t > 0$ this becomes classical in nature. A plot of the kinetic, potential and total energy Fig(2.26) shows large fluctuations between the total kinetic energy and total potential energy at short time. It can be noted, however, that the total energy is conserved throughout the simulation. Investigating a trajectory for an increased period of time, t (Fig.(2.27)) shows that the initial fluctuations between kinetic and potential energy appear as large spikes, at longer t the fluctuations between kinetic and potential persist, albeit at smaller amplitudes.

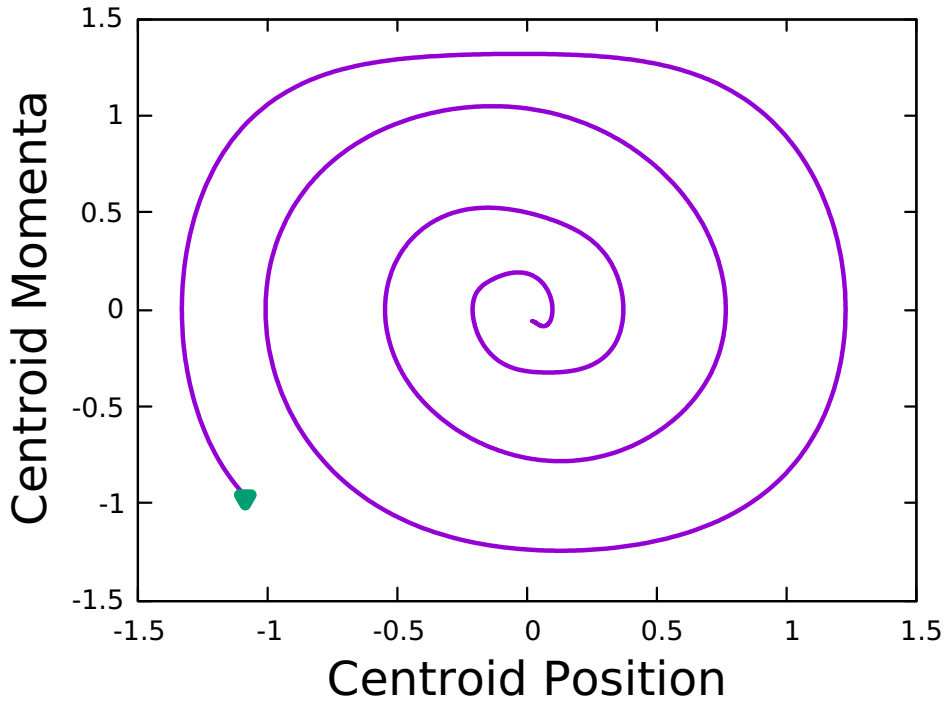

Figure 2.24: Centroid phase space plot corresponding to trajectory in Fig.(2.23).

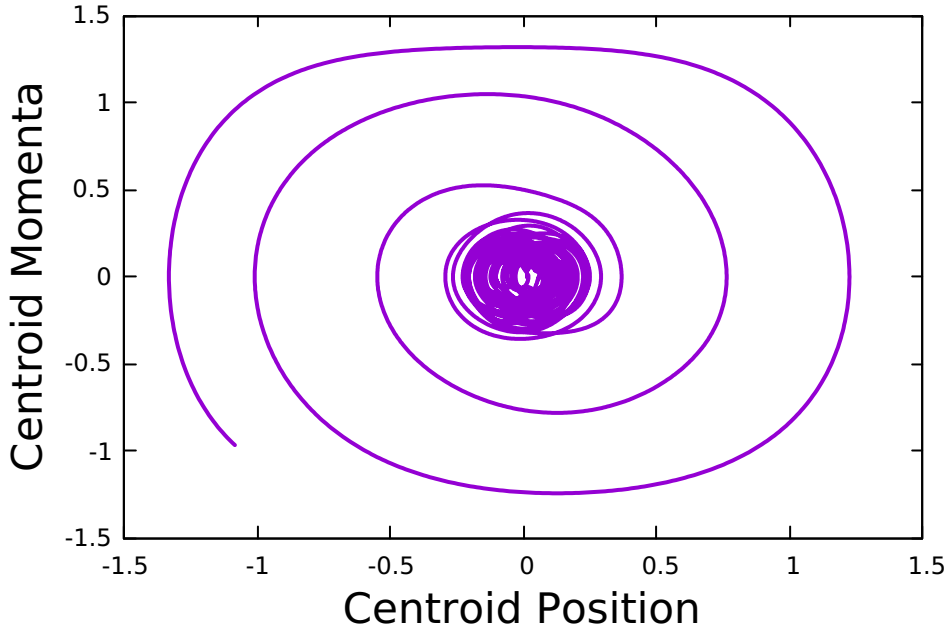

Figure 2.25: As with Fig.(2.24) but for an increased time. Once the system has re-equilibrated, the system samples a smaller region of phase space when compared with short times.

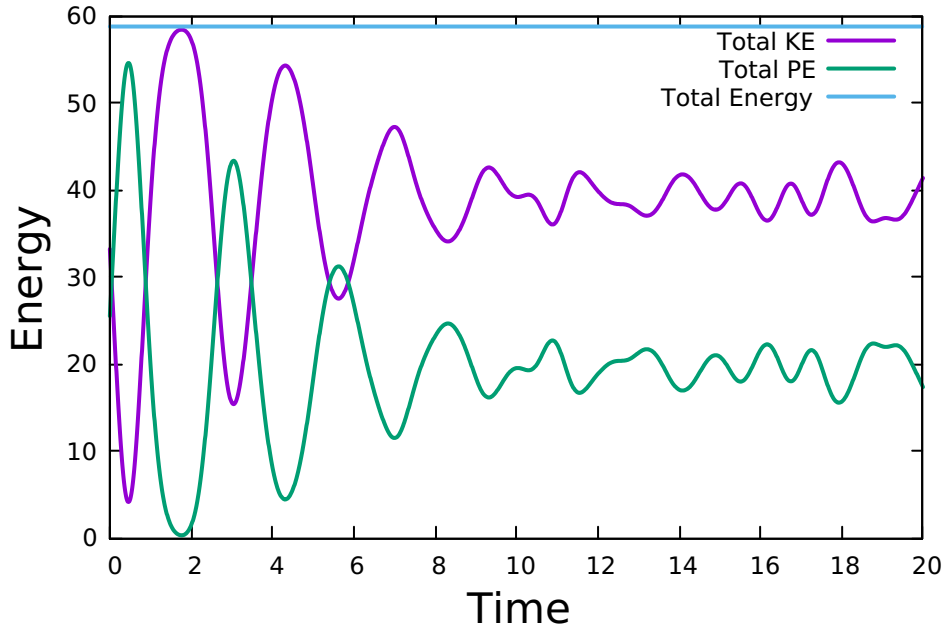

Figure 2.26: Plot of kinetic (purple), potential (green) and total (blue) energy along a trajectory for the strongly anharmonic potential at $\beta = 8$ for the NC method. Initial fluctuations in kinetic and potential energy are large but total energy is conserved.

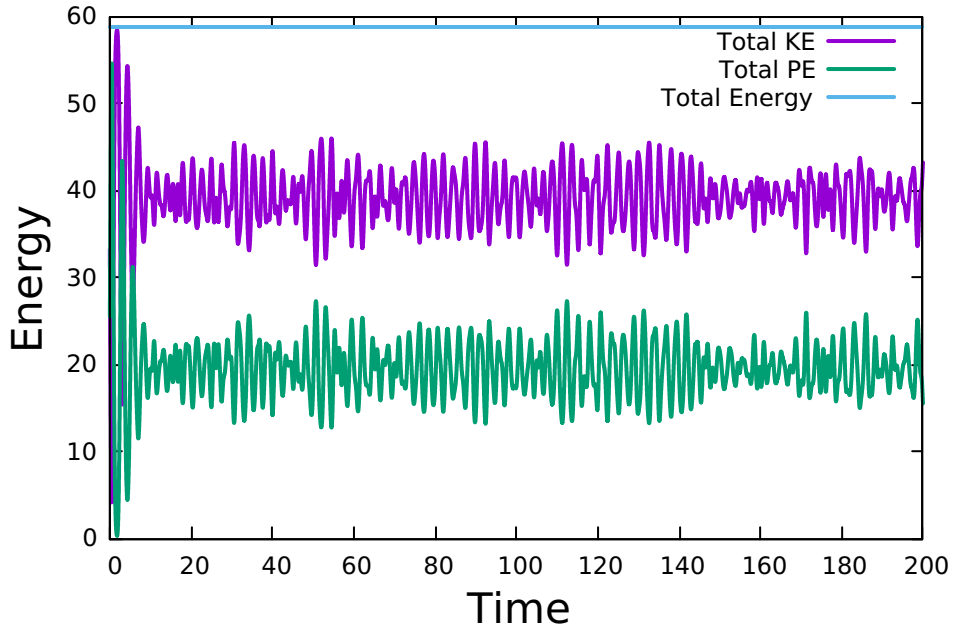

Figure 2.27: As with Fig.(2.26) but for a longer period of time. The fluctuations in energy persist although the amplitude is less than the short time spikes.

Uncertainty at $t = 0$

The choice of using a ring polymer to initialise the bead positions and momenta is made because it gives a phase space distribution which is consistent with the initial condition $\langle g(0) \rangle = \hbar^2/4$. For the strongly anharmonic potential we show that the initial positions and momenta of the system replicas in CUMD do not give exactly this minimum uncertainty, but is quite close (Fig.(2.28)). A similar pattern is also observed for the mildly anharmonic test system.

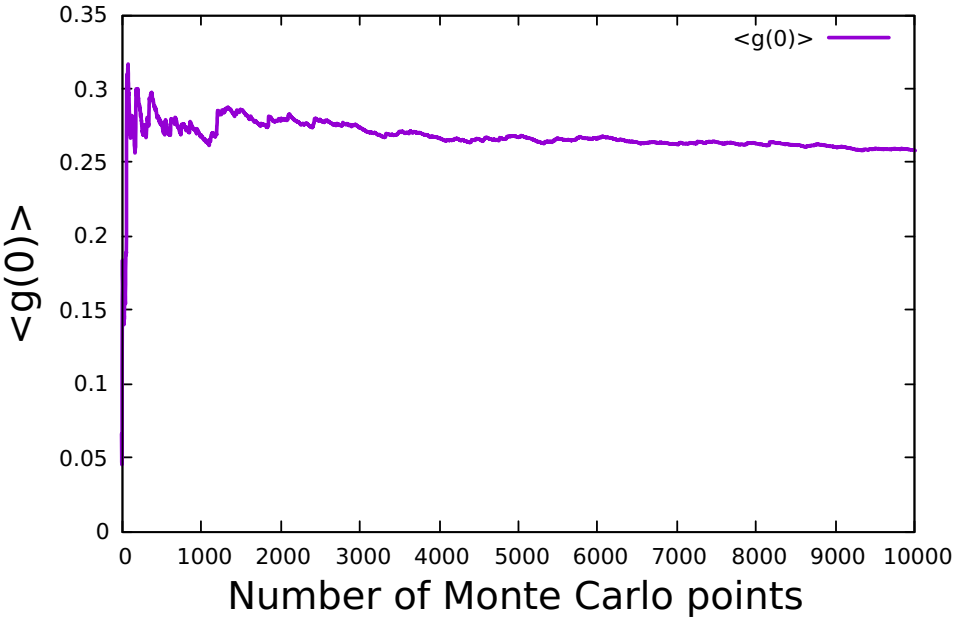

Figure 2.28: Value of the uncertainty at $t = 0$ ($g(0)$), averaged over the number of Monte Carlo sampling points for the strongly anharmonic potential at $\beta = 1$. It can be seen that the equilibrated value lies slightly above the minimum uncertainty of 0.25.

2.3.3 The Constraint

The Harmonic Limit

The equations of motion for the system replicas in a CUMD simulation are given by Eq. (2.30a) which, for the case of a harmonic potential ($V(q) = \frac{1}{2}q^2$) becomes

$$\begin{aligned}\dot{p_i}^{\mathrm{CU}} = -q_i^{\mathrm{CU}} + \lambda \Bigg[\left(q_i^{\mathrm{CU}} - \langle q \rangle^{\mathrm{CU}} \right) \times \left(\langle q^2 \rangle^{\mathrm{CU}} - \left(\langle q \rangle^{\mathrm{CU}} \right)^2 \right) \\ - \left(\langle q^2 \rangle^{\mathrm{CU}} - \left(\langle q \rangle^{\mathrm{CU}} \right)^2 \right) \times \left(q_i^{\mathrm{CU}} - \langle q \rangle^{\mathrm{CU}} \right) \Bigg]\end{aligned} \tag{2.57}$$

which simplifies to

$$\dot{p_i}^{\mathrm{CU}} = -q_i^{\mathrm{CU}} \tag{2.58}$$

i.e. the additional terms due to the addition of the constraint vanish, and the dynamics of the beads become purely classical. CUMD is equivalent to the NC method in the specific case of a harmonic potential and the dynamics of the system replicas are purely classical.

The Algorithmic Ad Hoc Fix

Although the constant-uncertainty constraint (Eq.(2.26)) is non-linear in the momentum p, it can be shown [Appendix B] that the time derivative of the constraint (Eq. (2.29)) is linear in p and can be written in the form $\sum_i \mu(q_i)\dot{q}_i$, where

$$\begin{aligned}\mu(q_i) = \Bigg[\left(\frac{\partial V}{\partial q_i}^{CU} - \left\langle \frac{\partial V}{\partial q} \right\rangle^{CU} \right) \left(\langle q^2 \rangle^{CU} - (\langle q \rangle^{CU})^2 \right) \\ - \left(\left\langle q \frac{\partial V}{\partial q} \right\rangle^{CU} - \langle q \rangle^{CU} \left\langle \frac{\partial V}{\partial q} \right\rangle^{CU} \right) \left(q_i^{CU} - \langle q \rangle^{CU} \right) \Bigg]\end{aligned} \tag{2.59}$$

Note that the use of the Heisenberg uncertainty principle would lead to terms non-linear in p which is why the Schrödinger uncertainty principle is used in CUMD.

The implementation of CUMD proposed in ref.[85] uses Eq.(2.59) to derive the equations of motion. By design, this would lead to a constant derivative of the uncertainty constraint not a constant-uncertainty constraint. To circumvent this, the author[85] introduces an ad hoc fix to treat the constraint by replacing Eq.(2.45c) and Eq.(2.45e) with the constraint which we want to satisfy ($g(t) - g(0) = 0$).

The modification to the non-holonomic integrator to treat this constraint causes several problems. An extremely short time step needs to be used (0.0025a.u in the 1-D simulations) to prevent the algorithm from becoming unstable. In the

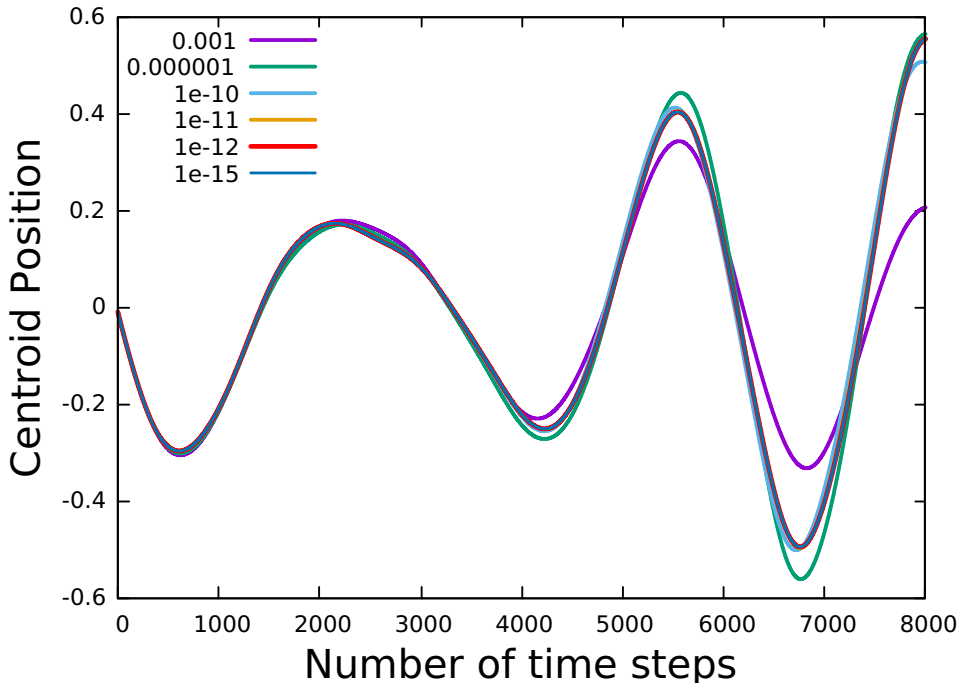

Figure 2.29: Convergence of the centroid position over a trajectory with respect to the Lagrange multiplier tolerance χ.

implementation of the constraint, a tolerance χ needs to be set. χ is selected such that the properties of interest are converged with respect to the selected value. Initially, we decided that the position of the centroid should be converged with respect to the value of the tolerance. This is shown in Fig.(2.29), it can be seen that graphical convergence of the centroid trajectory is achieved at $\chi = 1.0 \times 10^{-10}$. The convergence of the centroid momenta with respect to χ over a trajectory is also considered (Fig.(2.30)), this displays similar behaviour to the convergence of the position (graphical convergence at $\chi = 1.0 \times 10^{-11}$). The total energy of the system is considered along an individual trajectory (Fig.(2.31)), converging the total energy with respect χ requires a tighter tolerance than converging the centroid position/momenta (between $\chi = 1.0 \times 10^{-12}$ and 1.0×10^{-14} depending on the trajectory), this leads to an increase in the number of potential evaluations per time step but also causes problems due to the update formula for the Lagrange multiplier not being able to find a solution within the specified tolerance. [update formula given in Appendix A.2]. The main issue arising from the ad hoc fix in this integrator is the failure to conserve total energy along individual trajectories. The total energy of the system fluctuates a large amount in some cases as seen in Fig.(2.32). As such, we find that CUMD does not conserve energy and thus does not satisfy detailed balance.

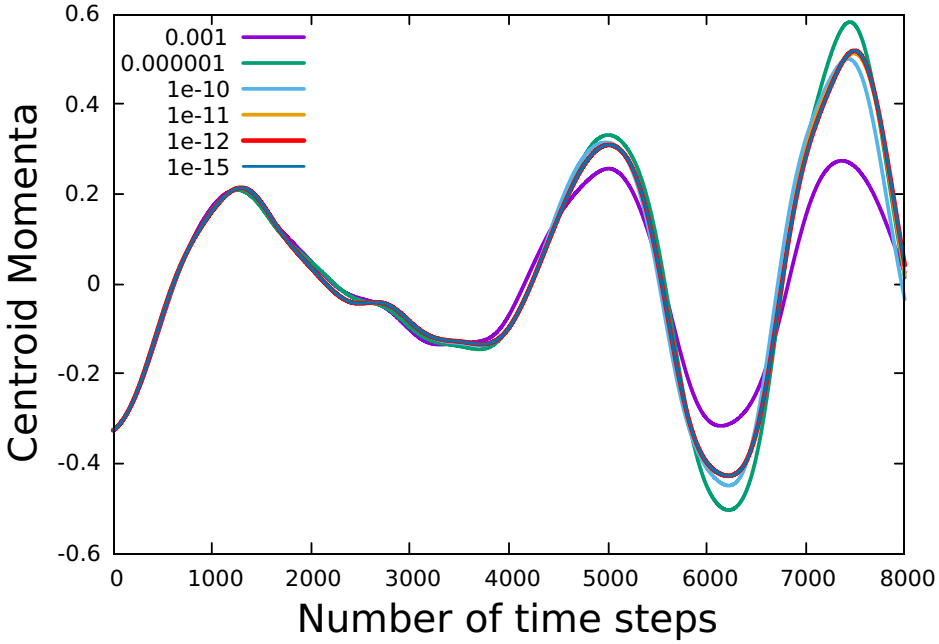

Figure 2.30: Convergence of the centroid momenta over a trajectory with respect to the Lagrange multiplier tolerance χ.

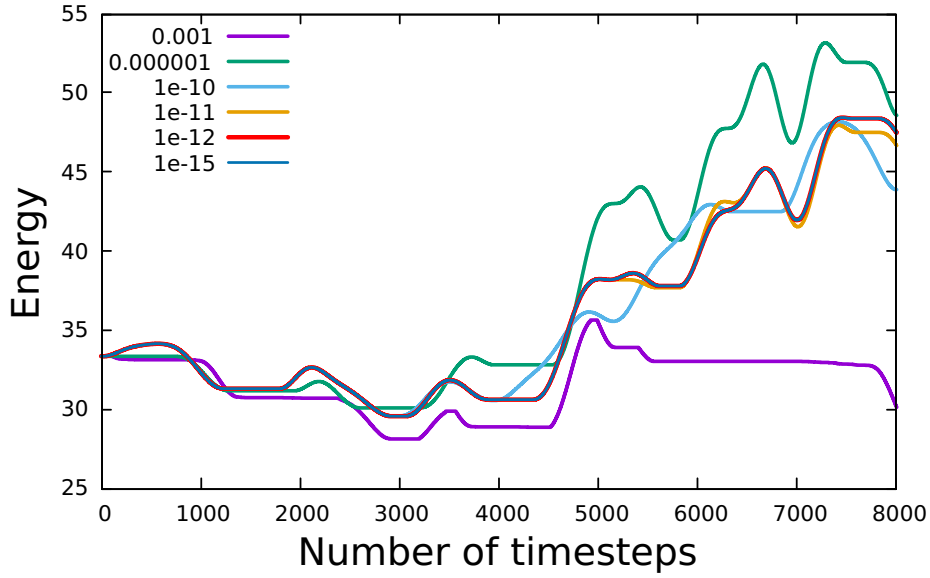

Figure 2.31: Convergence of the total energy over a trajectory with respect to the Lagrange multiplier tolerance χ.

Constrained Results

The CUMD results for the strongly anharmonic oscillator at $\beta = 1$ are shown in Fig.(2.32); implementation of the constraint has led to difficulties in sampling due to the update formula used sometimes failing to find a solution to the Lagrange multiplier within the specified tolerance. However, even with limited sampling (3500 Monte Carlo points), we have been able to reproduce the CUMD results for the strongly anharmonic potential in the high temperature case to quite good agreement (Fig.(2.33)). Comparing the CUMD TCF (Fig.(2.33)) with RPMD, classical and exact quantum data, we can see that whereas both the classical result and RPMD result fail to maintain any oscillation in the result after $t = 7$, the CUMD result does better and continues to maintain oscillations for a longer time, although the amplitude still decays. As a result, it is interesting to see that despite the problems in the method, it still gives promising results for the strongly anharmonic test system.

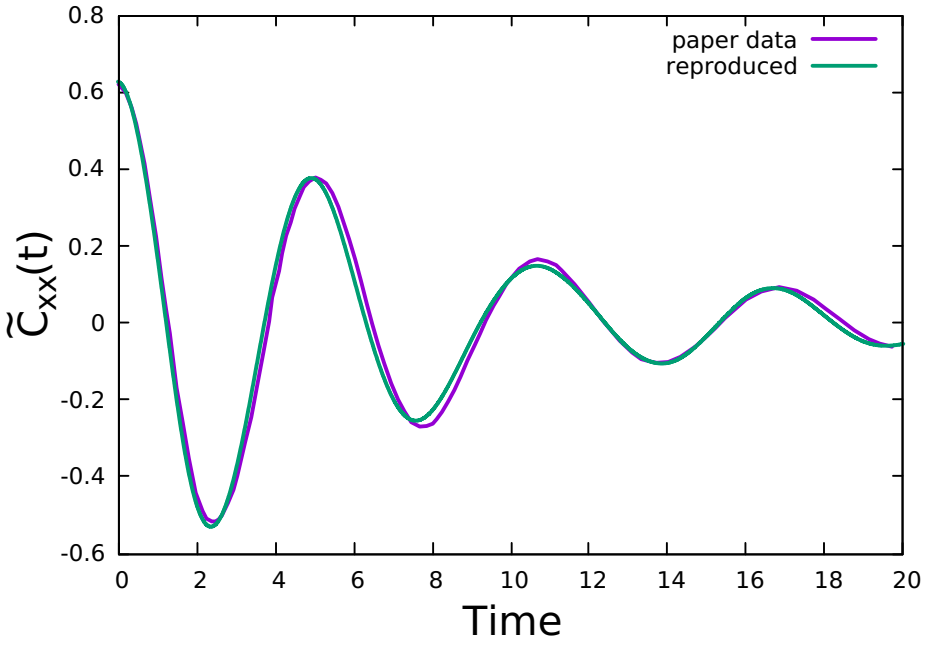

Figure 2.32: Position TCF for the strongly anharmonic potential at $\beta = 1$ comparing the CUMD results in this work with those taken from ref.[85].

For the low temperature case (Fig.(2.34)) we have been unable to successfully replicate the data given in the paper. Both the published data and our data agree at short times (up to $t = 6$), however, at later times the amplitudes of our peaks decay much more quickly than those given by Hasegawa although they occur at approximately the same t values. We were only able to sample 50,000 Monte Carlo points in the calculation of this TCF, before the instabilities in the algorithm men-

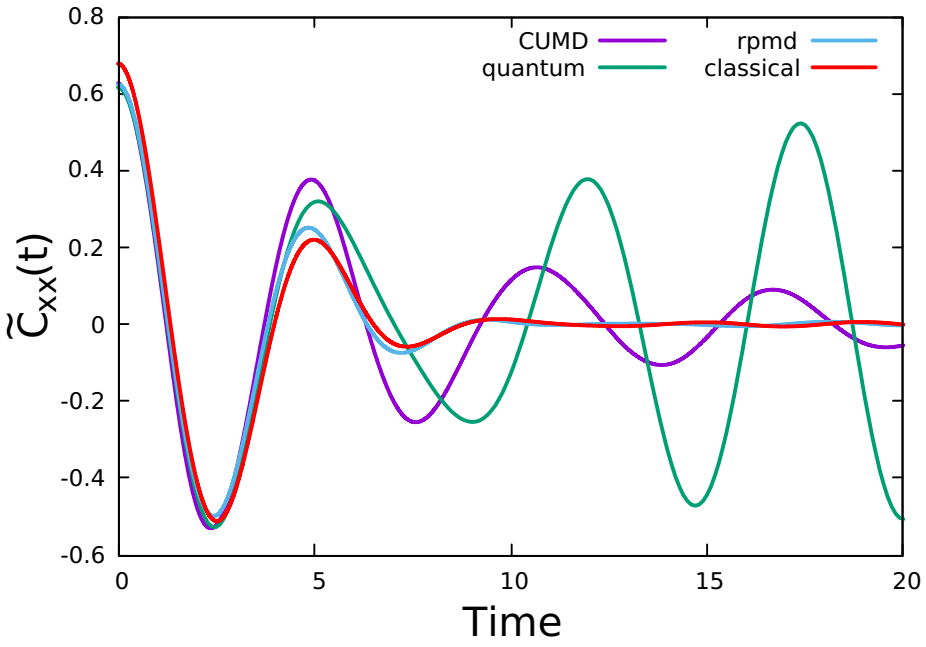

Figure 2.33: The CUMD (purple) position TCF for the strongly anharmonic potential at $\beta = 1$ compared with RPMD (blue), quantum (green) and classical (red) calculations.

tioned above became problematic. Nevertheless, the result appears to have been converged by this point and so it is unclear why this discrepancy between the two sets of CUMD results remains.

CUMD Trajectories

The uncertainty along a single trajectory for the strongly anharmonic potential was constrained to within $\chi = 1.0 \times 10^{-14}$ and the total energy investigated Fig.(2.35). For this trajectory, the large oscillations in the kinetic and potential energies continue in the entire trajectory, whereas in NC we saw that these decrease in amplitude. We also see that the total energy fluctuates (i.e. energy is not conserved along trajectories.). At $t > 12$ the total energy increases significantly, with the final energy at $t = 20$ approximately 1.5 times the initial energy. Considering the phase space plot for this trajectory (Fig.(2.36)), we see that the the addition of the constraint allows the centroid to continue to sample a larger phase space when compared to the NC case (Fig.(2.25)). Returning to our analogy of the ensemble of particles forming a quantum 'blob', we see that the addition of the constraint causes the spread in this 'blob' to remain and so the quantum nature of this ensemble is retained for $t > 0$. Considering a CUMD trajectory over a longer period of time Fig.(2.37), it can be seen that the total energy continually increases, with the energy at $t = 200$ approximately 2.5 times the energy at $t = 0$.

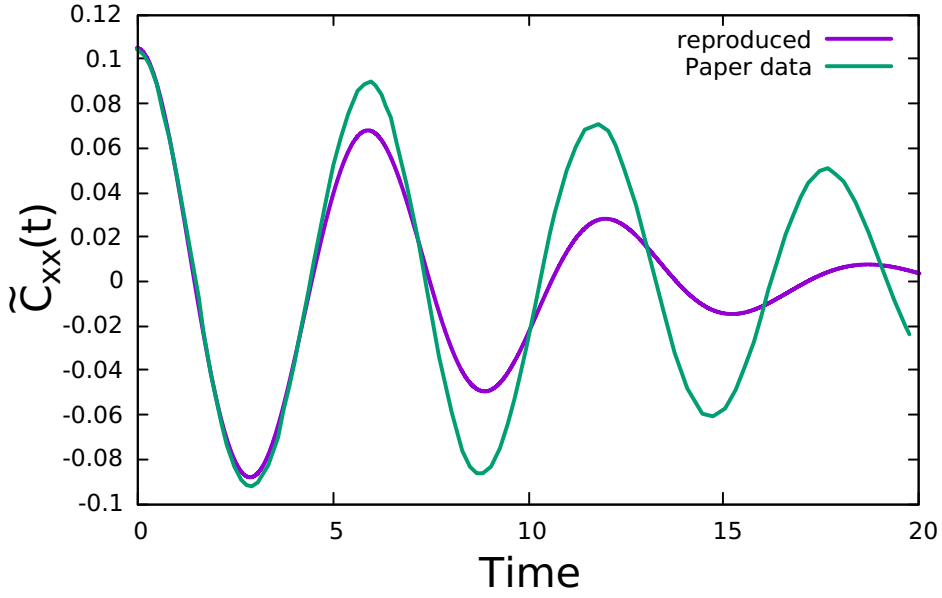

Figure 2.34: Position TCF for the strongly anharmonic potential at $\beta = 8$. Disagreement is shown between the published data (purple) and the reproduced data (green).

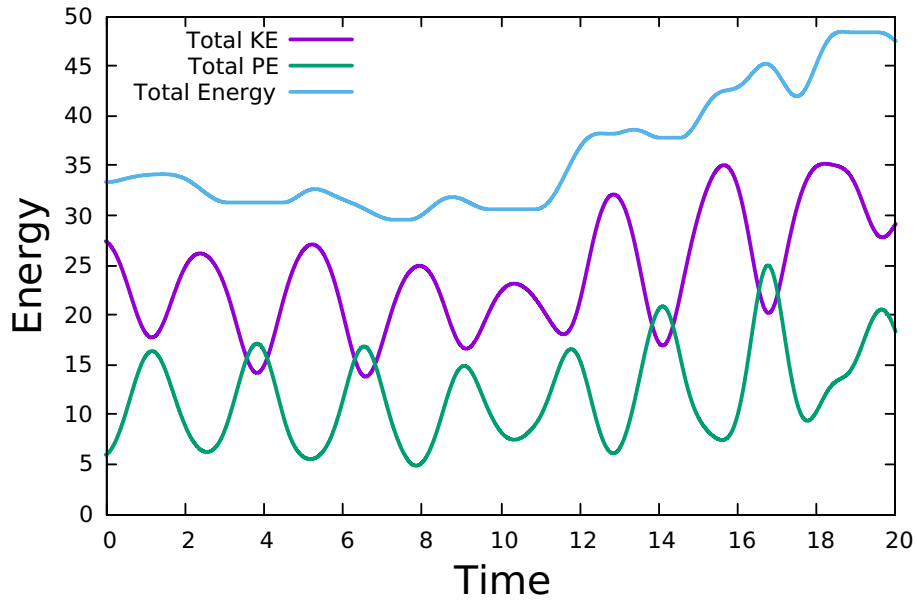

Figure 2.35: Plot of the kinetic, potential and total energy along a trajectory for CUMD for the strongly anharmonic potential at $\beta = 8$.

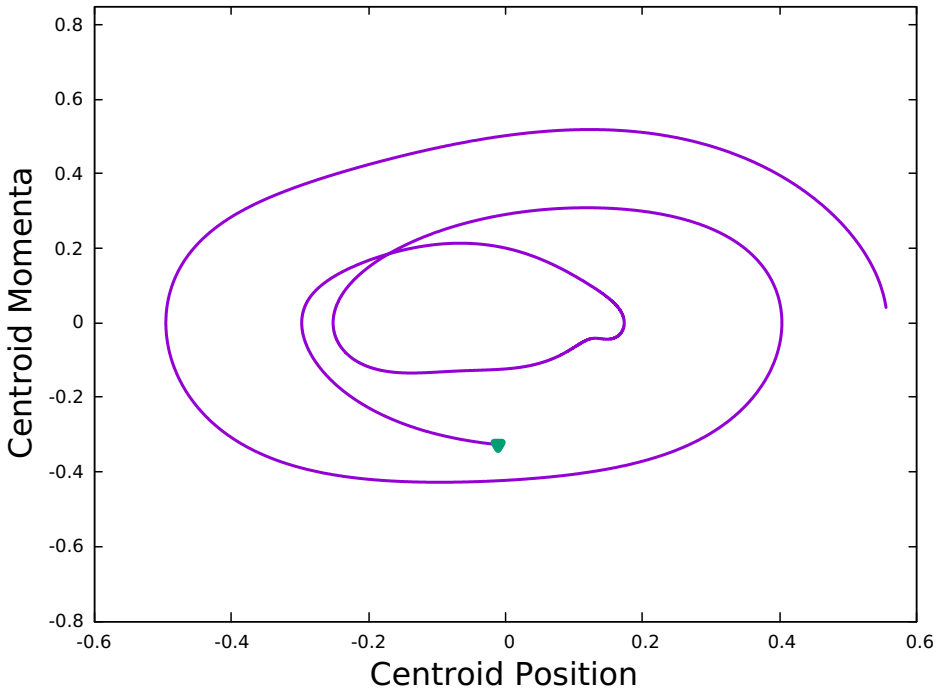

Figure 2.36: Phase space plot of the centroid for a CUMD trajectory for the strongly anharmonic potential at $\beta = 8$. The centroid starts at the point labelled by the green triangle.

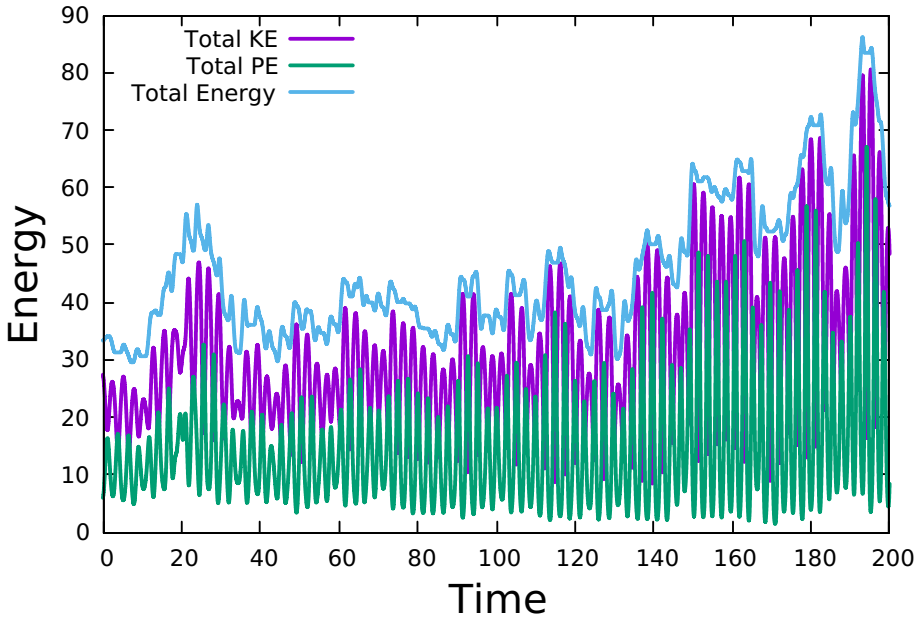

Figure 2.37: As with Fig.(2.35) but for longer periods of time. Fluctuations between kinetic and potential energy increase with time. The total energy grows with time.

We attempted to calculate TCFs for the mildly anharmonic potential, however the instability of the constraint algorithm became more problematic for this potential and so we were not able to sample enough to converge the TCF. Fig.(2.38) shows an individual trajectory for this potential at $\beta = 8$. As it can be seen in Fig(2.39), the total energy along a trajectory does not fluctuate as much for this potential when compared to the strongly anharmonic potential for short times, $t < 20$. Despite this, allowing the trajectory to evolve for a longer period of time (Fig.(2.40)), we see that the total energy grows and shows some oscillations after approximately 25,000 time steps.

After investigating individual trajectories for the CUMD method, the failure of the method to conserve energy is of concern; therefore, it is unlikely that CUMD would be a suitable method for larger systems.

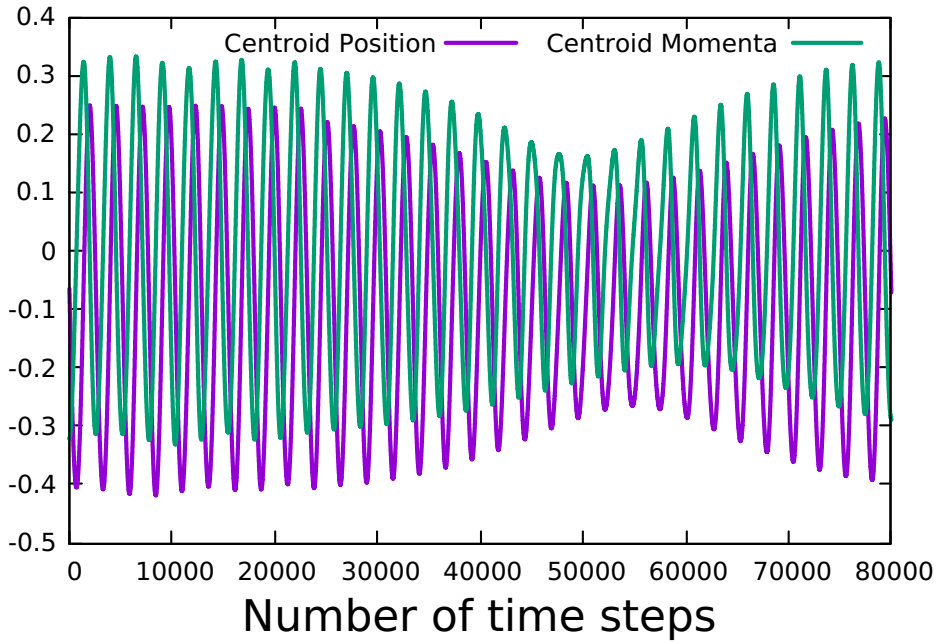

Figure 2.38: Position and momenta of the centroid during a single CUMD trajectory for the mildly anharmonic potential at $\beta = 8$. (time step = 0.0025a.u.)

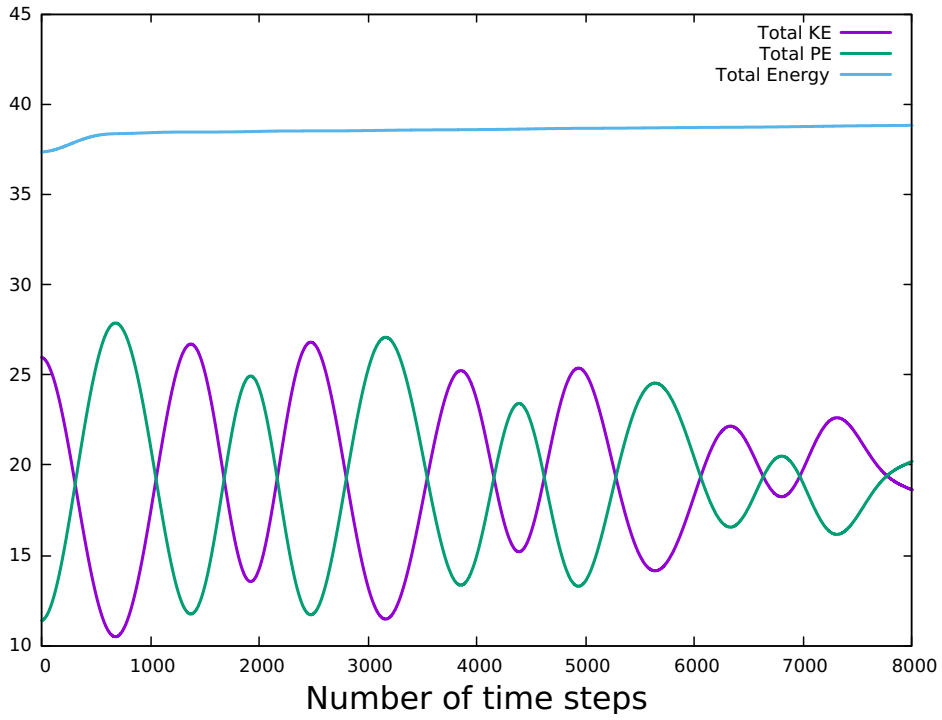

Figure 2.39: Plot of kinetic, potential and total energy during a single CUMD trajectory for the mildly anharmonic potential at $\beta = 8$. The total varies slowly over short times. (time step = 0.0025a.u.)

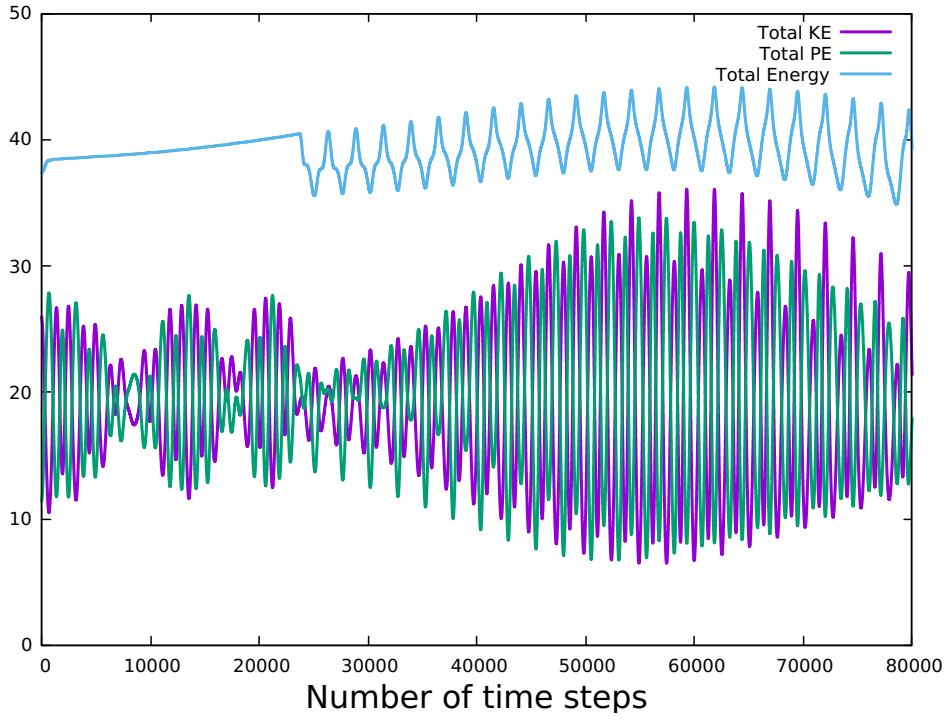

Figure 2.40: As with Fig.(2.39) but for longer times, after approximately 25,000 time steps the total energy displays oscillatory behavior. (time step = 0.0025a.u.)

2.4 Tests on Two-Dimensional Models

Given that the CUMD method does not conserve energy and is numerically unstable, it is unlikely that it can be extended to treat larger, more realistic systems. Here, we examine whether the NC method (in which the constraint is applied only at $t = 0$) can be used as a stand alone method by testing it on the two-dimensional (2D) champagne-bottle Morse potential.

It is straightforward to extend the NC method to 2D. In 1D, the bead momenta are rescaled according to Eq.(2.35). Extending this to two dimensions, we take the approach of rescaling the x and y components of the momenta separately so that

$$p^0_{D_i} = \sqrt{\frac{2mK^{CL}_D}{N}} \frac{\langle p^{\mathrm{RPMD}}_D \rangle}{|\langle p^{\mathrm{RPMD}}_D \rangle|} + \alpha_D s_{D_i}, \qquad D = x, y \tag{2.60}$$

Thus the rescaling procedure is the same in 2-D as in 1-D except that each quantity in Eq.(2.60) is calculated in the x and y dimensions.

The champagne-bottle Morse potential is of the form

$$V(r) = D_e(1 - e^{-\alpha(r-r_{eq})})^2 \tag{2.61}$$

where the parameters are chosen to model a rotating OH bond. The reduced mass of the OH unit is $\mu = 1741.0598$, $\alpha = 1.1605$, $r_{eq} = 1.8324$ and $D_e = 0.18748$ in atomic units.

The position autocorrelation functions are calculated for this potential for different N at a temperature of 109.2K (Fig.(2.41)), we see that the TCF converges with respect to N but in this 2D test system we see some 'zigzagging' at shorter times, which is an artificial magnification in the vibrational component of the TCF and is seen for all N and at higher temperatures.

The convergence of the KQMV is much slower in 2D than in 1D. Fig.(2.42) shows that the KQMV for both x and y fail to converge quickly. In this instance, we can see that this quantity does not converge until approximately 1.5 million time steps. As a result, it is not possible to allow these quantities to converge before the TCF is calculated as this would increase the computational cost of the calculation by several orders of magnitude.

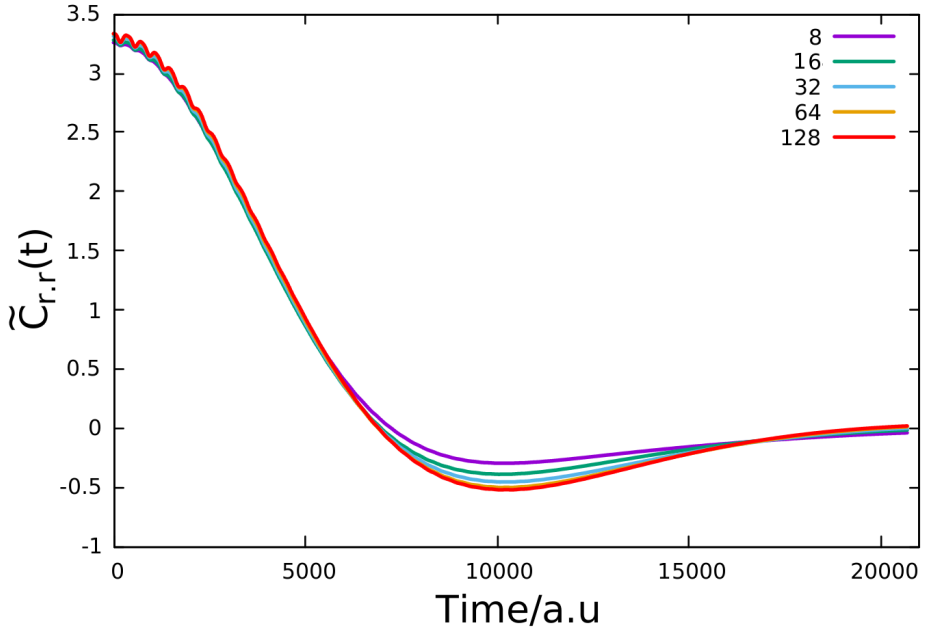

Figure 2.41: Position TCF for the champagne-bottle Morse potential at 109.2K using the NC method with various number of beads. The TCF is converged at $N = 64$.

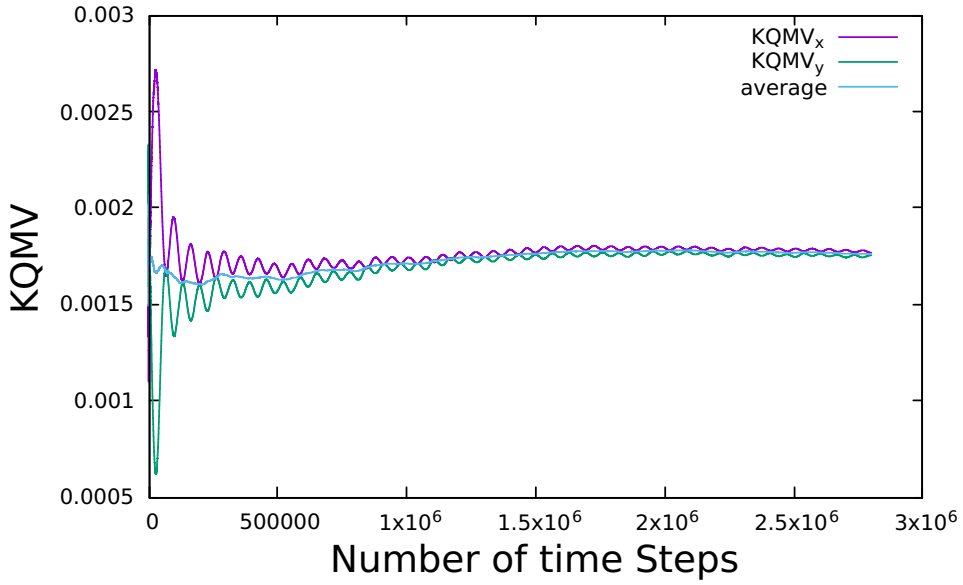

Figure 2.42: Convergence of KQMV for both the x (purple) component and y component (green) and the averaged value (blue).

Rovibrational Spectra

Absorption spectra can be derived from Fermi's golden rule using the following expression

$$n(\omega)\alpha(\omega) = \frac{2\pi\beta\omega^2}{3Vc}\int_{-\infty}^{\infty} e^{-i\omega t}\tilde{C}_{\mu.\mu}(t)dt \tag{2.62}$$

where α is the absorption coefficient, V is the volume of the sample, c is the speed of light in a vacuum, n is the refraction coefficient and μ is the dipole moment. In our work we ignore the constants in Eq.(2.62) as the units of intensity in our study have arbitrary units. As a result, the following expression can be used to calculate the IR spectra (where FT indicates the Fourier transform).

$$n(\omega)\alpha(\omega) = \omega^2 \mathrm{FT}[\tilde{C}_{r.r}](\omega) \tag{2.63}$$

Before Fourier transforming the TCF, we apply a damping function to ensure that the TCF goes to zero smoothly at the end point, t_{max} but does not alter the TCF elsewhere; the form of the damping function is:

$$f(t) = \begin{cases} \frac{1}{2}\left(\cos\left(\frac{\pi t}{\Delta t}\right)+1\right), & t \leq \Delta t \\ 0, & \text{elsewhere} \end{cases} \tag{2.64}$$

where Δt is set as $t_{max} = 500$ fs.

We first plot the spectrum at 109.2K for the O-H bond (Fig.(2.43)) for two different values of N to show how the spectrum converges with respect to the number of beads: as N increases from 32 to 64 that there is no shift in the peak positions, only a slight change in intensity and the spectrum is converged at 64 beads. We then compare this result to classical and RPMD simulations at the same temperature (Fig.(2.44)). Comparing to RPMD, we see that the NC gets the correct positions of the peaks in the spectra, slightly overpredicts the intensity of the rotational peak at $\sim$100cm^{-1} and overestimates the intensity of the vibrational peak by two orders of magnitude. This problem with the vibrational peak can be expected due to the 'zigzagging' in the TCF mentioned earlier.

At a higher temperature of 436.5K (Fig.(2.45)) we see that the peaks occur at approximately the correct position but the intensity of the vibrational peak is again much too high. We tested the NC method at higher temperatures, but this resulted in the same problems in the TCF and spectra as we have seen at low and intermediate temperatures. Another artifact seen in both the low and high temperature spectra is the negative dip between 3000-3200cm^{-1}.

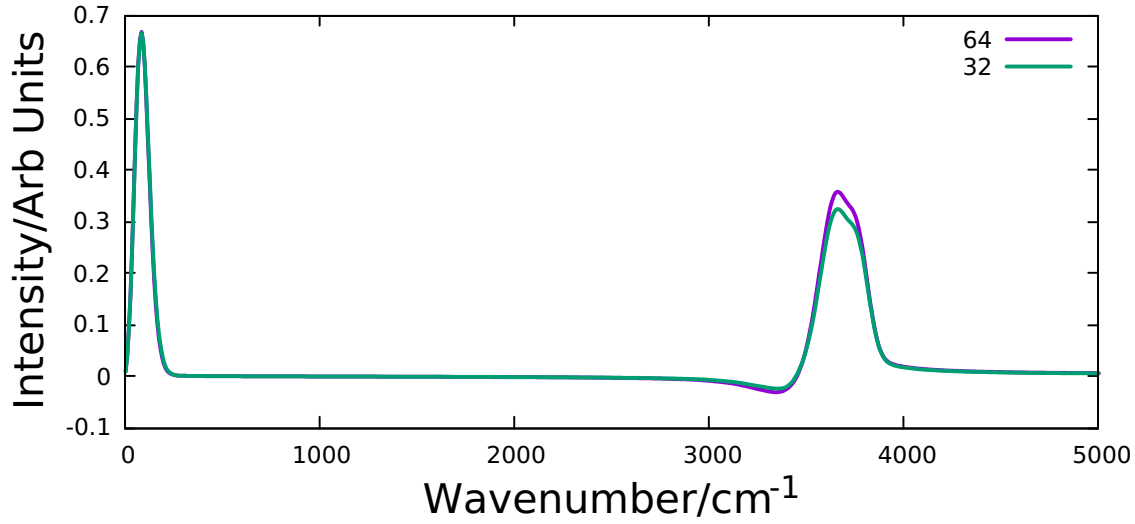

Figure 2.43: Spectra for the Morse potential at 109.2K using the NC method at 64 beads (purple) and at 32 beads (green).

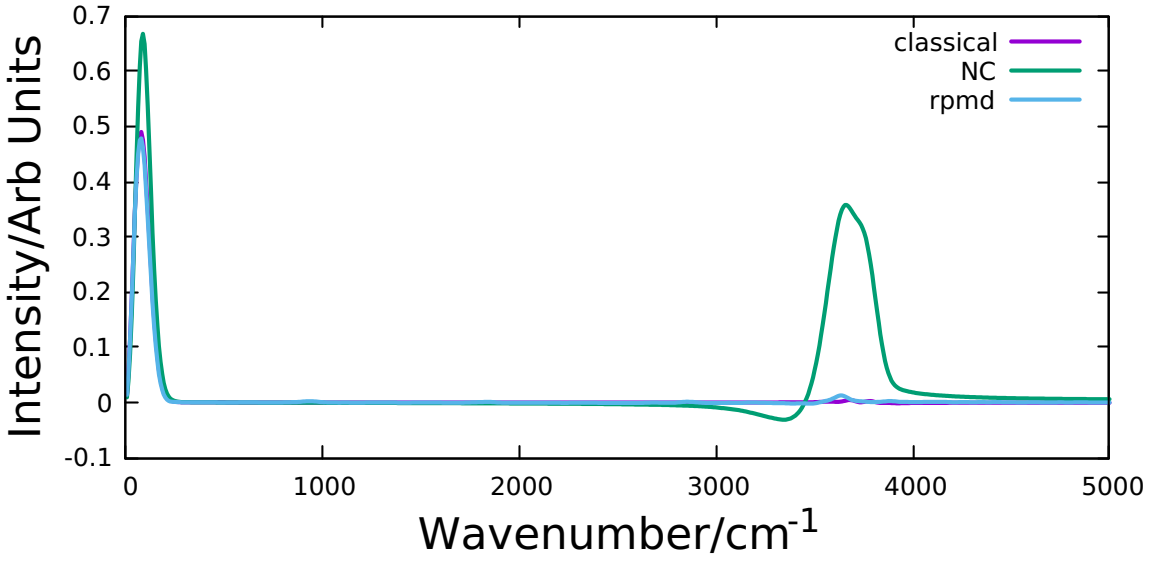

Figure 2.44: Spectra for the Morse potential at 109.2K using the NC method (green), classical dynamics (purple) and rpmd (blue).

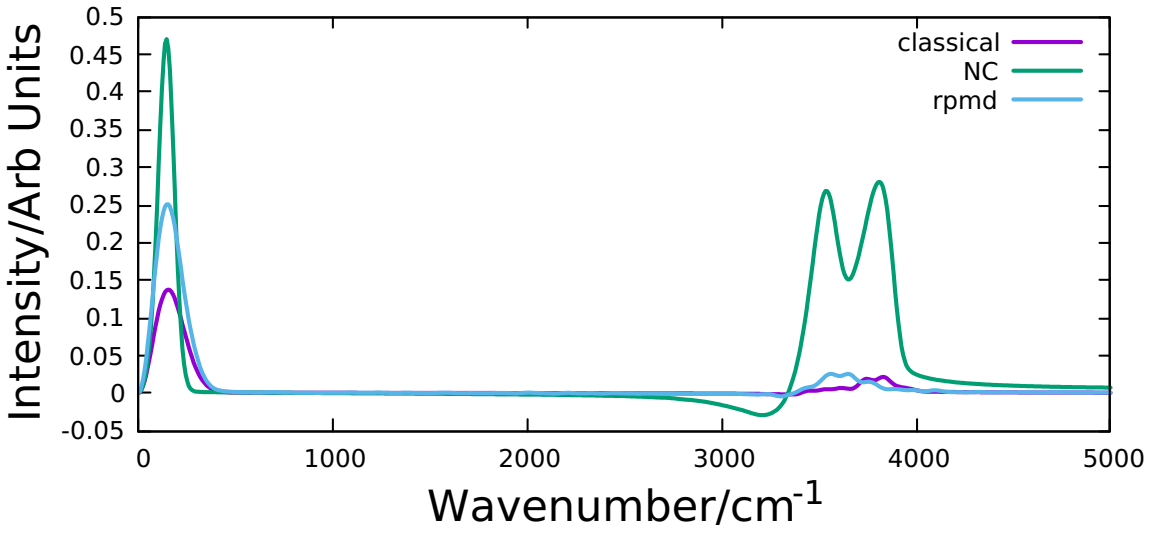

Figure 2.45: Spectra for the Morse potential at 436.5K using the NC method at 64 beads (purple) and at 128 beads (green).

2.5 Conclusions

We show that the application of the constraint in constant-uncertainty molecular dynamics (CUMD) uses an ad hoc fix in the algorithm which results in the method failing to conserve energy and becoming numerically unstable. Furthermore, we use the initial momenta rescaling step of the method, then allow the distribution to evolve classically which we test on toy one and two dimensional systems. We find that for the champagne-bottle Morse potential that the method is able to correctly predict the peak positions in the vibrational spectrum but overestimates the intensities by two orders of magnitude. We conclude that CUMD, both the original and modified version are impractical and unlikely to be able to approximate quantum dynamics for larger more realistic test systems.

Chapter 3

The Fitted Harmonic Approximation

3.1 Background Theory

3.1.1 The Wigner-Space Representation

We restrict the following treatment to the 1D case with $\hat{H} = \hat{p}^2/2m + \hat{V}(x)$ to simplify the algebra, but this readily generalises to the multi-dimensional case which we will return to when discussing numerical application in Sec.(3.1.6). Starting with the standard expression for the quantum TCF given in Eq.(2.1) and expanding in the basis of position states gives[73; 74]

$$C_{AB}(t) = \int dx \, \langle x | \, e^{-\beta \hat{H}} \hat{A} \hat{B}(t) \, | x \rangle \tag{3.1}$$

Inserting the identity operator

$$\hat{I} = \int_{-\infty}^{\infty} dy \, |y\rangle \, \langle y| \tag{3.2}$$

allows the quantum TCF for two operators $\hat{A}$ and $\hat{B}$ to be written as

$$C_{AB}(t) = \int dx \int dy \, \langle x | \, e^{-\beta \hat{H}} \hat{A} \, |y\rangle \, \langle y| \, \hat{B}(t) \, |x\rangle \tag{3.3}$$

Changing variables

$$q = (x + y)/2 \tag{3.4a}$$

$$\Delta = x - y \tag{3.4b}$$

and noting that the Jacobian is unity i.e. $dxdy = dqd\Delta$, we obtain

$$C_{AB}(t) = \int dq \int d\Delta \, \langle q + \Delta/2| \, e^{-\beta \hat{H}} \hat{A} \, |q - \Delta/2\rangle \, \langle q - \Delta/2| \, \hat{B}(t) \, |q + \Delta/2\rangle \tag{3.5}$$

Finally, inserting the identity operator for the dirac delta function

$$\begin{aligned} \hat{I} &= \int d\Delta' \, \delta(\Delta + \Delta') \\ &= \frac{1}{2\pi\hbar} \int d\Delta' \int dp \, e^{ip(\Delta+\Delta')/\hbar} \end{aligned} \tag{3.6}$$

$$C_{AB}(t) = \frac{1}{2\pi\hbar} \int dq \int dp \, \left[e^{-\beta \hat{H}} \hat{A}\right]_W (q,p) \left[\hat{B}(t)\right]_W (p,q) \tag{3.7}$$

where the Wigner transform of an operator $\hat{O}$ has been defined as

$$\left[\hat{O}\right]_W (p,q) = \int d\Delta \, \langle q + \Delta/2| \, \hat{O} \, |q - \Delta/2\rangle \, e^{ip\Delta/\hbar} \tag{3.8}$$

It is important to note that no approximation has been made in going from Eq.(3.1) to Eq.(3.7). The TCF has simply been rewritten in a form which contains classical-like phase space variables (p and q). This form of the time correlation function was first presented in the 1930s and is known as the Wigner phase space representation of the quantum TCF.[34]

3.1.2 The Moyal Series

To obtain the Liouvillian operator for the Wigner-transformed time correlation function, we begin by differentiating the TCF with respect to time[73; 74; 76]

$$\frac{d}{dt} C_{AB}(t) = \int dq \int dp \, [e^{-\beta \hat{H}} \hat{A}]_W (q,p) \left[\frac{i}{\hbar} [\hat{H}, \hat{B}(t)]\right]_W (p,q) \tag{3.9}$$

the commutator arises from the fact that

$$\frac{d}{dt} e^{+i\hat{H}t/\hbar} \hat{B} e^{-i\hat{H}t/\hbar} = \frac{i}{\hbar} [\hat{H}, e^{+i\hat{H}t/\hbar} \hat{B} e^{-i\hat{H}t/\hbar}] \tag{3.10}$$

Noting that $\hat{H} = \hat{p}^2/2m + \hat{V}$, we can write

$$\begin{aligned} \frac{d}{dt} [B(t)]_W (q,p) = &\frac{i}{\hbar} \int d\Delta \, e^{ip\Delta/\hbar} \, \langle q - \Delta/2| \left[\frac{\hat{p}^2}{2m}, \hat{B}(t)\right] |q + \Delta/2\rangle \\ &+ \frac{i}{\hbar} \int d\Delta \, e^{ip\Delta/\hbar} \, \langle q - \Delta/2| \left[\hat{V}, \hat{B}(t)\right] |q + \Delta/2\rangle \end{aligned} \tag{3.11}$$

It has been shown[74; 101] that the first term can be written as

$$\frac{i}{\hbar}\int d\Delta\, e^{ip\Delta/\hbar}\left\langle q-\Delta/2\right|\left[\frac{\hat{p}^2}{2m},\hat{B}(t)\right]\left|q+\Delta/2\right\rangle=\frac{p}{m}\frac{\partial}{\partial q}[\hat{B}(t)]_W \tag{3.12}$$

and the second term as

$$\frac{i}{\hbar}\int d\Delta\, e^{ip\Delta/\hbar}\left\langle q-\Delta/2\right|\left[\hat{V},\hat{B}(t)\right]\left|q+\Delta/2\right\rangle=-\frac{2}{\hbar}V(q)\sin\left(\frac{\hbar}{2}\frac{\overleftarrow{\partial}}{\partial q}\frac{\overrightarrow{\partial}}{\partial p}\right)[\hat{B}(t)]_W \tag{3.13}$$

where the arrows indicate the direction in which the derivative is applied. Combining Eq.(3.12) and Eq.(3.13), we can write

$$\frac{d}{dt}[\hat{B}(t)]_W=\mathcal{L}_{\mathcal{Q}}[\hat{B}(t)]_W \tag{3.14}$$

where $\mathcal{L}_{\mathcal{Q}}$ is the exact quantum Liouvillian,

$$\mathcal{L}_{\mathcal{Q}}=\frac{p}{m}\frac{d}{dq}-\frac{2}{\hbar}V(q)\sin\left(\frac{\hbar}{2}\frac{\overleftarrow{\partial}}{\partial q}\frac{\overrightarrow{\partial}}{\partial p}\right) \tag{3.15}$$

This is often referred to as the Moyal series because the sin term can be expanded as a series in powers of $\hbar^2$ to give

$$\mathcal{L}_{\mathcal{Q}}=\frac{p}{m}\frac{d}{dq}-\sum_{\lambda=1,\text{odd}}^{\infty}\frac{1}{\lambda!}\left(\frac{i\hbar}{2}\right)^{\lambda-1}\frac{\partial^\lambda V(q)}{\partial q^\lambda}\frac{\partial^\lambda}{\partial p^\lambda} \tag{3.16}$$

If all of the terms in the series are included, then the application of $\mathcal{L}_{\mathcal{Q}}$ generates exact quantum dynamics.

3.1.3 LSC-IVR

To obtain LSC-IVR, the quantum Liouvillian is written in the form[73]

$$\mathcal{L}_{\mathcal{Q}}=\mathcal{L}_{\mathcal{C}}+\mathcal{O}(\hbar^2) \tag{3.17}$$

where $\mathcal{L}_{\mathcal{C}}$ is the classical Liouvillian

$$\mathcal{L}_{\mathcal{C}}=\frac{p}{m}\frac{\partial}{\partial q}-\frac{\partial V}{\partial q}\frac{\partial}{\partial p} \tag{3.18}$$

The quantum Liouvillian $\mathcal{L}_{\mathcal{Q}}$ is then truncated at $\hbar^0$. As a result, the LSC-IVR approach replaces the exact quantum dynamics with classical dynamics such that

$C_{AB}(t)$ can be written as

$$C_{AB}(t) = \frac{1}{2\pi\hbar}\int dq \int dp \left[e^{-\beta\hat{H}}\hat{A}\right]_W (q,p) e^{\mathcal{L}_C t} \left[\hat{B}(0)\right]_W (p,q) \tag{3.19}$$

The LSC-IVR approach is known to be exact in the harmonic limit, high temperature limit (where $[e^{-\beta\hat{H}}\hat{A}]_W \to e^{-\beta H}A$) and also the $t = 0$ limit.[28; 33] Despite the successes of the LSC-IVR, the main drawback with the method is that, in general, it does not preserve the quantum Boltzmann distribution

$$\mathcal{L}_C[e^{-\beta\hat{H}}]_W \neq 0 \tag{3.20}$$

As a result

$$C^W_{AB}(t) \neq C^W_{BA}(-t) \tag{3.21}$$

i.e. it does not satisfy detailed balance. We return to this point in Sec.(3.1.5).

3.1.4 Ring-Polymer Representation of Time-Correlation Functions

It is also possible to represent the exact time-correlation functions over an extended ring-polymer phase space (Fig.(3.1)). This was done in previous work by Hele et al.[102] The ring-polymer quantum time-correlation function is defined as

$$\begin{aligned} C_{AB}^{[N]}(t) = &\int d\mathbf{q} \int d\Delta \int d\mathbf{z}\, A(\mathbf{q}) B(\mathbf{z}) \\ &\times \prod_{l=1}^{N} \langle q_{l-1} - \Delta_{l-1}/2 |\, e^{-\beta_N \hat{H}} \,| q_l + \Delta_l/2 \rangle \\ &\times \langle q_l + \Delta_l/2 |\, e^{-i\hat{H}t/\hbar} \,| z_l \rangle \, \langle z_l |\, e^{i\hat{H}t/\hbar} \,| q_l - \Delta_l/2 \rangle \end{aligned} \tag{3.22}$$

where

$$A(\mathbf{q}) = \frac{1}{N} \sum_{N} A_i(q), \qquad B(\mathbf{z}) = \frac{1}{N} \sum_{N} B_i(z) \tag{3.23}$$

In the limit $N \to \infty$ the sums in A($\mathbf{q}$) and B($\mathbf{z}$) become integrals and so this is just an alternative way of writing out the Kubo-transformed time correlation function. i.e.

$$\tilde{C}_{AB}(t) = \lim_{N\to\infty} C_{AB}^{[N]}(t) \tag{3.24}$$

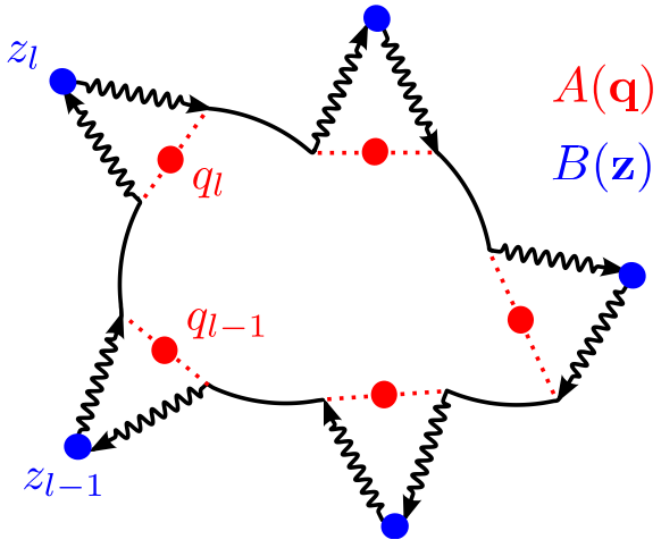

Figure 3.1: Schematic representation of the ring-polymer representation of the time correlation function as in Eq.(3.22) for $N = 5$. The red points represent q_l and the blue points z_l. Solid lines represent stretches of imaginary time of length $\beta_N\hbar$ and wavy arrows represent forward and backward propagations in real time. (Figure reproduced from ref. [73]).

The LSC-IVR approximation to the kubo-transformed TCF can be derived from Eq.(3.22). This can be thought of as a generalisation of the steps in Sec. (3.1.2) and (3.1.3). We summarise the results that arise from this. (Full details can be found in ref.[73]). In this representation the TCF can be written as

$$C_{AB}^{[N]}(t) = \frac{1}{(2\pi\hbar)^N} \int d\mathbf{q} \int d\mathbf{p}\, [e^{-\beta\hat{H}}\hat{A}]_{\overline{N}}(\mathbf{p},\mathbf{q})[\hat{B}(t)]_N(\mathbf{p},\mathbf{q}) \tag{3.25}$$

where

$$[e^{-\beta\hat{H}}\hat{A}]_{\overline{N}}(\mathbf{p},\mathbf{q}) = \int d\Delta\, A(\mathbf{q}) \prod_{l=1}^{N} \langle q_{l-1} - \Delta_{l-1}/2|\, e^{-\beta_N \hat{H}}\, |q_l + \Delta_l/2\rangle\, e^{ip_l\Delta_l/\hbar} \tag{3.26}$$

and

$$[\hat{B}(t)]_N(\mathbf{p},\mathbf{q}) = \int d\Delta \int d\mathbf{z}\, B(\mathbf{z}) \prod_{l=1}^{N} \langle q_l - \Delta_l/2|\, e^{-i\hat{H}t/\hbar}\, |z_l\rangle\, \langle z_l|\, e^{+i\hat{H}t/\hbar}\, |q_l + \Delta_l/2\rangle\, e^{ip_l\Delta_l/\hbar} \tag{3.27}$$

are generalised Wigner transforms. The Liouvillian operator can again be calculated for this TCF by differentiating with respect to time. This gives the Liouvillian operator as

$$\hat{L}_N = \sum_{l=1}^{N} \frac{p_l}{m}\frac{\partial}{\partial q_l} - V(q_l)\frac{2}{\hbar}\sin\left(\frac{\overleftarrow{\partial}}{\partial q_l}\frac{\hbar}{2}\frac{\overrightarrow{\partial}}{\partial p_l}\right) \tag{3.28}$$

we can again rewrite this Liouvillian as a classical term plus additional terms by expanding the sin function in powers of $\hbar^2$. Truncating the series at $\hbar^0$ returns the LSC IVR approximation at $N \to \infty$. The ring-polymer version of LSC-IVR thus approximates the dynamics of N independent particles with classical dynamics, initiated at phase-space points (p_l, q_l).

3.1.5 Limitations of LSC-IVR

As with all of the methods which are used to approximate quantum dynamics, there are limitations which arise due to the approximations made. The limitations which arise from LSC-IVR are briefly discussed below.

Being based on completely classical trajectories, the method fails to describe quantum recurrence/coherence effects. These effects are often important in few-dimensional systems; in condensed phase systems they are thought to be of less importance due to coupling of various degrees of freedom. Furthermore, it is unclear from LSC-IVR when and where these effects do become important. The Semi-Classical initial value representations can however provide a framework upon which

to improve upon LSC-IVR for longer time dynamics based on classical dynamics.[28]

It can be shown from the quantum commutation

$$\left[e^{-\beta\hat{H}}, e^{-i\hat{H}t/\hbar}\right] = 0 \tag{3.29}$$

that properties at thermal equilibrium are invariant with respect to time, i.e.

$$\left\langle \hat{B}(0) \right\rangle = \left\langle \hat{B}(t) \right\rangle \tag{3.30}$$

However, as mentioned above, LSC-IVR fails to conserve the Boltzmann distribution except in the harmonic limit, which leads to

$$\left\langle \hat{B}(0) \right\rangle \neq \left\langle \hat{B}(t) \right\rangle \tag{3.31}$$

for most thermal equilibrium properties.

This inability of LSC-IVR to conserve the distribution leads to the transfer of energy between inter and intra molecular modes in larger simulations of condensed phase systems such as liquid water and has been described as zero point energy leakage.

One of the biggest problems with the Linearised semi classical initial value representation is the concept of zero point energy leakage investigated by Habershon and Manolopoulos.[48] With LSC-IVR one runs purely classical trajectories from an initially quantized phase space distribution. In the case of liquid water, there is a large amount of energy which is quantized as zero point energy. However, once we allow the phase space distribution to evolve classically, this ZPE in the intramolecular modes can in principle leak out to the intermolecular modes which artificially heats these modes during the simulation. Nevetheless, for short time simulations the LSC-IVR with the LGA has been shown to be an extremely practical method for combining quantum statistics with classical dynamics;[29; 103] the method has been tested on large systems and is currently one of the front runners in the field along with RPMD and CMD.

3.1.6 Local Gaussian approximation

The Wigner function for the operator B is equivalent to the classical function B if it is a function of either position or momenta.[28] The more difficult task is the calculation of the Wigner transform of the operator A. This is because A involves the Boltzmann operator and so the total Hamiltonian of the complete system. Calculating this fourier transform becomes extremely difficult because it is an F-dimensional fourier transform (where F denotes the number of physical degrees of freedom) but is necessary to obtain the initial momenta distribution (P_0) for the real time trajectories. As a result, harmonic approximations are routinely made to LSC-IVR;[43–47] the most widely used of which is the LGA of Liu and Miller.[28; 32]

The LGA[32] is obtained for the momentum distribution by modification of the Local Harmonic approximation (LHA) of Shi and Geva.[104] The first step is to take the Wigner function of the Boltzmann operator $\mathbf{P}(x,p)$.

$$\mathbf{P}(x,p) = \int d\Delta x \left\langle x - \frac{\Delta x}{2} \right| e^{-\beta\hat{H}} \left| x + \frac{\Delta x}{2} \right\rangle e^{ip\Delta x/\hbar} \tag{3.32}$$

and then factor out the diagonal matrix elements of the operator

$$\mathbf{P}(x,p) = \langle x| e^{-\beta\hat{H}} |x\rangle \int d\Delta x \frac{\left\langle x - \frac{\Delta x}{2}\right| e^{-\beta\hat{H}} \left|x + \frac{\Delta x}{2}\right\rangle}{\langle x| e^{-\beta\hat{H}} |x\rangle} e^{ip\Delta x/\hbar} \tag{3.33}$$

Noting the following identities in the harmonic limit[104]

$$\langle x_1| e^{-\beta\hat{H}} |x_2\rangle = C \exp\left[-\frac{m\omega}{4\hbar}\left[(x_1^2+x_2^2)\tanh\left(\frac{\beta\hbar\omega}{2}\right) + (x_1^2-x_2^2)\coth\left(\frac{\beta\hbar\omega}{2}\right)\right]\right] \tag{3.34}$$

and

$$\langle x_1| e^{-\beta\hat{H}} |x_1\rangle = C \exp\left[-\frac{m\omega}{\hbar}\tanh\left(\frac{\beta\hbar\omega}{2}\right)x_1^2\right] \tag{3.35}$$

Where C is a proportionality constant independent of x_1 and x_2. The LHA is then made to the ratio of the off-diagonal to diagonal matrix elements in the integrand, i.e.

$$\frac{\left\langle x - \frac{\Delta x}{2}\right| e^{-\beta\hat{H}} \left|x + \frac{\Delta x}{2}\right\rangle}{\langle x| e^{-\beta\hat{H}} |x\rangle} \approx \exp\left[-\frac{m\omega}{4\hbar}\coth(\beta\hbar\omega/2)\Delta x^2\right] \tag{3.36}$$

where ω is the local frequency

$$\omega = \omega(x) = \sqrt{V''(x)/m} \tag{3.37}$$

Eq.(3.37) is exact in the harmonic limit in which the frequency is constant. With the LHA of Eq.(3.36) the Fourier integral in Eq.(3.33) can be evaluated to give the

LHA for the Wigner distribution function.[32]

$$\mathbf{P}(x,p) = \langle x|\, e^{-\beta\hat{H}}\, |x\rangle \left(\frac{\beta}{2m\pi Q(u)}\right)^{1/2} \exp\left[-\beta\frac{p^2}{2m}\frac{1}{Q(u)}\right] \tag{3.38}$$

where the quantum correction factor Q(u) is defined as

$$Q(u) = \frac{u/2}{\tanh[u/2]} \tag{3.39}$$

where u is the dimensionless parameter

$$u = \beta\hbar\omega \tag{3.40}$$

In the high temperature limit $\beta \to 0$, the classical limit $\hbar \to 0$ and the free particle limit $\omega \to 0$, $u \to 0$ which means that the quantum correction factor $Q(u) \to 1$ and so Eq.(3.36) gives the classical momentum distribution.

The local frequency ω is imaginary when $V''(x_0) < 0$ and so u becomes imaginary (i.e., $u = iu_i$ where $u_i = \beta\hbar|\omega|$). The quantum correction factor can then be written as

$$Q(u) \equiv Q(iu_i) = \frac{u_i/2}{\tan[u_i/2]} \tag{3.41}$$

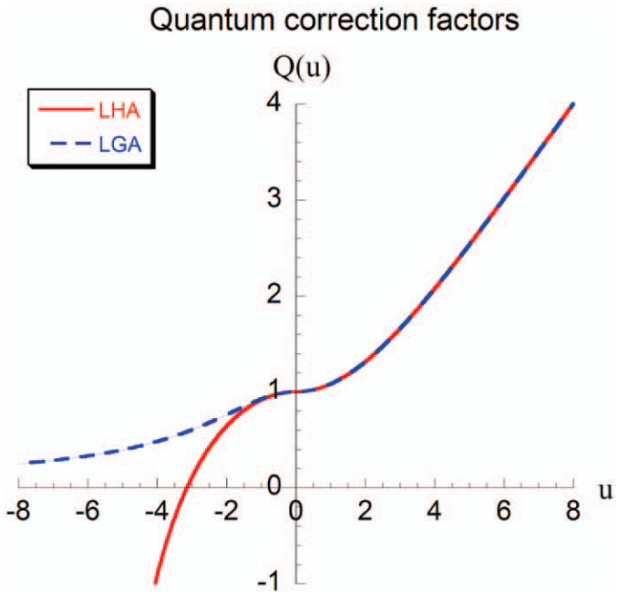

Figure 3.2: Quantum correction factor $Q(u = \beta\hbar\omega)$ for LHA (red) and LGA (blue dashed). Imaginary frequencies $i|\omega|$ are shown as $-|\omega|$ on the negative axis. Figure reproduced from ref.[32].)

As can be seen in Fig.(3.2) above, the LHA breaks down in the imaginary frequency regime in which $u_i > \pi$. One possible fix to this would be to simply set the quantum correction factor to 0, this would suggest that the momentum distribution in Eq.(3.38) would become infinitely narrow. In the low temperature regime, this Gaussian momentum distribution is expected to become increasingly narrow, however not infinitely narrow. As a result Liu and Miller suggest an alternate form of the Quantum correction factor (LGA) which decreases smoothly to zero beyond $u_i = \pi$. This is given as

$$Q(u) = \left[\frac{u/2}{\tanh(u/2)}\right] \text{ for real } u \tag{3.42}$$

$$Q(u) = \frac{1}{Q(u_i)} = \left[\frac{\tanh(u_i/2)}{u_i/2}\right] \text{ for imaginary } u(u = iu_i) \tag{3.43}$$

Liu and Miller have shown that the LGA modification to the LHA is successful at high temperatures and does well at low temperatures for problems dominated by imaginary frequencies.[32] It is important to note that this is a purely hueristic guess.

Generalisation to multidimensional systems

Since the LGA is a harmonic-like approximation one can use normal modes to generalise it to multiple dimensions.[28; 32] In normal mode analysis, the mass weighted Hessian matrix elements are given by

$$\mathbf{H}_{kl} = \frac{1}{\sqrt{m_k m_l}} \frac{\partial^2 V}{\partial x_k \partial x_l} \tag{3.44}$$

where m_k denotes the mass of the k^{th} degree of freedom. The eigenvalues of the mass weighted hessian matrix, produce normal mode frequencies ω_k, i.e.

$$\mathbf{T}^T \mathbf{H} \mathbf{T} = \boldsymbol{\lambda} \tag{3.45}$$

with $\boldsymbol{\lambda}$ a diagonal matrix with elements $(\omega_k)^2$ and $\mathbf{T}$ an orthogonal matrix. We denote $\mathbf{M}$ as the diagonal mass matrix with elements m_k. The mass-weighted normal-mode coordinates and momenta $(\mathbf{X}_0, \mathbf{P}_0)$ are given in terms of the Cartesian variables $(\mathbf{x}_0, \mathbf{p}_0)$ by

$$\mathbf{X}_0 = \mathbf{T}^T \mathbf{M}^{1/2} \mathbf{x}_0 \tag{3.46}$$

and

$$\mathbf{P}_0 = \mathbf{T}^T \mathbf{M}^{-1/2} \mathbf{p}_0 \tag{3.47}$$

respectively.

Liu and Miller have shown that for the LGA, the standard time correlation function for two operators $\hat{A}$ and $\hat{B}$ can be written as

$$C_{AB}^{\mathrm{LGA}}(t) = \int \mathbf{dx}_0 \left\langle \mathbf{x}_0 \right| e^{-\beta \hat{H}} \left| \mathbf{x}_0 \right\rangle \int \mathbf{dP}_0 \prod_{k=1}^{N} \left[\left(\frac{\beta}{2\pi Q(u_k)} \right)^{1/2} \times \exp\left[-\beta \frac{(P_{0,k})^2}{2Q(u_k)} \right] \right] f_A(\mathbf{x}_0, \mathbf{p}_0) B(\mathbf{x}_t, \mathbf{p}_t) \tag{3.48}$$

where the general expression for $f_A(\mathbf{x}_0, \mathbf{p}_0)$ can be found in ref.[32]. In this work, we are interested in calculating position autocorrelation functions, i.e. the case where $\hat{A} = \hat{B} = \hat{x}$. In this case [28]

$$f_A(\mathbf{x}_0, \mathbf{p}_0) = \mathbf{x}_0 + \frac{i\beta\hbar}{2} \mathbf{M}^{-1/2} \mathbf{T} \mathbf{Q}(\mathbf{u})^{-1} \mathbf{P}_0 \tag{3.49}$$

The correlation function in Eq.(3.48) is usually normalised by the partition function, i.e. we calculate $C_{AB}^{\mathrm{LGA}}(t)/Z$. The implementation of the LGA can be summarised as follows:

1. Use either path-integral molecular dynamics or path-integral Monte Carlo to simulate the system at equilibrium.

2. Randomly select one particular path-integral bead at a specific time in PIMD (or specific intervals in the case of PIMC) as the initial configuration x_0 for the real time dynamics.

3. Diagonalise the mass weighted hessian matrix of the potential energy surface to obtain the local normal mode frequencies.

4. Use the LGA to obtain the Gaussian distribution for the mass weighted normal mode momenta. This is used to sample the initial Cartesian momenta $p_0 = M^{1/2} T P_0$ for real time trajectories.

5. Run real time classical trajectories from phase space points (x_0, p_0) to obtain an estimate for $f_A(\mathbf{x}_0, \mathbf{p}_0) B(\mathbf{x}_t, \mathbf{p}_t)$

6. Repeat steps 2-5 and sum the property $f_A(\mathbf{x}_0, \mathbf{p}_0) B(\mathbf{x}_t, \mathbf{p}_t)$ until a converged result is obtained.

3.2 The Fitted Harmonic Approximation

The LGA has been the most successful and widely used approximation for making LSC-IVR practical. The method has been used to simulate relatively large systems including that of liquid water and ice.[32; 50] At present however, there are not many competing methods which can rival the LGA. This raises the question, is the LGA the best way in which LSC-IVR can be approximated? In this chapter we propose a new harmonic approximation to LSC-IVR, the fitted harmonic approximation (FHA). The method is implemented in 1D and 2D for some model systems and comparisons to the LGA are made.

3.2.1 Theory

In this section, we outline the theory behind the FHA. In the harmonic limit, the momentum distribution is proportional to

$$\exp\left(-\frac{1}{m\omega\hbar}\tanh\left(\frac{\beta\hbar\omega}{2}\right)p^2\right) \tag{3.50}$$

and the position distribution can be written as

$$\exp\left(-\frac{m\omega}{\hbar}\tanh\left(\frac{\beta\hbar\omega}{2}\right)q^2\right) \tag{3.51}$$

We first begin with the density matrix

$$\gamma(q,\beta) = \langle q|\, e^{-\beta\hat{H}}\, |q\rangle \tag{3.52}$$

inserting the identity, this can be written as

$$\gamma(q,\beta) = \sum_n \langle q|n\rangle \langle n|q\rangle\, e^{-\beta E_n} \tag{3.53a}$$

$$= \sum_n e^{-\beta E_n} |\psi_n(q)|^2 \tag{3.53b}$$

i.e. a sum of the square of the wavefunctions for a particular system multiplied by a Boltzmann weighting. In the harmonic limit this is equal to the expression for the position distribution in Eq.(3.51). i.e.

$$\gamma(q,\beta) = \sum_n e^{-\beta E_n} |\psi_n(q)|^2 = \exp\left(-\frac{m\omega}{\hbar}\tanh\left(\frac{\beta\hbar\omega}{2}\right)q^2\right) \tag{3.54}$$

Taking the natural logarithm and differentiating with respect to q twice gives

$$-\frac{\partial^2 \ln(\gamma(q,\beta))}{\partial q^2} = -\frac{\partial^2 \ln\left(\sum_n e^{-\beta E_n}|\psi_n(q)|^2\right)}{\partial q^2} = \frac{2m\omega}{\hbar}\tanh(\beta\hbar\omega/2) \tag{3.55}$$

i.e. a nonlinear equation involving ω which can be solved numerically. In the FHA we present this as an alternate way in which the local frequency ω can be calculated in the momentum distribution (Eq.(3.50)) in a LGA-type calculation instead of the local second derivative (in 1D) or hessian matrix (in multidimensions). (This replaces step 3 in the LGA implementation described above in section (3.1.6)).

3.2.2 One-Dimensional Implementation

In the following section we outline the steps involved in the implementation of the FHA using the harmonic oscillator as a test system. For the harmonic oscillator, the analytical results are known, thus the implementation of the method can be verified. We use the DVR of Colbert and Miller on an equally spaced grid[2] to calculate the wavefunctions $\Psi_n(q)$ and the corresponding energies E_n required to calculate quantity $\gamma(q,\beta)$. Note that in addition to being system dependent, this quantity is also temperature (β) dependent. In contrast to the LGA of Liu and Miller,[32] the FHA will result in frequencies which are temperature dependent. For both the high temperature ($\beta = 1$) and the low temperature case ($\beta = 8$) we compute $\gamma(q,\beta = 1)$ Fig.(3.3) and $\gamma(q,\beta = 8)$ Fig.(3.4) shown below.

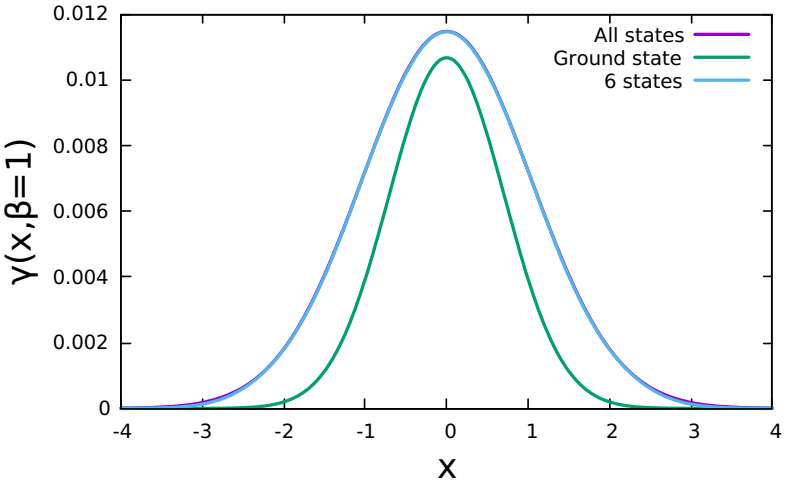

Figure 3.3: Plot of $\gamma(q,\beta = 1)$ vs q for the harmonic oscillator.

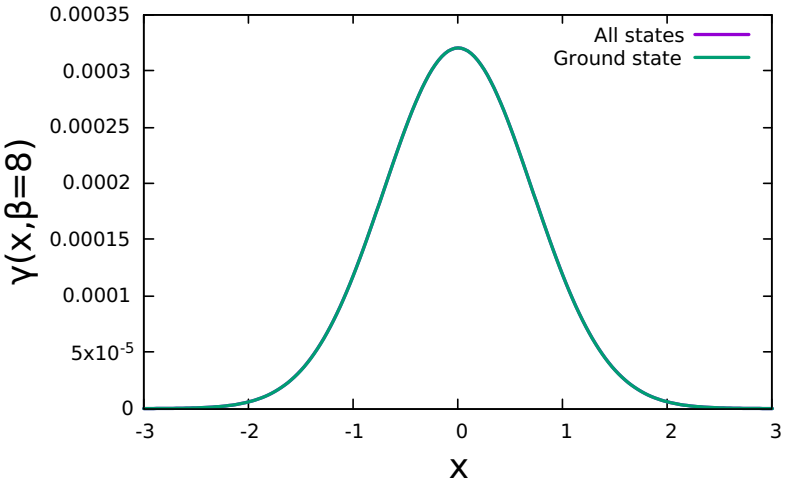

Figure 3.4: Plot of $\gamma(q,\beta = 8)$ vs q for the for the harmonic oscillator, both curves show agreement and lie on top of each other.

We find that in the low temperature case (Fig.(3.4)), $\gamma \to 0$ at approximately $q = \pm 2$ whereas for the high temperature (Fig.(3.3)) case this is $q = \pm 4$. This can be understood because the Boltzmann factor in the calculation of γ is temperature dependent. At low temperature, this Boltzmann weighting quickly removes contributions in the sum due to excited states and only the first harmonic oscillator wavefunction contributes to γ. In contrast, at high temperatures the particle has an increased amount of energy and so is more likely to be described by excited state wavefunctions. In terms of γ, the weighting of the states due to the Boltzmann factor more slowly dampens off the higher energy excited states. Fig.(3.4) shows that at low temperature, γ is described by the ground state alone, whereas at high temperature (Fig.(3.3)), the ground state and the first five excited states are required to achieve graphical convergence.

For a given temperature the natural logarithm of γ is then computed at each grid point. Shown for the high temperature case in Fig(3.5).

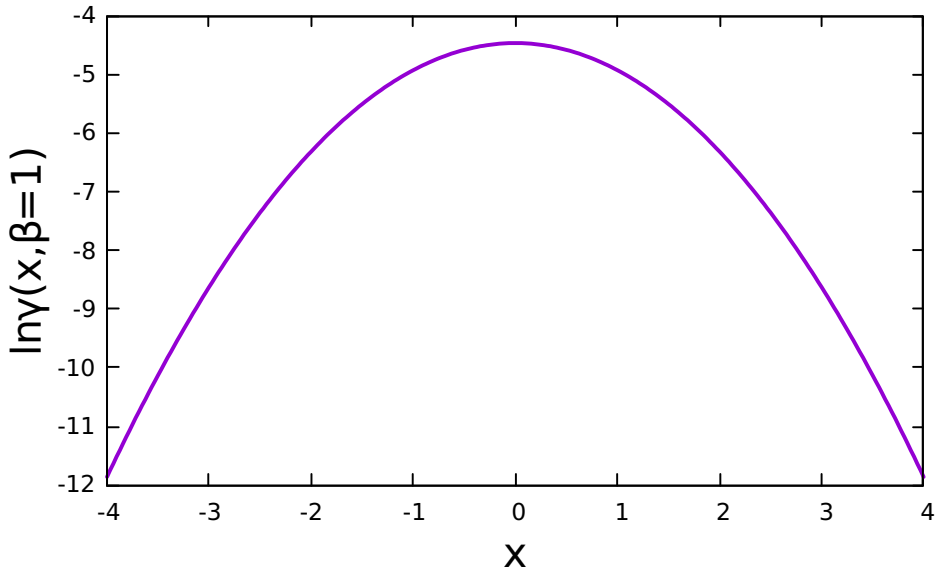

Figure 3.5: $\ln\gamma$ vs x calculated across the grid for the high temperature ($\beta = 1$) case.

A cubic spline is then fitted to this data (using the Scipy.Interpolate.Cubicspline package), this package is used to numerically calculate and return the second derivative. Once the the negative of the second derivative has been calculated, Eq.(3.55) is solved numerically for ω at each point along the grid using the 'nsolve' procedure in python. This requires a starting guess for the solution which if selected poorly can increase computational effort or lead to the procedure failing to converge to a solution. When calculating ω we restrict the calculations to regions to which γ is non-negligible (i.e. for $|x| < 5$), this is due to numerical instabilities (wiggles) which

occur when calculating the logarithm and second derivative of the logarithm of extremely small numbers outside of this region. In the Harmonic limit, the analytic expression for the frequency is $\omega = \sqrt{k/m}$. For the potential $V(x) = 1/2x^2$ with $m = 1$ this is simply equal to 1. As expected, the FHA is able to calculate the exact frequencies in this limit. The frequencies obtained using the FHA are then used in an LGA-type calculation to calculate position autocorrelation functions. The quantum results presented in this chapter are calculated on an equally spaced DVR grid as described in [Appendix A.1].

3.2.3 Anharmonic Test Systems

By construction, the FHA is exact in the harmonic limit. We proceed by testing the FHA on the following anharmonic test potentials and draw comparisons between the results obtained relative to the LGA.

Mildly anharmonic oscillator

We first test the method on the mildly anharmonic oscillator, $V(x) = \frac{1}{2}x^2 + \frac{1}{10}x^3 + \frac{1}{100}x^4$. Applying the same procedure as with the harmonic system we calculate $\gamma(q, \beta)$ at high temperature (Fig.(3.6) and low temperature (Fig.(3.7)).

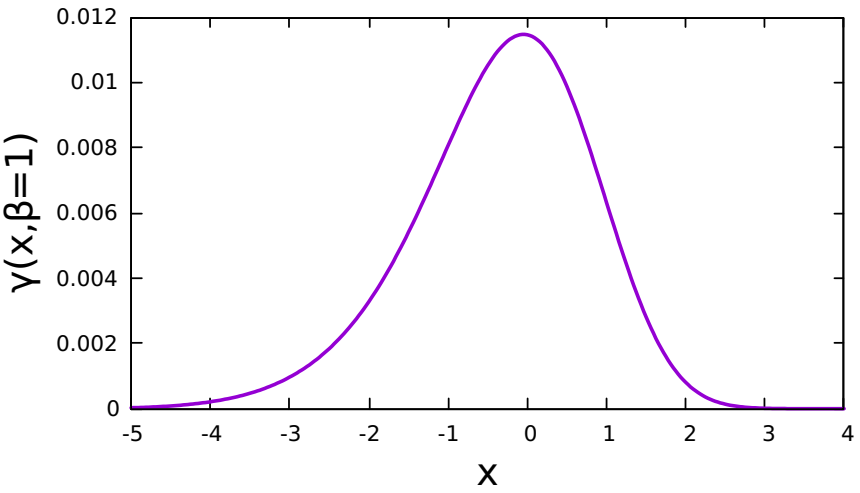

Figure 3.6: $\gamma(q, \beta = 1)$ calculated across the grid for the mildly anharmonic oscillator.

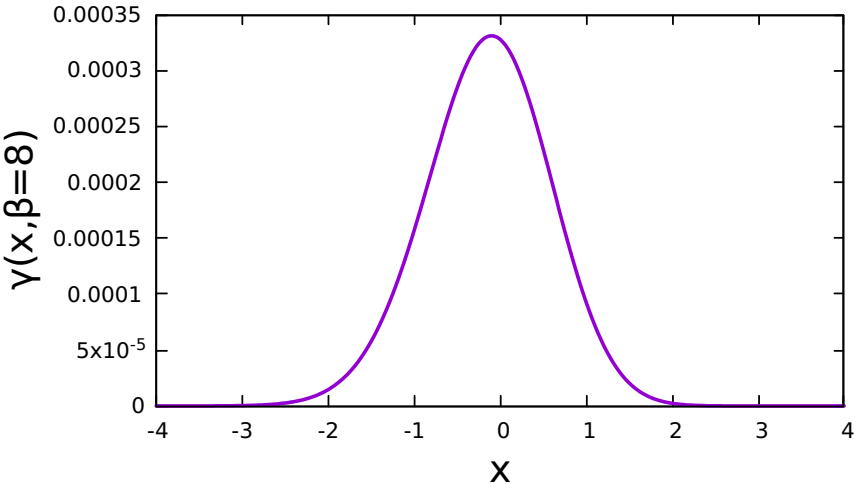

Figure 3.7: $\gamma(q, \beta = 8)$ calculated across the grid for the mildly anharmonic oscillator.

As with the harmonic potential, γ appears to be centred on 0 and tends towards

zero relatively quickly (by approximately ±3). In contrast to the harmonic case, as this potential is not symmetric about 0, γ is also not symmetric.

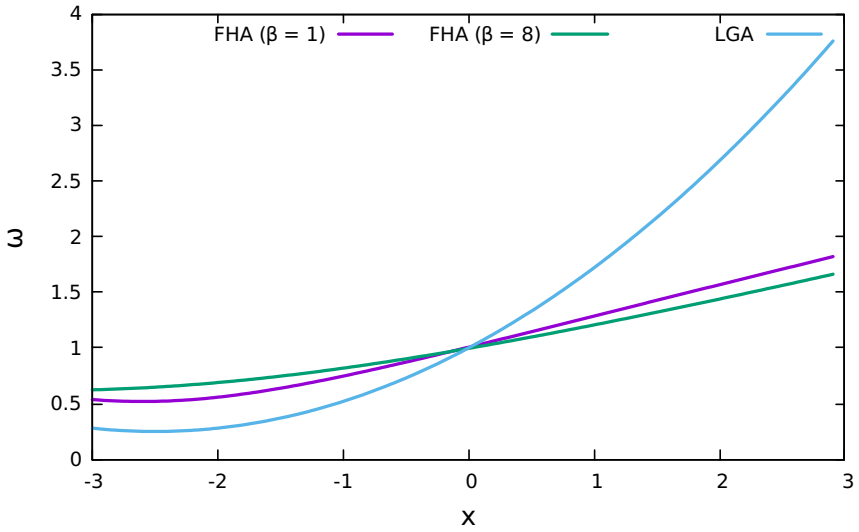

Figure 3.8: Calculated values of ω for the FHA at high temperature (purple), low temperature (green) and the LGA result (blue).

We then calculate ω at high and low temperature and compare the result obtained from the FHA at both temperatures with the LGA frequency in Fig.(3.8). Fig.(3.8) shows that the LGA result has a minimum at a lower value relative to the FHA results, furthermore the calculated value of ω for the FHA rises much more slowly with increasing x when compared to the LGA. From Figs.(3.6 and 3.7) it is clear that for this system, most of the particles will be in the region ±2. Comparing the LGA frequencies with that of the FHA Fig.(3.8), in the region $|x| < 2$ we find that they are quite similar when compared to that of the strongly anharmonic oscillator (discussed in the next section) and so we would expect the dynamics in an LGA-type calculation using the FHA frequencies to be quite similar to that of the standard LGA implementation.

The position auto-correlation functions are computed for both the low (Fig.(3.9)) and high temperature (Fig.(3.10)) limits and compared to the Quantum, LSC-IVR and LGA results. For both the FHA and LGA calculations, we use 64 and 128 path-integral beads for the high and low temperature limits respectively with 100,000 trajectories used in both. In the calculation of the LSC-IVR TCF, the Wigner transforms are evaluated using the eigenfunctions and eigenvectors from an equally spaced DVR of Colbert and Miller with $N = 1000$. This gives a function $f(q, \Delta)$ which is Fourier transformed to give $f(p, q)$. $f(p, q)$ is propagated throughout time using the velocity-Verlet algorithm with a time step of 0.01 a.u. and rectangular quadrature is used in the calculation of the integrals.

In the high temperature limit, (Fig.(3.10)) at short times the TCFs computed for all of the methods follow the quantum result closely. At longer times ($t > 12$), the amplitudes of the peak for all of the methods (LSC-IVR, LGA and the FHA) decay faster than that of the quantum result. It is also noted that the FHA agrees quite closely with the LGA result. In the low temperature case, (Fig.(3.9)) shows that all of the approximate methods give a similar result with the peaks occurring at the correct time but decaying in amplitude too quickly when compared to the quantum TCF.

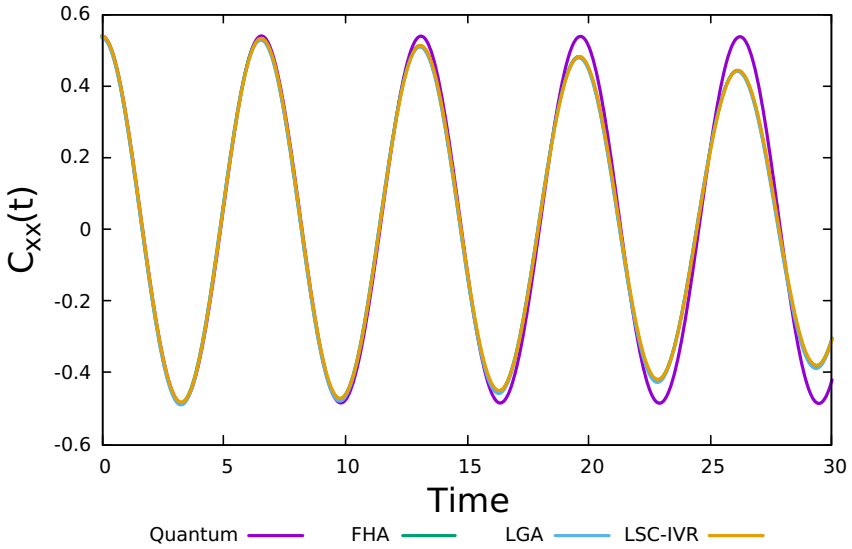

Figure 3.9: Position time correlation function for the mildly anharmonic oscillator at low temperature, $\beta = 8$. Quantum (purple), FHA (green), LGA (blue), LSC-IVR (yellow).

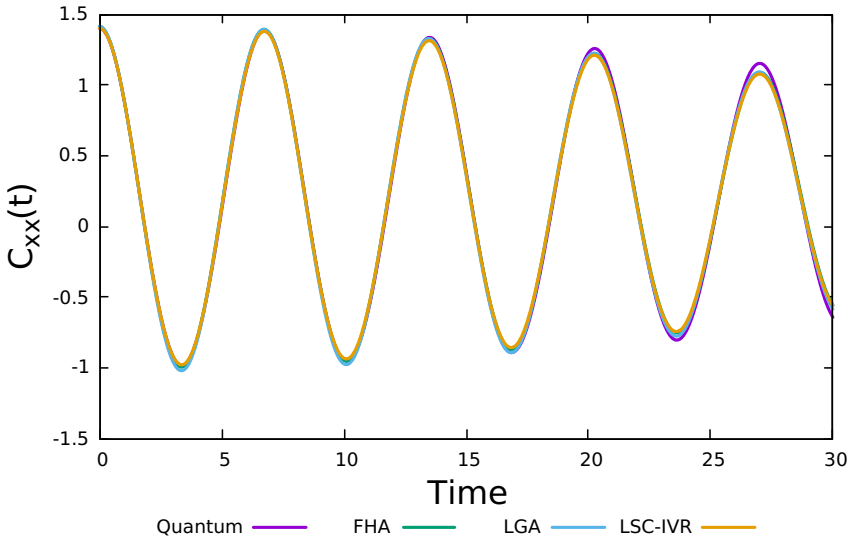

Figure 3.10: Position time correlation function for the mildly anharmonic oscillator at high temperature, $\beta = 1$. Quantum (purple), FHA (green), LGA (blue), LSC-IVR (yellow).

Strongly anharmonic oscillator

The second test system is the strongly anharmonic system $V(x) = \frac{1}{4}x^4$ which path-integral based techniques are known to perform poorly for. The potential is quite flat with steep walls and so it is expected that quantum coherence effects (which path integral-based methods completely neglect) become important, i.e. the quantum statistics alone are not sufficient to capture the important quantum effects.

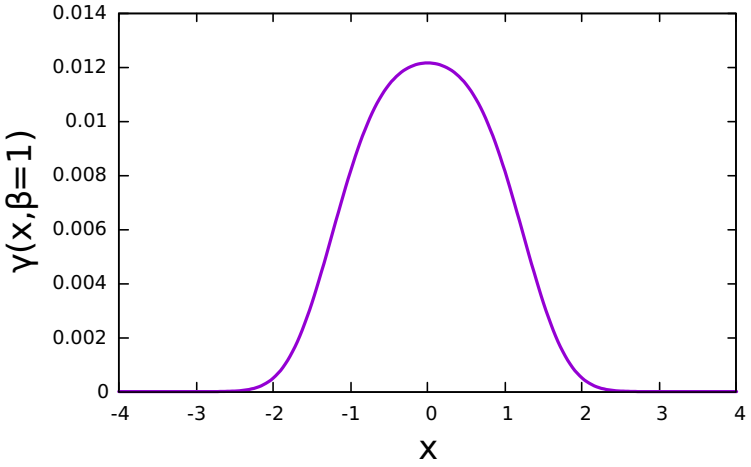

Figure 3.11: γ calculated across the grid for the strongly anharmonic oscillator at high temperature ($\beta = 1$).

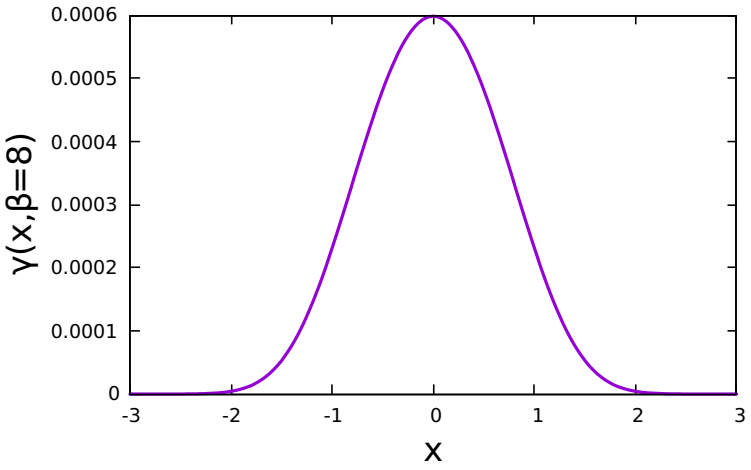

Figure 3.12: γ calculated across the grid for the strongly anharmonic oscillator at low temperature ($\beta = 8$).

Gamma is computed at high (Fig.(3.11)) and low (Fig.(3.12)) temperature. For this test system, the shape of the curve is broad in the centre and tends towards 0 quite sharply (in particular at $\beta = 1$) as one may expect from the shape of the potential. The shape of the curve is significantly different to that of the harmonic

oscillator (Fig.(3.3)), as a result, we expect that applying a harmonic approximation such as the FHA or the LGA to this test system will give relatively poor results when compared to the quantum result.

Calculating the log and the second derivatives of γ lead to the same numerical instabilities in regions where γ becomes vanishingly small as previously discussed in the harmonic implementation. As this potential is symmetric, we find that the second derivative of $ln\gamma$ is also symmetric and centred on 0. For this test system, a comparison of the frequencies obtained relative to the LGA Fig.(3.13) is quite interesting. It can be seen that the frequencies used in the LGA (the second derivative of the potential) has zero magnitude at $x = 0$ and rises much more steeply relative to the FHA. The FHA curves however are non zero at $x = 0$ and rise much more slowly. A comparison of the FHA frequency curves for the high T and low T Fig.(3.14), show that the curves agree quite well however the high T limit has a slightly lower frequency at $x = 0$ and then rises more quickly as $|x|$ increases.

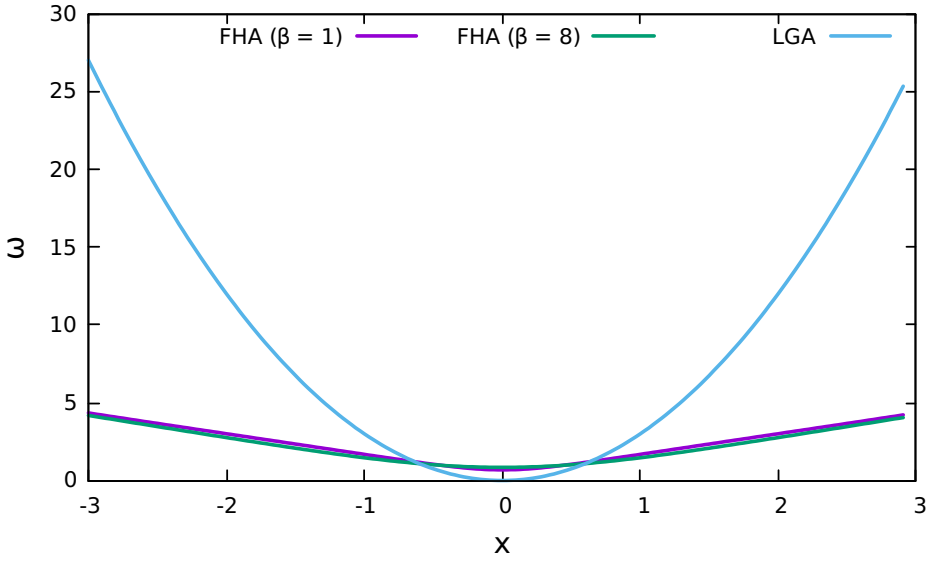

Figure 3.13: Calculated values of ω for the FHA at both high temperature (purple), low temperature (green) and the LGA result (blue).

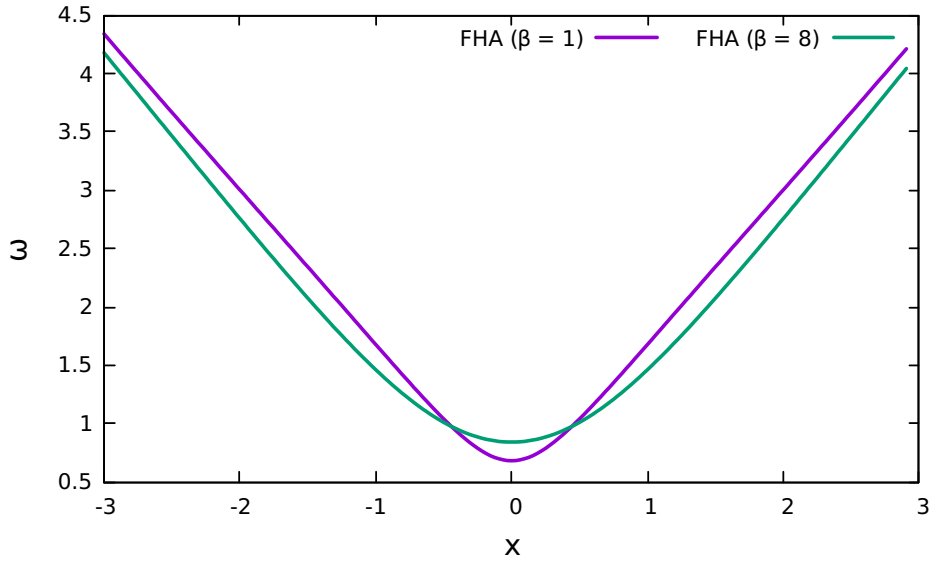

Figure 3.14: Enhanced image showing the calculated values of ω for the FHA at both high temperature (purple) and low temperature (green).

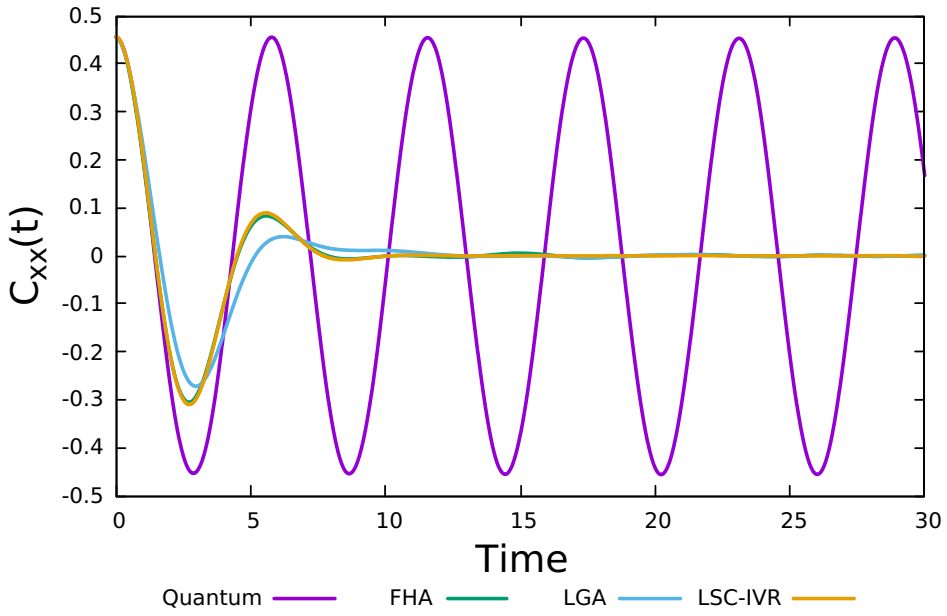

Figure 3.15: Position time correlation function for the strongly anharmonic oscillator at low temperature, $\beta = 8$. Quantum (purple), FHA (green), LGA (blue), LSC-IVR (yellow).

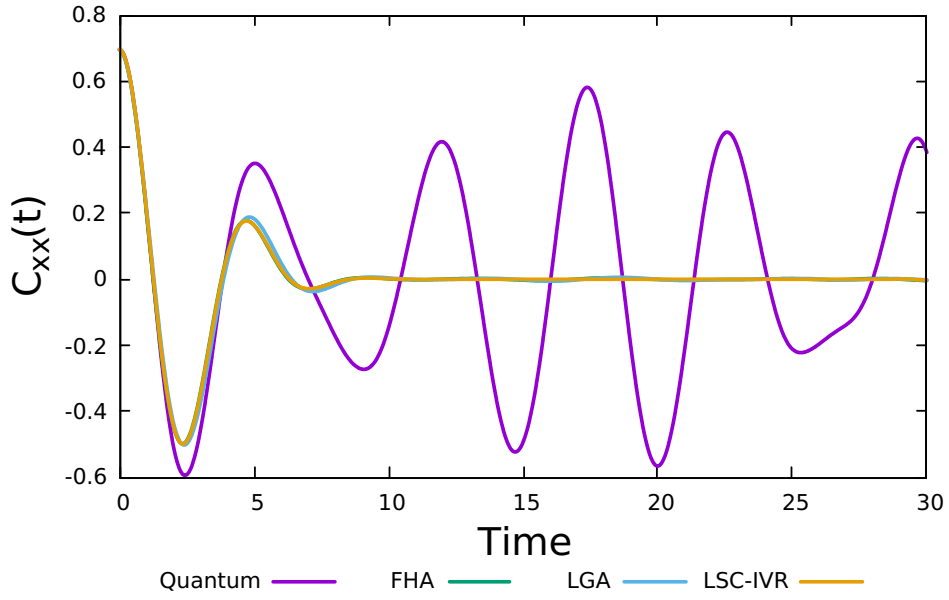

Figure 3.16: Position time correlation function for the strongly anharmonic oscillator at high temperature, $\beta = 1$. Quantum (purple), FHA (green), LGA (blue), LSC-IVR (yellow).

Interestingly, the position autocorrelation functions show that at low temperature (Fig.(3.15)), the FHA has better agreement with the LSC-IVR result and is slightly better than the LGA result which flattens out more quickly. None of the approximations are able to replicate the recurring oscillations seen in the quantum result which are due to wavepackets colliding with the steep wall. At high temperature (Fig.(3.16)) all of the approximations agree to a similar extent, overall there is very little difference seen in the result between the LGA and the FHA. We have seen that the frequency calculated for the FHA appears to be different to that in the LGA, in practise the use of the FHA frequencies results in position auto-correlation functions which agree closely or improve upon the LGA result.

Morse test system

When tested on the mildly anharmonic oscillator and the quartic oscillator the FHA is able to give results which are comparable to if not better than the LGA. More realistic systems fall in between these two limits, we therefore consider a Morse oscillator of the form

$$V(x) = D_e(1 - e^{-\alpha x})^2 \tag{3.56}$$

With $D_e = 15, m = 1$ and $\alpha = 0.1$ a.u.

We consider this Morse test system at high ($\beta = 2$) and low ($\beta = 8$) temperature and compare the computed FHA TCFs to the quantum, LSC-IVR and LGA result. Fig. (3.17) shows γ at both high temperature (purple) and low temperature (green). At high temperature γ appears to be more asymmetric relative to the low temperature case, this is due to the particle having an increased amount of energy and so accessing regions of the potential which are increasingly anharmonic. In Fig.(3.18) the frequencies obtained for the FHA at both $\beta = 2$ and $\beta = 8$ are plotted alongside the LGA result. The LGA frequency more steeply declines with increasing x relative to the FHA curves.

In Fig.(3.19) the computed position autocorrelation functions at high temperature are shown. The results show that the LGA underestimates the trough positions relative to the quantum result, LSC-IVR agrees more closely with the quantum result and at short time $t < 20$ agrees almost almost perfectly. Remarkably, it can be seen that the use of the FHA frequencies improves upon the LGA result with very good agreement seen with the quantum and the LSC-IVR result. The same pattern is also observed at low temperatures (Fig.(3.20)). This result strengthens our prior conclusion that the FHA frequencies result in TCFs which agree as well as, if not better than, the LGA when compared to the quantum result.

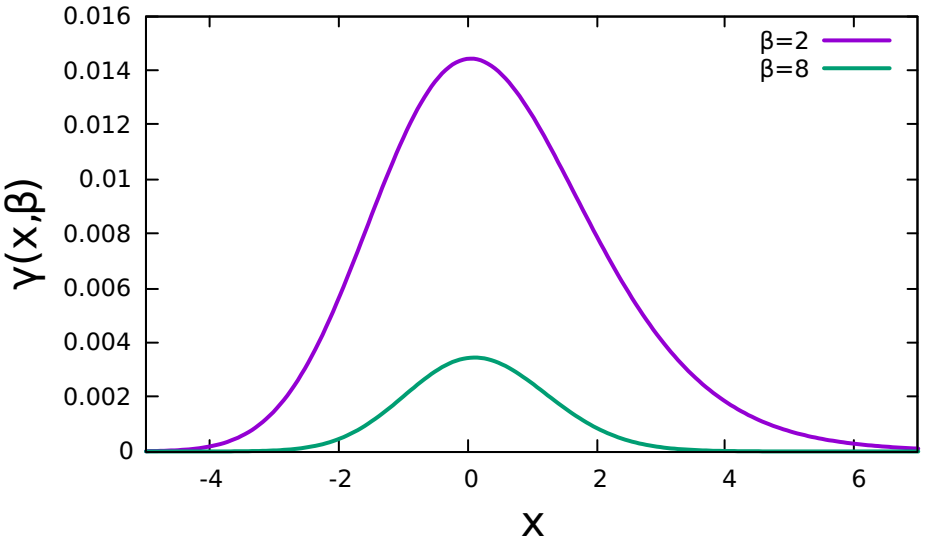

Figure 3.17: γ calculated across the grid for the Morse oscillator at high temperature (purple) and low temperature (green).

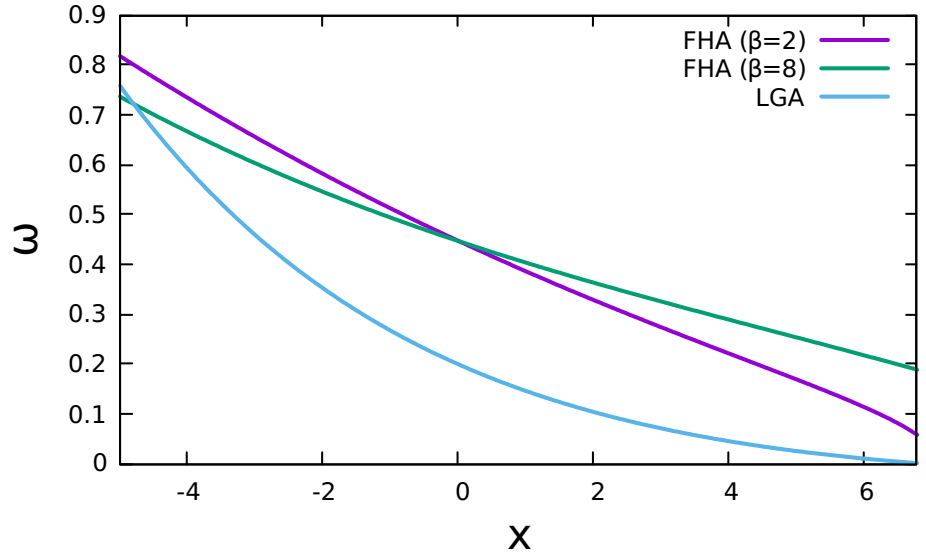

Figure 3.18: Calculated values of ω for the FHA at high temperature (purple), low temperature (green) and the LGA result (blue).

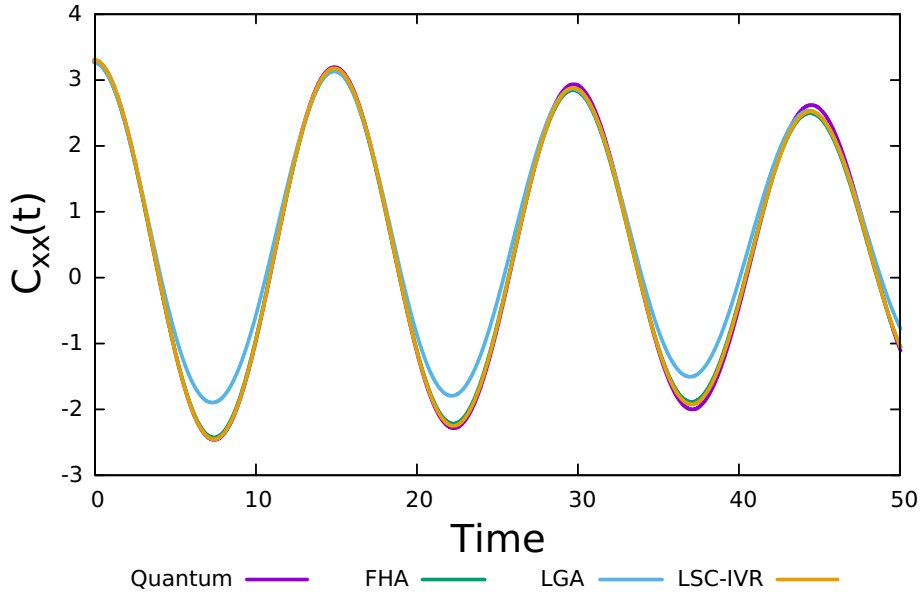

Figure 3.19: Position time correlation function for the Morse oscillator at high temperature, $\beta = 2$. Quantum (purple), FHA (green), LGA (blue), LSC-IVR (yellow).

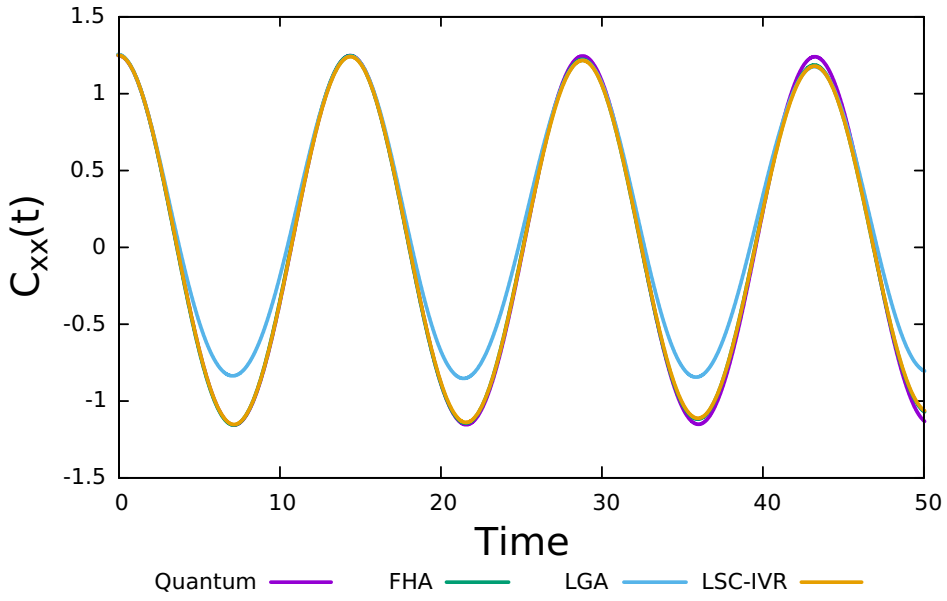

Figure 3.20: Position time correlation function for the Morse oscillator at low temperature, $\beta = 8$. Quantum (purple), FHA (green), LGA (blue), LSC-IVR (yellow).

3.2.4 Two-Dimensional Implementation

In this section we present the generalisation of the FHA to 2D. The density matrix is now a function of 2 Cartesian coordinates (x and y) and is written as follows:

$$\gamma(q,\beta) = \langle xy|\, e^{-\beta\hat{H}}\, |xy\rangle \tag{3.57a}$$

$$= \sum_n e^{-\beta E_n} |\psi_n(x,y)|^2 \tag{3.57b}$$

Analogous to the 1D case we take the negative log of this quantity. In 2D the second derivative can be calculated with respect to each of the Cartesian coordinates, i.e a hessian matrix is constructed.

$$\Gamma = -\begin{pmatrix} \frac{\partial^2 \ln(\gamma(xy,\beta))}{\partial x^2} & \frac{\partial^2 \ln(\gamma(xy,\beta))}{\partial x \partial y} \\ \frac{\partial^2 \ln(\gamma(xy,\beta))}{\partial y \partial x} & \frac{\partial^2 \ln(\gamma(xy,\beta))}{\partial y^2} \end{pmatrix} \tag{3.58}$$

which is then diagonalised

$$\begin{pmatrix} A_1 & 0 \\ 0 & A_2 \end{pmatrix} \tag{3.59}$$

returning the eigenvalues denoted by A_1 and A_2. These eigenvalues are then used to solve for $\omega_{1/2}$ as in the 1D case by numerically solving

$$-\frac{\partial^2 \ln(\gamma(q,\beta))}{\partial q^2} = \frac{2m\omega_{1/2}}{\hbar}\tanh(\beta\hbar\omega_{1/2}/2) = A_{1/2} \tag{3.60}$$

In the multidimensional case, the eigenvectors need to be retained for the transformation of the momenta from Cartesian to normal modes (in the 1D case these eigenvectors are trivially equal to 1). We can not precompute omega along the surface, but calculate it on the fly and keep the eigenvectors. The computational cost of the method increases steeply due to the increase in dimensionality of the problem, the need to numerically solve for additional frequencies at each point and the need to calculate the frequencies on the fly. In its current implementation the wavefunctions and corresponding eigenvalues are computed using a 2D equally spaced DVR grid. As a result, the scaling of the method from 1D to 2D causes the method to become significantly more expensive and difficult to implement and so is unlikely to be able to be extended to larger systems beyond 2D in its current form. This generalisation however, acts as a proof of principle in the extension of the method beyond 1D.

The Harmonic limit

We begin by first implementing the FHA to the two dimensional harmonic oscillator $V(x,y) = x^2 + y^2/2$. In the harmonic limit, the density matrix can be separated into a product of its Cartesian coordinates, this is shown as follows. Starting with the density matrix:

$$\gamma^{harmonic}(q,\beta) = \langle xy|\, e^{-\beta\hat{H}}\, |xy\rangle \tag{3.61a}$$

$$\gamma(q,\beta) = \sum_n \langle xy|n\rangle \langle n|xy\rangle\, e^{-\beta E_{nxy}} \tag{3.61b}$$

$$= \sum_n e^{-\beta E_n} |\psi_n(x,y)|^2 \tag{3.61c}$$

In the harmonic limit, the following relations apply: The total 2D wavefunctions can be constructed as a product of the 1D wavefunctions

$$\psi_n(x,y) = \psi_l(x)\psi_m(y) \tag{3.62a}$$

and the total energy can be written as a sum of the energies in 1D, i.e.

$$E_{nxy} = E_{lx} + E_{my} \tag{3.62b}$$

The density matrix can therefore be written as

$$\gamma(q,\beta) = \sum_l \sum_m e^{-\beta(E_{lx}+E_{my})} |\psi_l(x)\psi_m(y))|^2 \tag{3.63a}$$

$$= \sum_{n_x} e^{-\beta E_{nx}} |\psi_{nx}(x)|^2 \sum_{n_y} e^{-\beta E_{ny}} |\psi_{ny}(y)|^2 \tag{3.63b}$$

$$= \langle x|\, e^{-\beta\hat{H}}\, |x\rangle \langle y|\, e^{-\beta\hat{H}}\, |y\rangle \tag{3.63c}$$

$$= \gamma_x \gamma_y \tag{3.63d}$$

Making use of equation (3.63d) allows for the calculation of the surface γ in 2D to be calculated on a finer grid and allows for the verification of the code in 2D.

3.2.5 Harmonic calculations

In Fig.(3.21) we show the quantity γ for the harmonic case, this is now a function of two coordinates and so is represented by a surface rather than a curve. The two-

dimensional eigenvalues and eigenvectors are calculated using a DVR with equally spaced grid points in both the x and y directions. γ is then constructed as described by Eq.(3.61c). To further verify this approach, the surface is also constructed as a direct product of $\gamma(x)\gamma(y)$ (Eq.(3.63d)). As expected, in this limit both methods give identical results. In Fig.(3.22) $\ln\gamma$ is calculated, in the 1D case wiggles are seen in regions which $\gamma \to 0$, the surfaces also exhibits these wiggles. In the figure below we restrict $\ln\gamma$ to the regions in which these wiggles are absent.

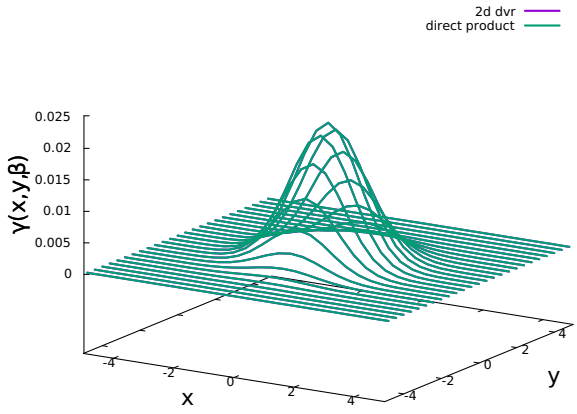

Figure 3.21: $\gamma(x, y, \beta = 1)$ for the harmonic oscillator. γ constructed using a 2D DVR (purple) and a product of a 1D DVR (green).

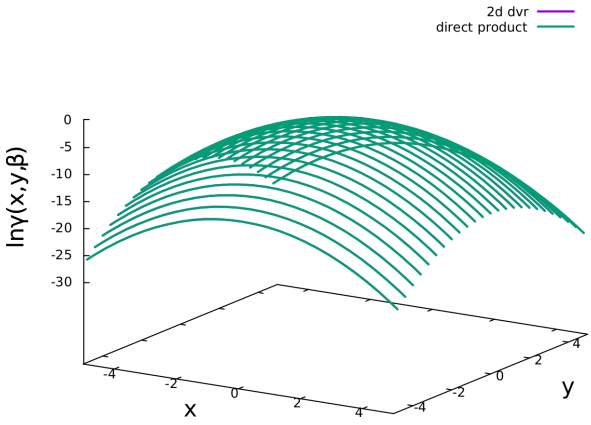

Figure 3.22: $\ln\gamma(x, y, \beta = 1)$ using a 2D DVR (purple) and direct product (green).

The position autocorrelation functions have been calculated in both the high temperature and the low temperature limit and reproduce the exact result (not shown). For the calculation of both the FHA and LGA results in 2D, at $\beta = 1$ we

use 64 path-integral beads, for $\beta = 8$ we use 128 path-integral beads with 100,000 trajectories.[105]

Constructing second derivatives

In the 2D FHA calculations, we find that in cases in which γ becomes vanishingly small (approaching machine precision) that the numerical second derivative of $\ln\gamma$ (calculated using numpy.gradient) can cause numerical difficulties. One way in which this is overcome is to calculate the second derivatives in the hessian using the following relation:

$$\frac{\partial \ln\gamma}{\partial x} = \frac{1}{\gamma}\frac{\partial \gamma}{\partial x} \tag{3.64}$$

as a result, the diagonal elements of the hessian matrix can be written as

$$\frac{\partial^2 \ln\gamma}{\partial x^2} = \frac{-1}{\gamma^2}\left(\frac{\partial \gamma}{\partial x}\right)^2 + \frac{1}{\gamma}\frac{\partial^2 \gamma}{\partial x^2} \tag{3.65}$$

and the off diagonal hessian matrix elements can be written as

$$\frac{\partial^2 \ln\gamma}{\partial x \partial y} = \frac{-1}{\gamma^2}\left(\frac{\partial \gamma}{\partial x}\right)\left(\frac{\partial \gamma}{\partial y}\right) + \frac{1}{\gamma}\frac{\partial^2 \gamma}{\partial x \partial y} \tag{3.66}$$

3.2.6 Anharmonic Test Systems

Mildly anharmonic potential

In this section, we test the method on two further anharmonic test potentials. The first of which is a 2D mildly anharmonic potential given by

$$V(x,y) = x^2/2 + x^3/10 + x^4/100 + y^2/2 + y^3/10 + y^4/100 + xy/100 \tag{3.67}$$

We follow the same process as described for the harmonic test systems. At high temperature (Fig.(3.23)) the FHA TCF agrees very closely with the LGA result and both methods closely follow the quantum result. In the low temperature case (Fig.(3.24)), the FHA and LGA both agree with the quantum result at short times ($t < 10$). At longer times, the amplitude of both the FHA and LGA peaks decay quicker than the exact quantum result but the FHA result agrees slightly better than the LGA result. As with the 1D results, the use of the frequencies computed in the FHA results in TCFs which are comparable to the LGA.

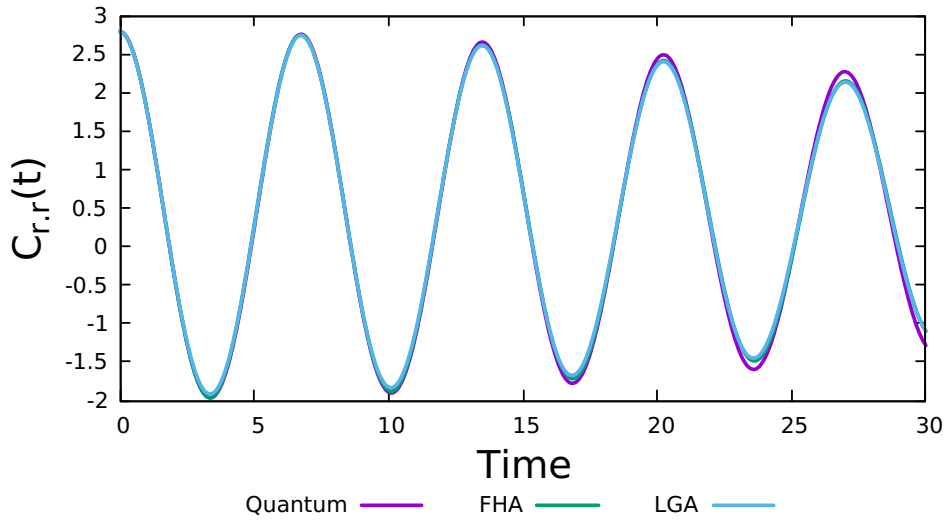

Figure 3.23: Position time correlation function for the two-dimensional mildly anharmonic oscillator at high temperature, $\beta = 1$. Quantum (purple), LGA (blue) and FHA (green).

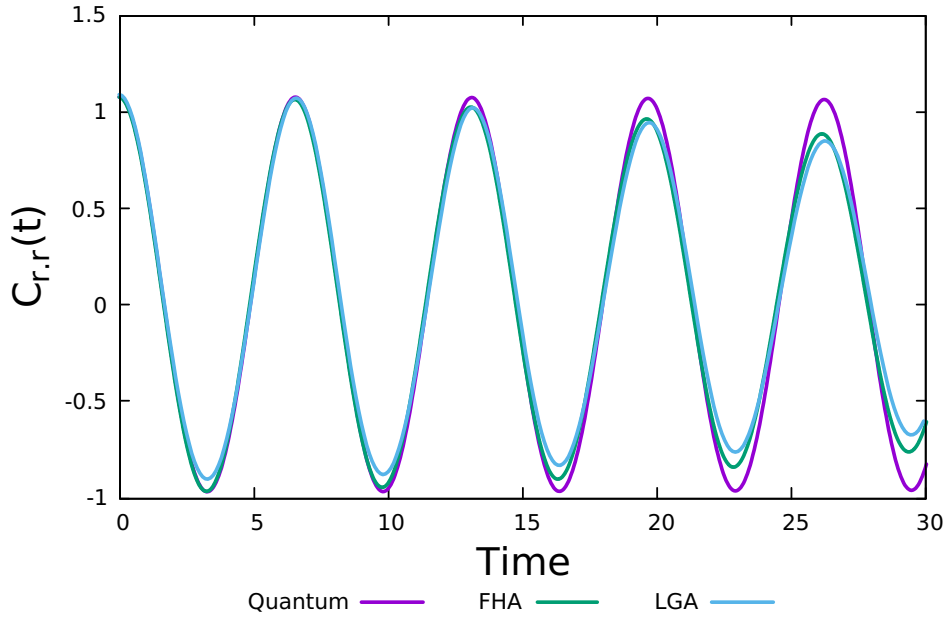

Figure 3.24: Position time correlation function for the two-dimensional mildly anharmonic oscillator at low temperature, $\beta = 8$. Quantum (purple), LGA (blue) and FHA (green).

Strongly anharmonic potential

The second test potential which we consider is the two-dimensional strongly anharmonic potential given by

$$V(x, y) = x^4/4 + y^4/4 + x^2y^2/100 \tag{3.68}$$

At high temperature Fig.(3.25), both the LGA and FHA TCFs follow each other quite closely. When compared to the quantum result, the FHA and LGA is only able to correctly predict the TCF for short periods of time due to the method only capturing quantum statistical effects and neglecting quantum coherence effects. At low temperature Fig.(3.26), the FHA and LGA only agree with the quantum result for very short times, the reasons why this occurs are the same as in the high temperature case. Arguably, the result obtained from the FHA offers a marginal improvement over the LGA. This result in combination with the 1D results leads us to question the choice of the local second derivative in the calculation of the frequency used in the LGA and whether this is the best way in which LSC-IVR can be approximated. The difficulties presented in the implementation of the FHA compared to the the LGA make it unlikely that it will act as a direct competitor to the LGA in its current form, however the results obtained thus far could motivate further work in investigating the choice of frequencies used in an LGA type approximation to LSC-IVR.

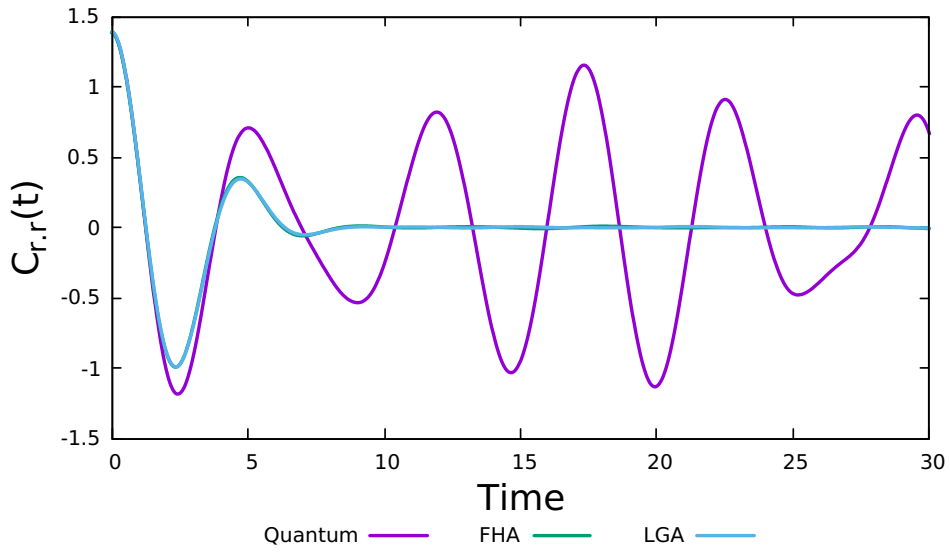

Figure 3.25: Position time correlation function for the two-dimensional strongly anharmonic oscillator at high temperature, $\beta = 1$. Quantum (purple), LGA (blue) and FHA (green).

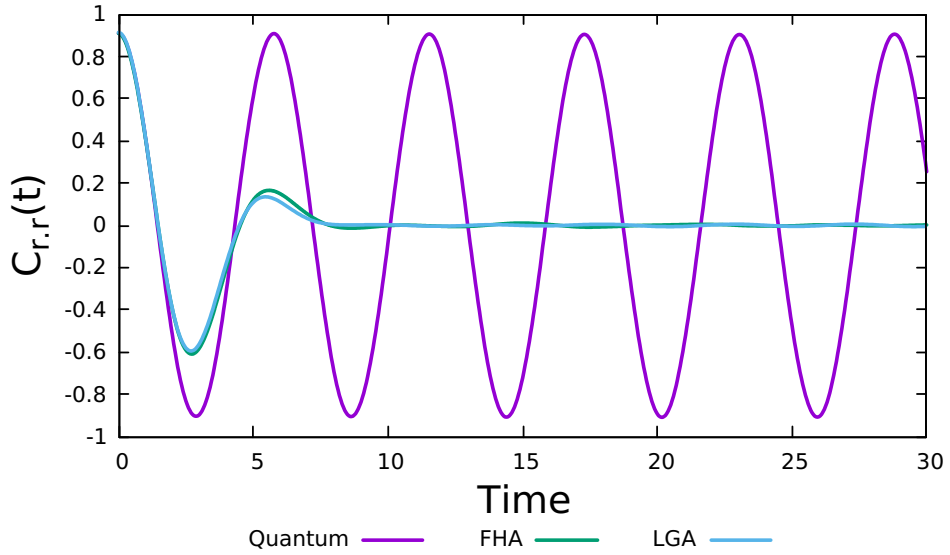

Figure 3.26: Position time correlation function for the two-dimensional strongly anharmonic oscillator at low temperature, $\beta = 8$. Quantum (purple), LGA (blue) and FHA (green).

3.3 Conclusions and Future work

We have developed a new locally harmonic approximation to LSC-IVR, the fitted harmonic approximation (FHA). The FHA method provides an alternative way to calculate the frequency used in the momentum distribution in a LGA-type calculation. We implement the FHA on toy one-dimensional systems for a range of temperatures. After verifying the method in the harmonic limit, we extend the method to mildly anharmonic, strongly anharmonic and Morse test systems. In contrast to the LGA, the frequencies obtained in the FHA are temperature dependent in addition to being system dependent. Furthermore, the method relies on numerically solving a nonlinear equation for ω which causes an increase in the computational time to run an FHA calculation.

We then extend the implementation of the method to two dimensions which also results in TCFs which agree closely with the LGA TCFs. Similarly to the LGA, the FHA requires the diagonalisation of a hessian matrix (γ instead of the potential). As the analytic form of the hessian elements are not known, in its current form, a two-dimensional spline needs to be used to interpolate between the values at grid points which increases the complexity of the FHA relative to the LGA.

At present, the implementation of the FHA is a proof of principle, showing a potential method which could be used as an approximation to LSC-IVR. For the test systems considered, the method gives TCFs which are comparable to and in some cases better than the LGA. Future work could involve trying to devise a practical implementation for the FHA and to investigate other ways in which the frequencies could be calculated and whether the LGA can be improved upon.

Chapter 4

Windowed Centroid Molecular Dynamics

Preliminary work by Althorpe,[106] showed that applying a constraint to the tangential spread of the ring-polymer via a RATTLE algorithm in CMD led to results which were comparable to QCMD for the champagne bottle Morse potential.[79] This preliminary finding was a promising result as constraining the quasi-centroid in QCMD increases the complexity of the dynamics in the simulation relative to CMD.[79; 84] The model used to test the method is the 2D champagne-bottle Morse potential which is a model for a rotating and vibrating O-H bond. The motivation then arises to further simplify this finding. i.e. can we replicate this finding without the need for constrained dynamics. To do this we apply a simple modification to the CMD, through the application of a window function as discussed in Sec. (4.2). We begin with a review of the background theory concerning CMD and QCMD before applying the window function to the champagne-bottle Morse potential as well as two angular dependent potentials constructed to mimic the bend like behaviour in water.

4.1 Background Theory

4.1.1 Centroid Molecular Dynamics (CMD)

The idea behind centroid molecular dynamics (CMD) [70; 71] is a conceptually simple one. As with most path-integral based methods, the starting point is the 'classical isomorphism' between the expression for the quantum partition function and that of the partition function of a classical ring polymer of N replicas of the system, with neighbouring replicas connected via temperature dependent harmonic

springs. In centroid molecular dynamics, the Cartesian centre of mass or the centroid of the ring polymer is constrained and the ring polymer is allowed to fluctuate about this centroid. By doing so, the potential of mean force due to these fluctuations can be calculated and one can simply carry out a classical dynamics simulation on this potential. The method has been extensively tested on a wide variety of systems,[68; 107] and due to the simplicity of the method, many of the usual techniques used in molecular dynamics simulations can also be used for CMD.

In this chapter we restrict our investigation to 2D as this is sufficient to capture the physics that we want to investigate. In CMD one considers the cartesian centroid, or the centre of mass of the ring polymer. In 2D, for a particle of mass m, represented by N beads, the centroid position $\mathbf{Q} \equiv (Q_x, Q_y)$ is defined as

$$\mathbf{Q} = \frac{1}{N}\sum_{i=1}^{N} \mathbf{q}_i \tag{4.1}$$

where $\mathbf{q}_i \equiv (q_{ix}, q_{iy})$ are the cartesian coordinates of the i-th ring-polymer bead. In the same way, the centroid momentum $\mathbf{P}$ is defined as

$$\mathbf{P} = \frac{1}{N}\sum_{i=1}^{N} \mathbf{p}_i \tag{4.2}$$

where $\mathbf{p}_i \equiv (p_{ix}, p_{iy})$ are the cartesian momenta of the i-th ring-polymer bead. The equations of motion for CMD are written as[78]

$$\dot{\mathbf{Q}} = \frac{\mathbf{P}}{m} \tag{4.3a}$$

$$\dot{\mathbf{P}} = -\frac{\partial F(\mathbf{Q})}{\partial \mathbf{Q}} \tag{4.3b}$$

where

$$F(\mathbf{Q}) = -\frac{1}{\beta}\ln Z_0(\mathbf{Q}) \tag{4.4}$$

is the free energy obtained from

$$Z_0(\mathbf{Q}) = \frac{1}{(2\pi\hbar)^{2N}} \int d\mathbf{q}' e^{-\beta W(\mathbf{q}')} \prod_{\nu=x,y} \delta(Q'_\nu - Q_\nu) \tag{4.5}$$

where d$\mathbf{q}$' indicates the integral takes place over all beads $\mathbf{q}_i$, we define

$$W(\mathbf{q}) = U(\mathbf{q}) + S(\mathbf{q}) \tag{4.6}$$

$$U(\mathbf{q}) = \frac{1}{N}\sum_{i=1}^{N} V(\mathbf{q}_i) \tag{4.7}$$

$$S(\mathbf{q}) = \frac{mN}{2(\beta\hbar)^2}\sum_{\nu=x,y}\sum_{i=1}^{N}(q_{\nu i+1} - q_{\nu i})^2 \tag{4.8}$$

Where $U(\mathbf{q})$ is the potential experienced by the ring-polymers and $S(\mathbf{q})$ the potential due to the springs connecting the system replicas in the ring polymer. Since $S(\mathbf{q})$ is independent of $\mathbf{Q}$, it follows that

$$-\frac{\partial F(\mathbf{Q})}{\partial \mathbf{Q}} = -\left\langle \frac{\partial \mathbf{U(q)}}{\partial \mathbf{Q}} \right\rangle_{\mathbf{Q}} \tag{4.9}$$

where

$$\langle ... \rangle_{\mathbf{Q}} = \frac{1}{Z_0(\mathbf{Q})}\int d\mathbf{q}' e^{-\beta W(\mathbf{q}')}(...)\prod_{\nu=x,y}\delta(Q'_\nu - Q_\nu) \tag{4.10}$$

4.1.2 Adiabatic Centroid Molecular Dynamics

To perform a CMD calculation one would need to sample the configuration space of all of the non-centroid modes of the ring polymer at all centroid positions. This becomes difficult beyond the simplest of systems and so a more practical approach involves the adiabatic decoupling of the physical motion of the centroid mode from the fictitious dynamics of the noncentroid modes.[82] This is achieved by artificially reducing the masses of the non-centroid modes by a factor of γ^2, thus accelerating the motion of the non centroid modes. The mass of the centroid is kept at the physical mass.

The scaling of the modes is given as

$$m_1 = m, \qquad m_n = \lambda_n m/\gamma^2 \tag{4.11}$$

Where m_1 is used to denote the centroid mass and m_n the mass of the non-centroid modes ($2 < n < N$). λ_n are determined by the normal mode transformation from bead coordinates to normal mode coordinate as described in ref.[82].

The idea is that the motion of the centroid is comparatively slow relative to the non centroid modes and so it can be thought that centroid is in a bath due to the non centroid modes. As a result, adiabatic centroid molecular dynamics (ACMD) computes the potential of mean force on the fly. The scaling factor of γ is often referred to as the adiabaticity parameter and needs to be chosen such that the centroid and noncentroid modes are decoupled. The drawback of this approach is

that the larger the parameter, the smaller the time step that needs to be used in the dynamics, and so the choice of the parameter is usually a trade off between numerical accuracy and computational effort.

4.1.3 Instantons

In the context of path-integrals, instantons arise when Feynman path-integral theory is used to describe quantum tunnelling through barriers. Instantons describe the dominant tunnelling path which gives an approximate but physically rigorous description of the tunnelling dynamics.[86] These instantons correspond to periodic orbits (of length $\beta\hbar$) on the inverted potential energy surface.[79; 86]

4.1.4 The Breakdown of CMD - Centroid Constrained Instantons

We consider the Champagne-bottle morse potential given by the form

$$V(r) = D_0(1 - e^{-\alpha(r-r_e)})^2 \tag{4.12}$$

where $r = \sqrt{x^2 + y^2}, D_0 = 0.18748,\ \alpha = 1.1605, r_e = 1.8324$ and $m = 1741$ a.u.

This potential is radially dependent but is angular independent, i.e. it is spherically symmetric. Using this potential the breakdown of CMD, reproduced at low temperatures has been investigated by Marx and Ivanov[83] and Trenins and Althorpe.[78] Fig. (4.1) reproduced from ref.[78], shows a plot of the potential of mean force, $-\partial F/\partial R_0$ vs R_0, where $R_0 = \sqrt{X_0^2 + Y_0^2}$ at temperatures 200-600 K. This has been overlayed with the CMD Boltzmann distribution. It is apparent from this figure that the force flattens below a radius R_0 which increases as the temperature decreases. Furthermore, it can be seen that at temperatures of 400 K and 600 K that the CMD Boltzmann distribution is well separated from this region. However, for the case of 200 K, it can be seen that there is an appreciable overlap of the CMD Boltzmann distribution and this flattened region.

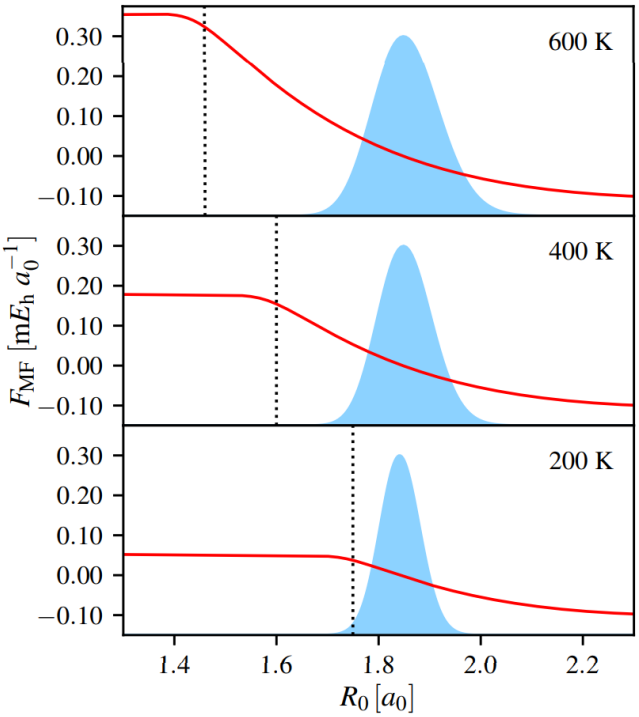

Figure 4.1: The CMD mean-field force $-dF(R_0)/dR_0$ (red), plotted on top of the corresponding Boltzmann distribution (blue). The dashed line indicates the position at which the curve begins to flatten. Figure reproduced from ref.[78].

The reason for the occurrence of this overlap can be explained using Fig.(4.2) reproduced from ref.[78]. The figure shows the centroid-constrained ring-polymer distributions at three points along a single trajectory for the 2D Morse oscillator describing an O-H bond at 400 and 200 K. The trajectory shown at 200 K is one of the 6% of trajectories which fall into the flat region at this temperature as previously described in Fig. (4.1). At 400 K the distribution remains relatively compact as a 'blob', with a slight stretching observed at the inner turning point where it pushes against the repulsive wall; the minimum energy ring polymer within the distribution is a point at the centroid. In contrast, at 200 K, the trajectory shows that the distribution spreads or smears out at the turning point where the minimum energy ring polymer has a delocalised geometry. This geometry is a minimum on the ring polymer surface, subject to a centroid constraint. The path followed by the beads corresponds to a periodic orbit on the inverted potential surface, subject to a time-averaged constraint. Thus, by constraining the centroid in the distribution, CMD artificially creates instantons.

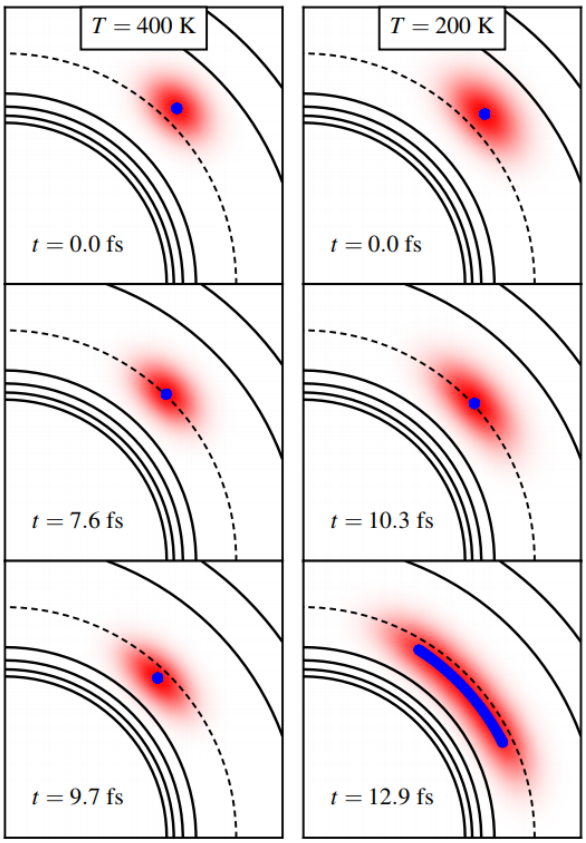

Figure 4.2: CMD trajectories on the Morse potential (black contour lines), r_e is shown by the dashed line. The centroid-constrained bead distribution is shown in red and the corresponding minimum-energy ring-polymer configuration in blue. The artificial instanton is seen in the 200 K trajectory at 12.9 fs.

4.1.5 Quasi-Centroid Molecular Dynamics

With quasi-centroid molecular dynamics,[79] instead of constraining the cartesian centroid as with CMD,[70] a constraint is applied to the centroid of the ring-polymer radial coordinates

$$R = \frac{1}{N}\sum_i r_i \tag{4.13}$$

where

$$r_i = \sqrt{x_i^2 + y_i^2} \tag{4.14}$$

Application of this constraint makes it impossible for the ring-polymers to lower their energy by spreading out and moving outwards into instantons. Furthermore this constraint also ensures that the R describes the centre of the ring-polymer distribution rather than its approximate focal point.

Defining a polar angle Θ which runs from 0 to 2π, we then define

$$\bar{Q}_x = R\cos\Theta \tag{4.15a}$$

$$\bar{Q}_y = R\sin\Theta \tag{4.15b}$$

such that they span the entire two-dimensional space. In the case of the 2D Morse potential, due to the circular symmetry of the potential, the dependence of the bead coordinate on θ does not need to be specified as the potential of mean force is independent of θ.

The non-linear relation between the centroid defined in both polar and Cartesian bead coordinates means that $\bar{\mathbf{Q}} \neq \mathbf{Q}$. However, it has been shown that in the high T limit that $\bar{\mathbf{Q}} \to \mathbf{Q}$, and that $\bar{\mathbf{Q}} \simeq \mathbf{Q}$ as long as the distribution is relatively compact.[79] As such $\bar{\mathbf{Q}}$ is referred to as the 'quasi-centroid'.

In quasi-centroid molecular dynamics, cartesian equations of motion are used which resemble those of CMD, with the difference being that mean field averages are taken around the quasi centroid rather than the cartesian centroid.

$$\dot{\bar{\mathbf{Q}}} = \frac{\bar{\mathbf{P}}}{m} \tag{4.16a}$$

$$\dot{\bar{\mathbf{P}}} = -\frac{\partial \bar{F}(\mathbf{R})}{\partial \bar{\mathbf{Q}}} \tag{4.16b}$$

where

$$\bar{F}(\mathbf{R}) = -\frac{1}{\beta}\ln\frac{\bar{Z}_0(\mathbf{R})}{R} \tag{4.17}$$

is the free energy obtained from

$$\bar{Z}_0(\mathbf{R}) = \int d\mathbf{q}' e^{-\beta W(\mathbf{q}')}\delta(R' - R) \tag{4.18}$$

Two approximations are made when writing out these equations. The first is that one can mean-field average the dynamics about the centroid and the second that the dynamics can be approximated by cartesian equations of motion.

The calculation of the force is further simplified by making the approximation that

$$-\frac{\partial \bar{F}(\mathbf{R})}{\partial \bar{\mathbf{Q}}} \simeq -\left\langle \frac{\partial \mathbf{U(q)}}{\partial \bar{\mathbf{Q}}} \right\rangle_{\mathbf{R}} \tag{4.19}$$

where

$$\langle ... \rangle_{\mathbf{R}} = \frac{1}{Z_0(\mathbf{R})}\int d\mathbf{q}' e^{-\beta W(\mathbf{q}')}(...)\delta(R' - R)\delta(\Theta' - \Theta) \tag{4.20}$$

This is equivalent to making the assumption that the terms of the force due to the ring-polymer springs do not survive when taking the mean field average. Although this assumption is exact for CMD, this is not the case for QCMD because R will contain components of ring-polymer normal modes orthogonal to the centroid. However, the size of the spring-force is expected to depend on the spread of the ring-polymer distribution and so will remain small as long as the ring-polymer distribution remains compact.

4.2 Windowed Centroid Molecular Dynamics

4.2.1 Theory and Implementation

The use of a radial constraint in quasi-centroid molecular dynamics rather than a cartesian centroid constraint has been shown to eliminate the artifactual red shift seen in the vibrational spectrum of the O-H unit.[79] At present, QCMD is the gold standard of path-integral based methods. However, the implementation of QCMD is significantly more complex and computationally more expensive than CMD. Also, at present it is not clear how readily QCMD can be generalised to molecules other than water. As a result, there is a need for a method which is able to cure the artifactual red-shift of CMD in spectra but is simpler to implement.

We therefore propose a new modification to the standard centroid molecular dynamics method, which we will show below gives results comparable to QCMD for the two-dimensional test systems considered. As described by Trenins and Althorpe, CMD breaks down due to the formation of artificial instantons. To overcome this issue, we apply a window function to the potential which acts as a filter. We measure the spread of the ring-polymer in the direction tangential to the centroid. The window function prevents the formation of ring-polymer geometries which are extremely delocalised, thus preventing the formation of artificial instantons (such as shown in Fig. (4.2)). This windowed centroid-molecular dynamics (WCMD) method differs from QCMD in an important way: QCMD regroups the ring-polymer geometries relative to a constraint based on the radius of the ring-polymer; i.e. the delocalised ring polymers remain, but are associated with large values of the radius. WCMD on the other hand acts as a filter and removes any delocalised ring-polymer geometries.

In 1-D the radius of gyration, ρ, of the ring polymer is defined as

$$\rho^2 = \frac{1}{N}\sum_{i=1}^{N}(x_i - X_0)^2 \tag{4.21}$$

where X_0 is the position of the cartesian centroid

$$X_0 = \frac{1}{N}\sum_{i=1}^{N} x_i \tag{4.22}$$

In 2D, the x and y components of the radius of gyration are analogous to the 1D case. Defining

$$R^2 = X_0^2 + Y_0^2, \qquad \tan\Theta = \frac{Y_0}{X_0} \tag{4.23}$$

We can write the tangential displacement of the i^{th} bead with respect to the position of the centroid (X_0, Y_0) as,

$$\begin{aligned} t_i &= (x_i - X_0)\sin\Theta - (y_i - Y_0)\cos\Theta \\ &= (x_i Y_0 - y_i X_0)/R \end{aligned} \tag{4.24}$$

The radius of gyration in the tangential direction is

$$\rho_t^2 = \frac{1}{NR^2}\sum_{i=1}^{N}(x_i Y_0 - y_i X_0)^2 \tag{4.25}$$

Thus we can measure the spread of the ring polymer using

$$s_t = R\rho_t \tag{4.26}$$

To apply the window to the ring polymer, an additional force $f(s_t)$ is added to the potential which acts on the fluctuations of the ring polymer in the direction tangential to its centroid. In the x direction, the force can be written as

$$\begin{aligned} F(x_i, y_i)_x &= -f'(s_t)\frac{\partial s_t}{\partial x_i} \\ &= \frac{-f'(s_t)}{N s_t}\left[Y_0(x_i Y_0 - y_i X_0) - \frac{1}{N}(x_j Y_0 - y_j X_0)y_j\right] \end{aligned} \tag{4.27}$$

and analogously for $F(x_i, y_i)_y$. Where we have defined

$$f(s_t) = \frac{r_s}{1 + \mathrm{e}^{(s_t - r_{1/2})/r_\sigma}} \tag{4.28}$$

and so

$$f'(s_t) = \frac{r_s \mathrm{e}^{(s_t - r_{1/2})/r_\sigma}}{r_\sigma(1 + \mathrm{e}^{(s_t - r_{1/2})/r_\sigma})^2} \tag{4.29}$$

Where r_s defines the height of the window function, r_σ defines how quickly $f(s_t)$ decays and $r_{1/2}$ is the half width of the function; this is an adjustable parameter within the method which we refer to as the window width and discuss in more detail in Sec.(4.2.2). In Eq.(4.27) the second term is independent of i and thus acts only on the centroid. Any additional force on the centroid would interfere with the dynamics, we only want the window function to apply a force on the fluctuations about the centroid in the tangential direction. To achieve this, the second term is subtracted in the calculation of the window function.

4.2.2 The Window Function

The window function $f(s_t)$ has an adjustable parameter $r_{1/2}$, the window half width. This parameter determines if a ring polymer of a certain spread is allowed by giving it an energy with negligible Boltzmann weight or if it is removed from the calculation. We can loosely define three regimes dependent on $f(s_t)$.

First, the limit that $f(s_t) = 0$ completely removes the fluctuations of the ring polymer in the direction tangential to the centroid. In other words, the ring polymer collapses onto a single bead in this direction; it is completely classical. The ring polymer is allowed to fluctuate as normal in the direction radial to the centroid. Thus a window width of zero can be thought of as a mixed quantum classical calculation.

The second is intermediate values of $f(s_t)$. In this regime most of the ring polymer geometries are kept within the calculation, however ring polymers which are extremely delocalised are filtered out from the calculation. In this work, this is the regime which we are concerned with.

Third, In the limit that the $f(s_t)$ becomes large, i.e. the radius of gyration of allowed polymers is increased. In this regime, the problematic delocalised ring polymers are again included in the calculation, i.e. the filter is gradually being removed and we return to a standard CMD calculation.

4.2.3 Spectral Damping Function

In the calculation of the spectra in this chapter, a damping function is applied to the TCF before Fourier transforming to calculate the spectra. This function has the form:

$$f(t) = \frac{1}{1 + e^{(|t|-t_{1/2})/\tau}} \tag{4.30}$$

with parameters $t_{1/2} = 400$ fs and $\tau = 25$ fs, chosen to model the decorrelation time in liquid water.[79]

4.2.4 Preliminary Tests

We begin by considering the champagne-bottle Morse potential discussed above in Eq.(4.12). We apply the window function to CMD and compare it with the preliminary work by Althorpe, in which the spread of the ring polymer was constrained via a RATTLE algorithm. We find that, by setting $r_{1/2} = 0.1$ we get almost identical results to the constrained CMD result (shown in Fig.(4.3)), and so we use this as the value for $r_{1/2}$ throughout. We use values of $r_\sigma = 0.03$ and $r_s = 1.6$ with the number of beads $N = 32$.

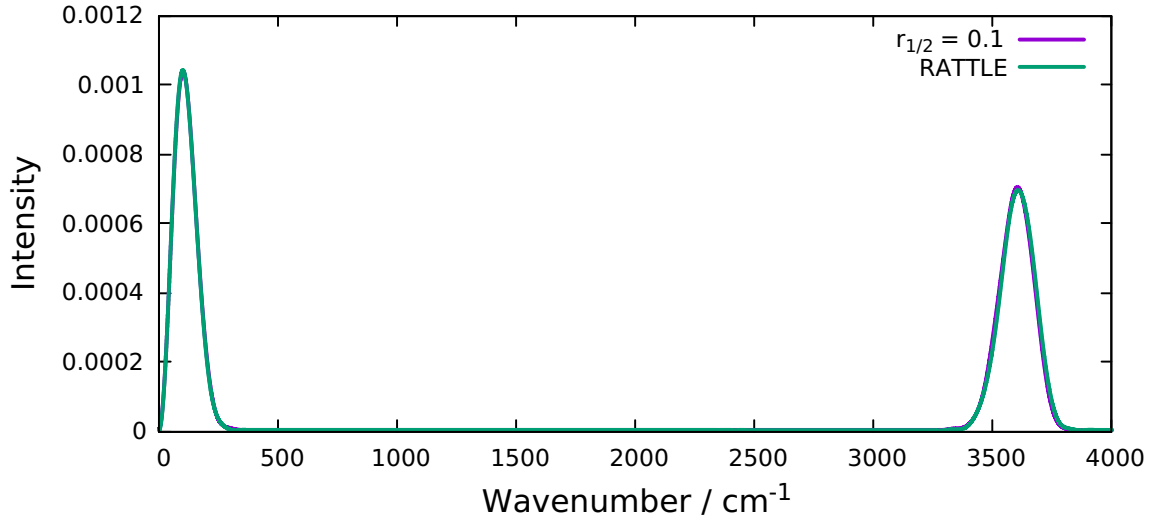

Figure 4.3: RATTLE constrained CMD (purple) spectrum and WCMD spectrum (green) with $r_{1/2} = 0.1$ for the champagne bottle Morse potential at 200K.

4.2.5 Insensitivity of Spectra Due to Window Width

We plot the spectra of the champagne-bottle Morse potential at 200K (Fig.(4.4)), whilst varying $r_{1/2}$. This shows that the spectrum obtained is insensitive (a small shift of $45cm^{-}1$ is seen in the peak maximum between $r_{1/2} = 0.1$ and $r_{1/2} = 0.5$) to the width of the window as expected. For $r_{1/2}$ between 0.1 and 0.5, the peak positions and intensities vary by only a very small amount. However, as we further increase or decrease the width of the window we see movement of the peak positions. In the limit that $r_{1/2} \to 0$, as discussed in Sec.(4.2.2) we have a regime in which the ring polymer is almost completely classical in its fluctuation in the direction tangential to the centroid but quantum in the direction radial to the centroid, this results in a peak which is red shifted. In the limit that the $r_{1/2}$ becomes very large, the window is no longer exerting any force on the fluctuations about the centroid. The spectrum will therefore tend towards the CMD result in this regime and we will

see a red shift due to delocalised ring polymers as seen with $r_{1/2} = 1.0$.

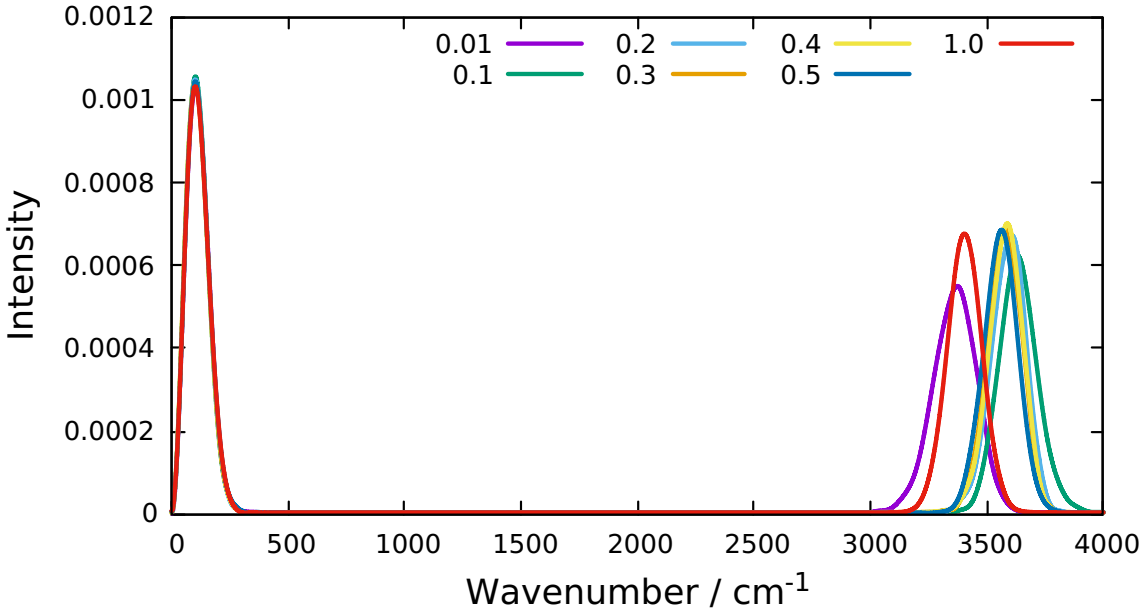

Figure 4.4: WCMD spectrum for the champagne bottle Morse potential at 200K for different $r_{1/2}$.

4.2.6 Adiabatic Implementation

Using the prescription for the adiabatic implementation of centroid molecular dynamics discussed in Sec.(4.1.2) we implement an adiabatic version of WCMD which is referred to as AWCMD. Convergence of the spectra at 200 K with respect to the adiabaticity paramter γ is shown in Fig. (4.5). At $\gamma = 16$, the peaks positions have converged, but some slight wiggles remain, at $\gamma = 32$ these issues have been resolved and we achieve spectral convergence. Fig.(4.6) shows that the AWCMD result with $\gamma = 32$ agrees graphically with the standard implementation of WCMD. As the Morse potential is radially symmetric, the PMF only needs to be calculated in 1D and so the standard implementation of WCMD at grid points is feasible. As the number of dimensions is increased the scaling of the standard implementation becomes prohibitively expensive. Therefore, it becomes advantageous to calculate the forces on the fly to reduce this computational cost. The adiabatic implementation will become more important in Sec. (4.2.9) where we consider angular dependent potentials.

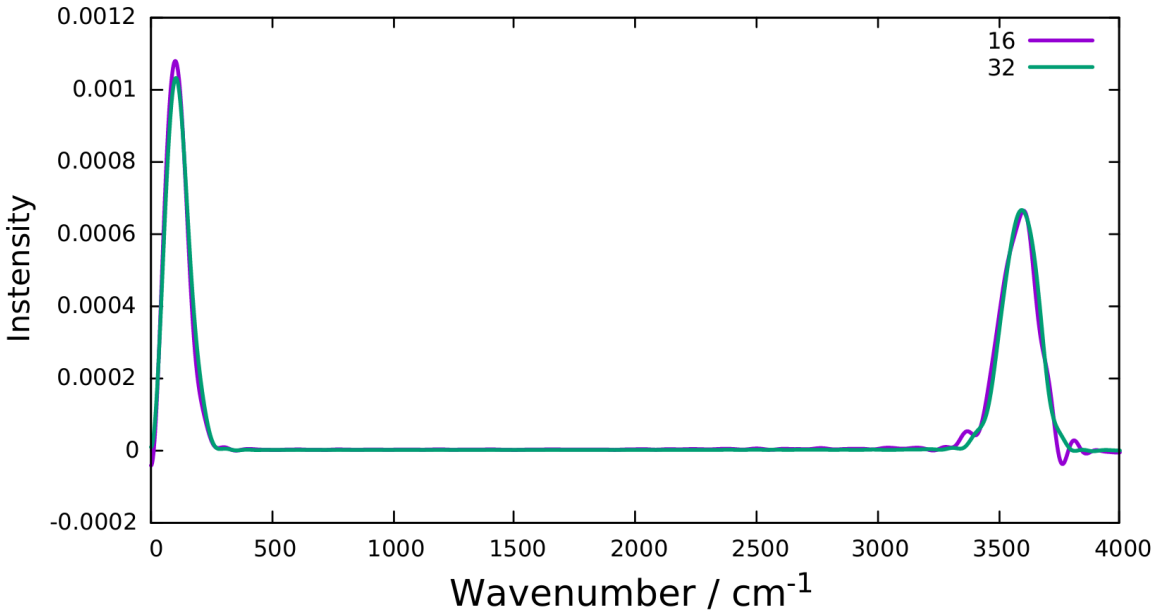

Figure 4.5: Spectrum for the champagne bottle Morse potential at 200 K for WCMD at 200K for $\gamma = 16$ (purple) and 32 (green).

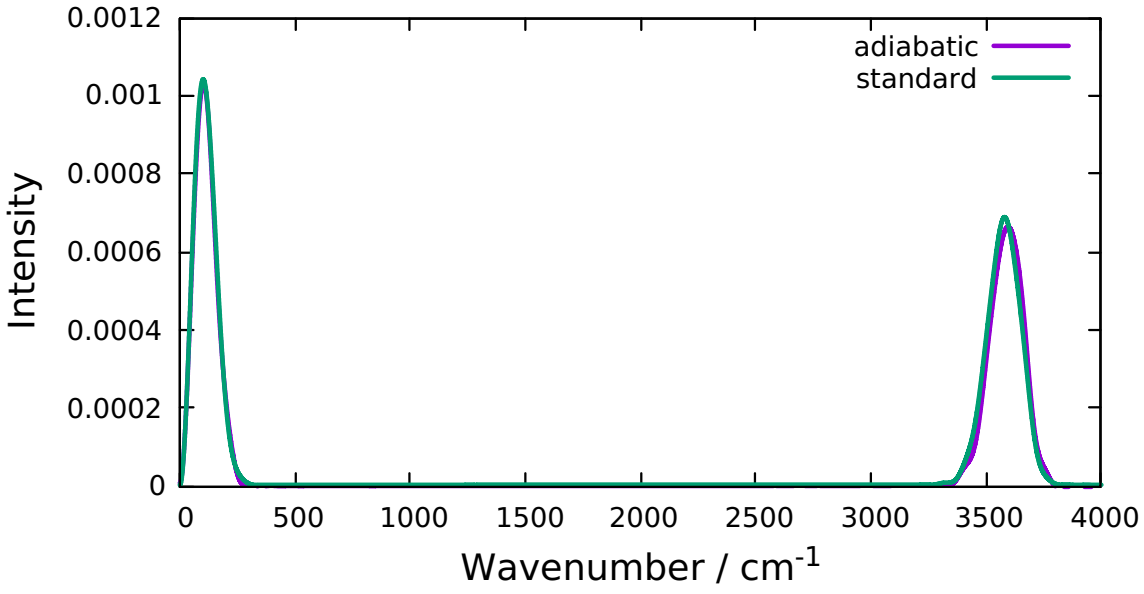

Figure 4.6: WCMD Spectrum for the champagne bottle Morse potential at 200K using the standard implementation (green) and the adiabatic implementation (purple) with $\gamma = 32$.

4.2.7 Comparison of Spectra

We compare the spectra obtained for the Champagne-bottle Morse potential at temperatures between 200 and 800 K for (CMD Fig.(4.7)), WCMD (Fig.(4.8)) QCMD (Fig.(4.19)) and Quantum (Fig.(4.10)). The quantum results are calculated on an equally spaced DVR grid as descried in [Appendix A.1]. The Quantum spectra display two peaks, one at low frequency (200 cm^{-1}) due to the rotation of the O-H bond and one at high frequency (3700 cm^{-1}) due to the vibration of the O-H bond. There are two main patterns which are observed: first, as the temperature is increased the frequency of the rotation also increases. Second, the frequency of the vibrational peak is temperature independent, i.e. the peak position is unaltered by increasing temperature. CMD correctly predicts the position and intensities of the rotational peak, however, the method breaks down as expected for the vibrational peak. As the temperature is decreased from 800 to 400 K, a red shift is seen in the position of the peak which becomes more strongly pronounced as the temperature is further decreased to 200 K. QCMD and WCMD overcome this problem of the red shift in the vibrational peak and correctly predict a temperature independence of the peak. The results for both methods show very good agreement with each other. QCMD corrects the spectral red shift by using a radial constraint rather than a cartesian contraint as discussed in Sec. (4.1.5). WCMD on the other hand applies a window function to prevent the formation of the delocalised ring polymers which cause the red shift. There is a small shift of 20 cm^{-1} between the quantum result and the QCMD[108] and WCMD result, however this is believed to be due to real-time coherence effects which are not captured by these methods based on Quantum statistics and classical dynamics.[78]

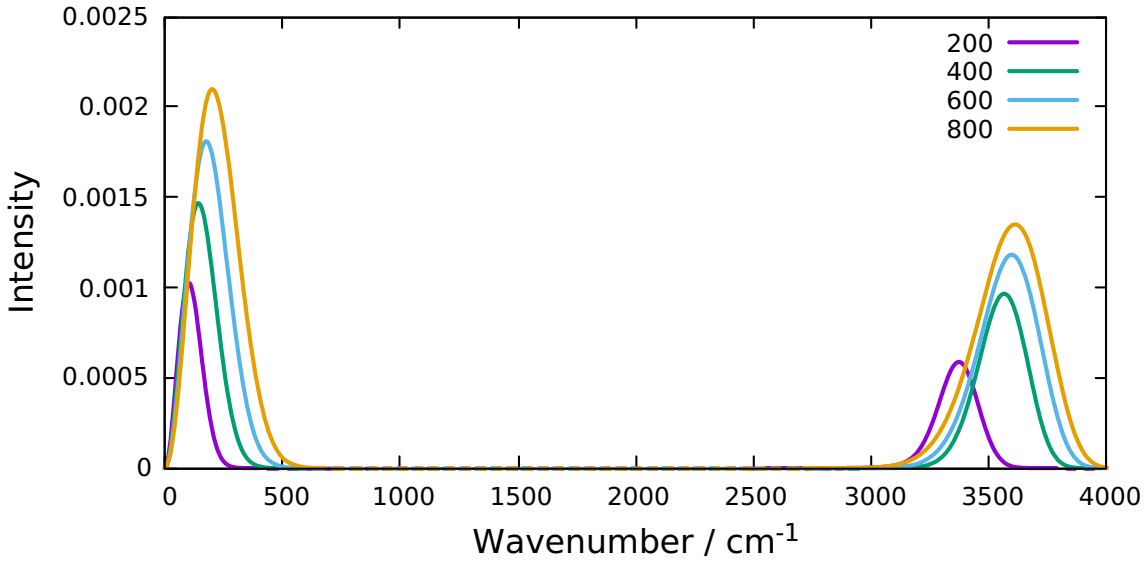

Figure 4.7: CMD spectra for the Morse potential at 200 (purple), 400 (green), 600 (blue) and 800 K (yellow).

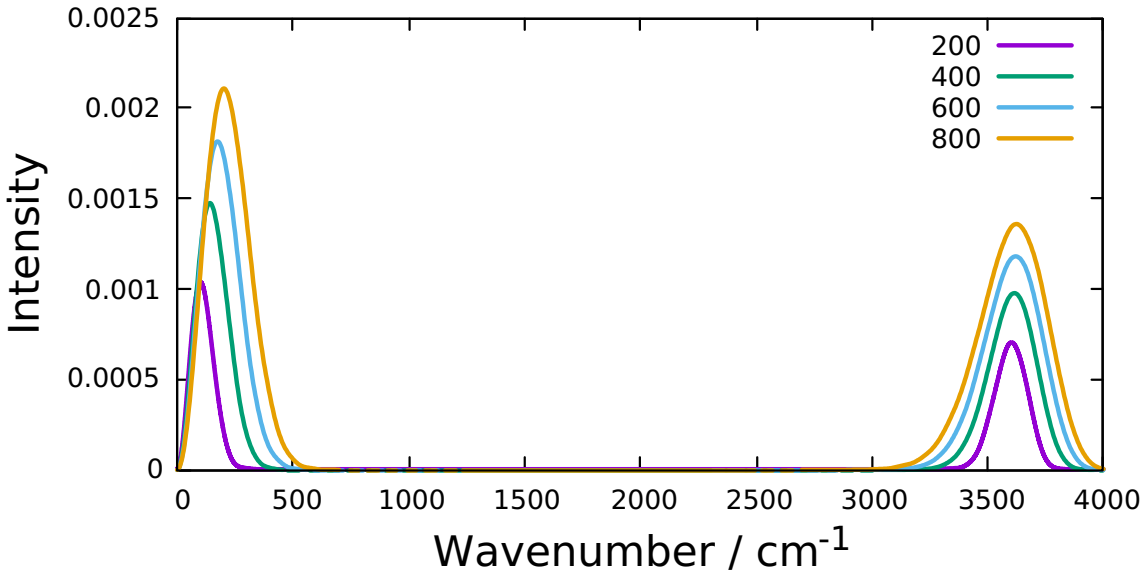

Figure 4.8: WCMD Spectra for the Morse potential at 200 (purple), 400 (green), 600 (blue) and 800 K (yellow).

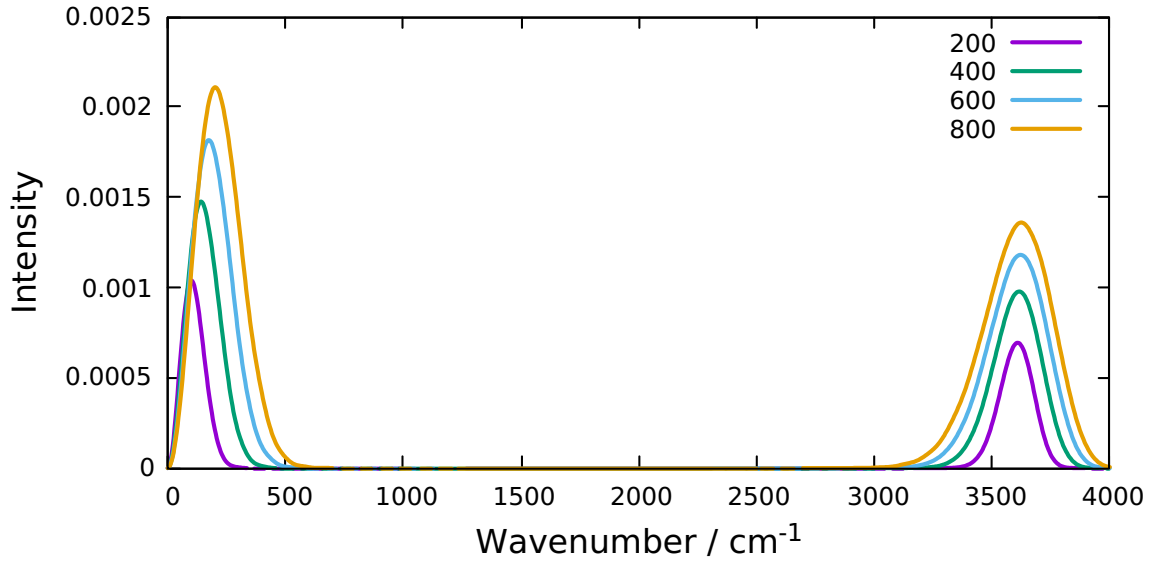

Figure 4.9: QCMD Spectra for the Morse potential at 200 (purple), 400 (green), 600 (blue) and 800 K (yellow).

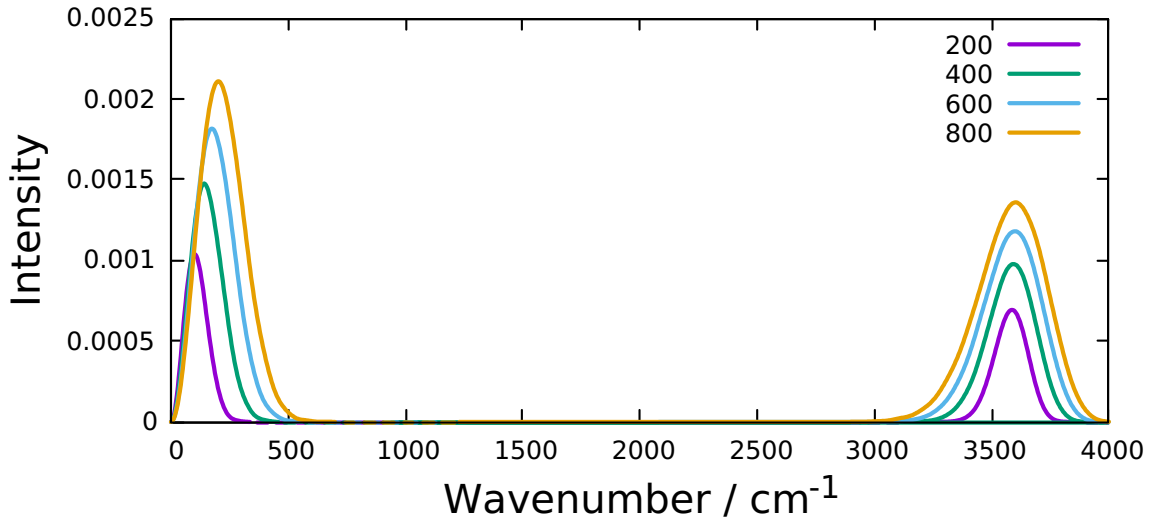

Figure 4.10: Quantum Spectra for the Morse potential at 200 (purple), 400 (green), 600 (blue) and 800 K (yellow).

4.2.8 Potential of Mean Force

To investigate the reason for the difference between the spectra for CMD and WCMD, we plot the potential of mean force vs R_0 as done in Fig.(4.1) at 600 K (Fig.(4.11)), 400 K (Fig.(4.12)) and 200 K (Fig.(4.13)). Comparing the PMF plots for 600 K (Fig.(4.11)), the curves for CMD and WCMD agree very well for the most part, this is to be expected as CMD does very well at high temperatures. As R_0 falls below 1.5 the CMD curve begins to flatten whereas the WCMD curve continues to rise. As the CMD Boltzmann distribution does not have a significant overlap in this region, the formation of artificial instantons does not become problematic at this temperature and so a red shift is not observed in the spectrum. At 400K (Fig.(4.12)), the CMD spectrum shows a slight red shift in the spectrum. Fig.(4.1) shows that below 1.6 that the CMD curve begins to flatten out, since a larger proportion of the CMD boltzmann distribution falls under this area, the formation of delocalised instantons starts to become more significant. Application of the window function prevents the formation of these delocalised ring-polymer geometries and thus prevents the curve from flattening out. At 200 K (Fig(4.13)) we see a similar result to that seen at 400 K, however since the value of R_0 at which the curve begins to flatten out is larger ~ 1.8, the red shift observed in the spectra is more pronounced relative to 400 K. At 200 K it is known that CMD breaks down, again the window function prevents the formation of these delocalised ring-polymer geometries which prevents the flattening out of the PMF which eliminates the red shift in the spectra. Promisingly, plots of the QCMD PMF data[109] shows excellent agreement with the result obtained from WCMD.

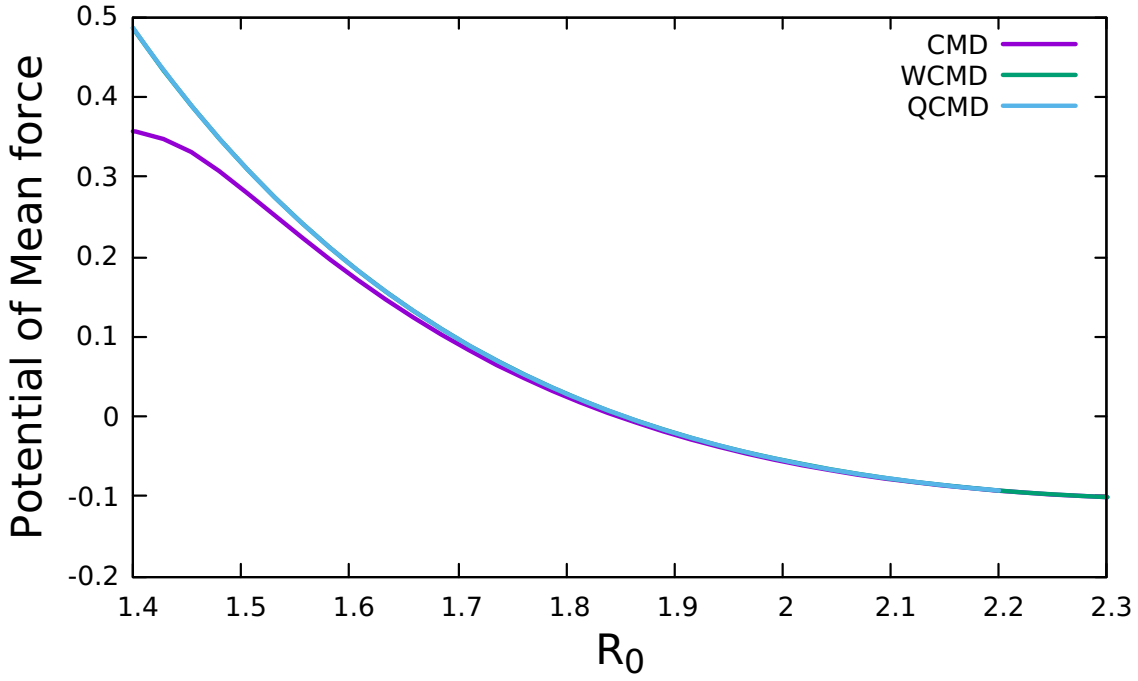

Figure 4.11: Plots of the PMF as a function of coordinate taking along the radial direction of the potential at 600 K. CMD (purple), WCMD (green) and QCMD (blue)

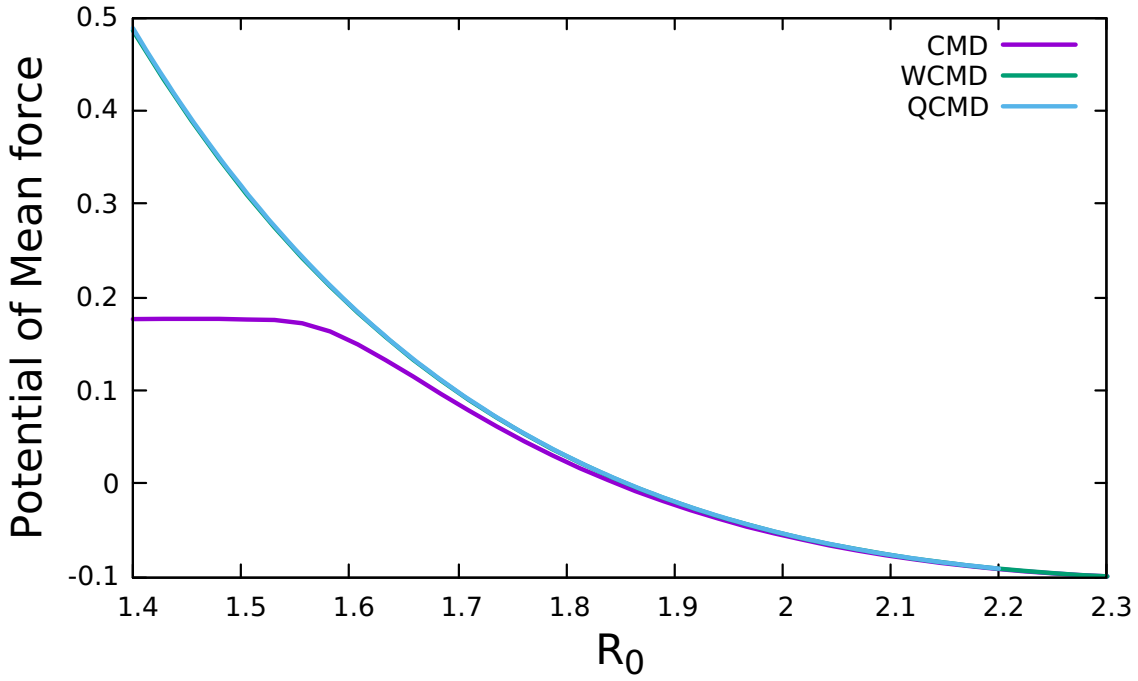

Figure 4.12: Plots of the PMF as a function of coordinate taking along the radial direction of the potential at 400 K. CMD (purple), WCMD (green) and QCMD (blue)

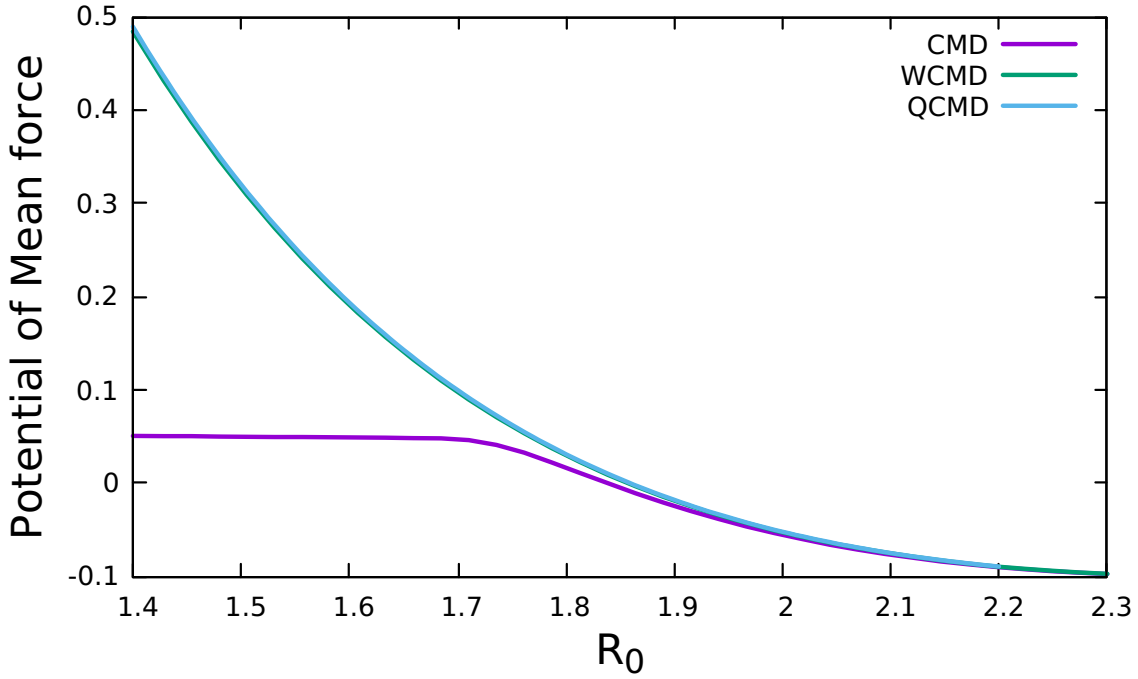

Figure 4.13: Plots of the PMF as a function of coordinate taking along the radial direction of the potential at 200 K. CMD (purple), WCMD (green) and QCMD (blue)

4.2.9 Angular-Dependent Potentials

To further test the validity of WCMD, we construct two test potentials which contain an angular dependence and compare the spectra obtained to the classical, CMD and exact quantum results. The motivation for this is to see if WCMD can also be extended to describe the bend-like behaviour seen in molecular systems. We test two regimes within the angular dependent potentials. The first of the potentials is based on the Champagne Morse potential with an additional harmonic angular term. The second is also of this type but with an additional strongly anharmonic term in the angular component which would more realistically mimic the bend like behaviour in water than the first. We utilise the adiabatic implementation of WCMD in the calculation of these spectra (AWCMD) with a adiabaticity parameter of $\gamma = 32$.

Test Potential 1

The mathematical form of the first angular potential is given below

$$V(r,\theta) = D_0(1 - e^{-\alpha(r-r_e)})^2 + \frac{k_{\theta_1}}{2}(r\theta)^2 \tag{4.31}$$

where $r = \sqrt{x^2+y^2}, \theta = \arctan(y/x), D_0 = 0.18748, \alpha = 1.1605, r_e = 1.8324$ and $k_{\theta_1} = 0.02$. This is plotted below in Fig.(4.14)

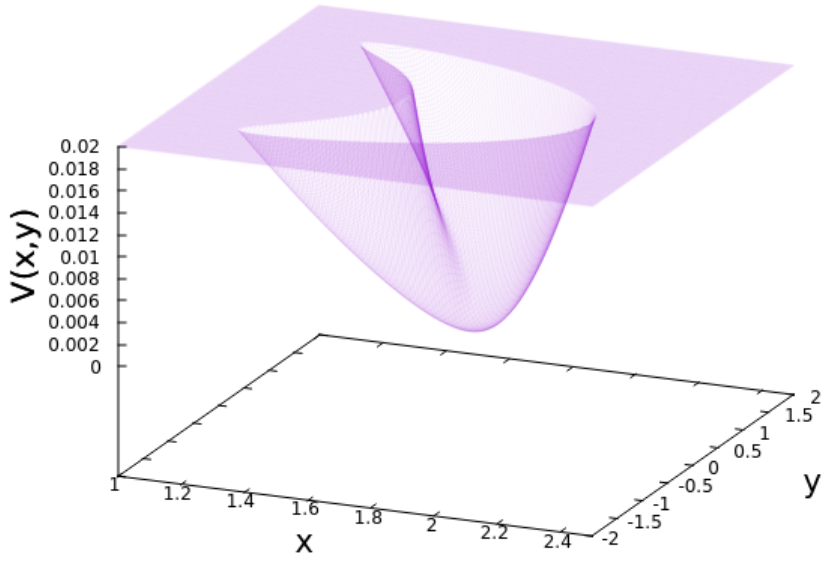

Figure 4.14: Plot of the first angular test potential given by Eq.(4.31).

We calculate the spectra for this potential using classical dynamics (Fig.(4.15)), CMD (Fig.(4.16)), WCMD (Fig.(4.17)) and the exact quantum result (Fig.(4.18)). The results tell a similar story to that of the Morse potential, i.e. a red shift is observed for the high frequency peak for CMD which is corrected by WCMD. The quantum mechanical result shows that the peak positions for both the low (750 cm^{-1}) and high frequency peaks (3600 cm^{-1}) are temperature independent. The classical result is able to replicate this temperature independence but incorrectly predicts the position of the high frequency peak (3750 cm^{-1}) which is due to the incorrect statistics for classical mechanics. The CMD result at high temperature is able to fix this problem with peak positions, however as with the 2D champagne-bottle Morse potential, as the temperature is decreased the formation of artificial instantons result in a red shift in the peak position. Promisingly, the WCMD result is able to significantly reduce the red shift seen in the peak position when compared to the CMD result (for example the shift is reduced from 122 cm^{-1} to 19 cm^{-1} at 200 K when compared to the quantum result (see table (4.1)).

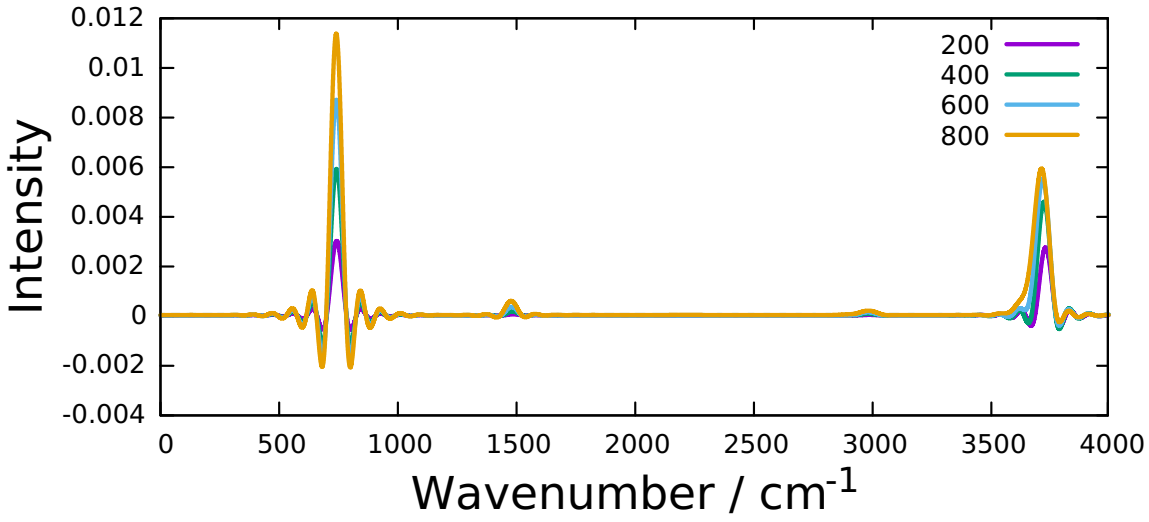

Figure 4.15: Classical spectra for the harmonic angular test potential at 200 (purple), 400 (green), 600 (blue), 800 K (yellow).

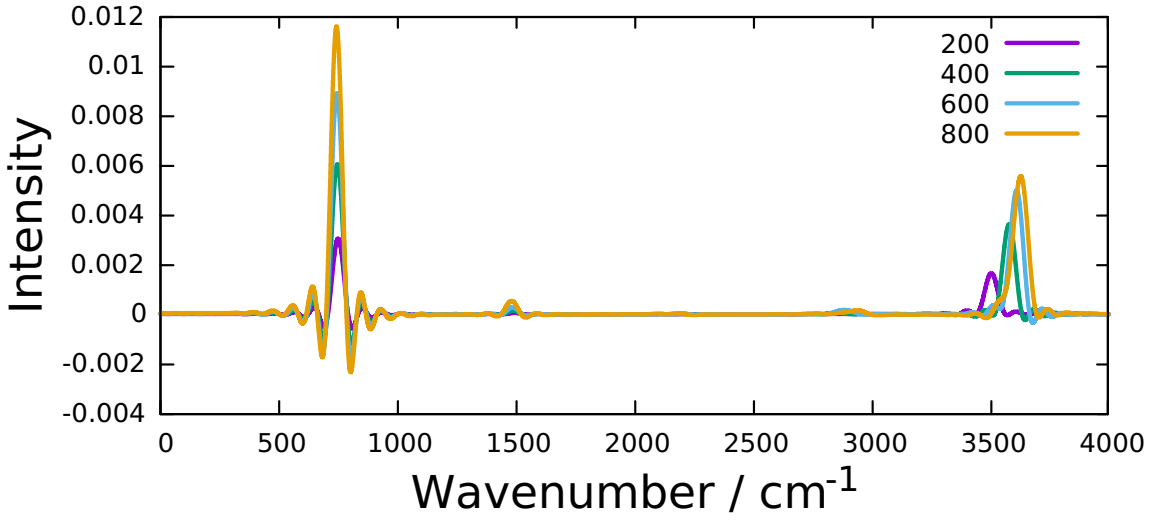

Figure 4.16: CMD spectra for the harmonic angular test potential at 200 (purple), 400 (green), 600 (blue), and 800 K (yellow).

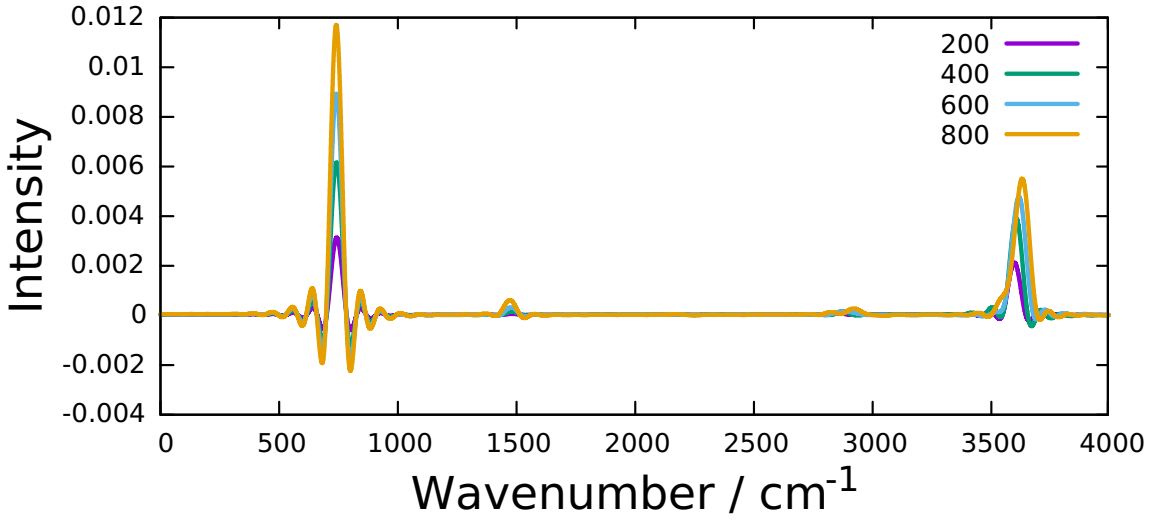

Figure 4.17: WCMD spectra for the harmonic angular test potential at 200 (purple), 400 (green), 600 (blue) and 800 K (yellow).

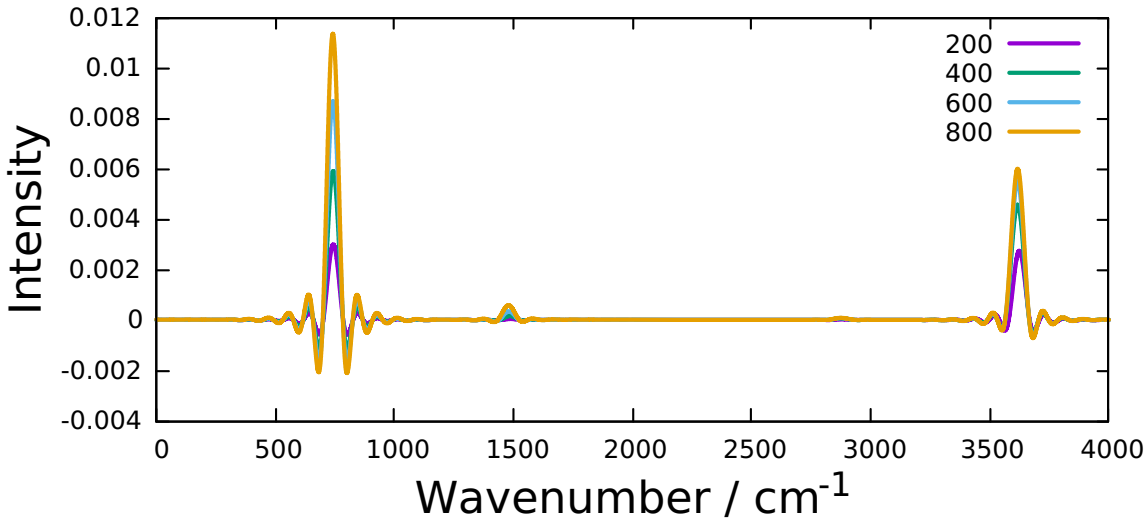

Figure 4.18: Quantum spectra for the harmonic angular test potential at 200 (purple), 400(green), 600 (blue) and 800 K (yellow).

T/K	Classical	CMD	WCMD	Quantum
200	3734	3502	3605	3624
400	3726	3582	3610	3618
600	3722	3616	3620	3618
800	3718	3630	3634	3617

Table 4.1: Position of the maximum of the high frequency peak in wavenumbers (cm^{-1}) for the first angular test potential.

Test Potential 2

The form of the second angular potential which has been constructed to mimic a bend like movement in water is given below:

$$V(r,\theta) = D_0(1 - e^{-\alpha(r-r_e)})^2 + \frac{k_{\theta_2}}{2}(r\theta)^2 + \frac{k_{\theta_2}}{40}(r\theta)^4 \tag{4.32}$$

where $r = \sqrt{x^2+y^2}, \theta = \arctan(y/x), D_0 = 0.18748, \alpha = 1.1605, r_e = 1.8324$ and $k_{\theta_2} = 0.08$

The potential is plotted in Fig.(4.19).

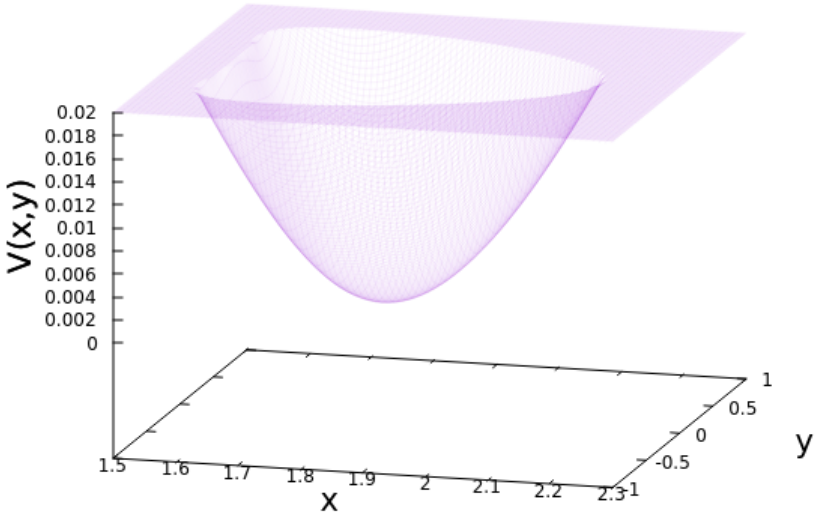

Figure 4.19: Plot of the second angular test potential given by Eq.(4.32) plotted against coordinate x and y.

In addition to being angular dependent, it can be see that the potential is narrower and less circular relative to the first angular test potential. We calculate the spectra for this potential using classical dynamics (Fig.(4.20)), CMD (Fig.(4.21)), WCMD (Fig.(4.22)) and the exact quantum result (Fig.(4.23)). For this potential, when considering the position of the peak maximum the quantum result shows that the position of both the low frequency and high frequency peaks are temperature independent (within 2 cm^{-1} for the high frequency peak, see table (4.2)). The classical result, shows a similar pattern (a temperature dependence of 9 cm^{-1} for the high frequency peak, see table (4.2)) but the frequency of the high frequency peak is incorrectly predicted. The CMD result improves upon the classical result at high

temperatures but the red shift is seen as the temperature is lowered from 800 to 200 K. WCMD again improves upon the CMD result by preventing the contribution of delocalised ring polymers seen in CMD from contributing to the potential of mean force (for example at 200K the red shift is reduced from 42 cm^{-1} to 12 cm^{-1}). For this potential we see an interesting result (Fig.(4.24)) for the low frequency peak. We observe a small blue shift in the CMD result which we discuss further in the next section. Interestingly, WCMD is able to fix this the blue shift in the low frequency CMD peak by the addition of the window function

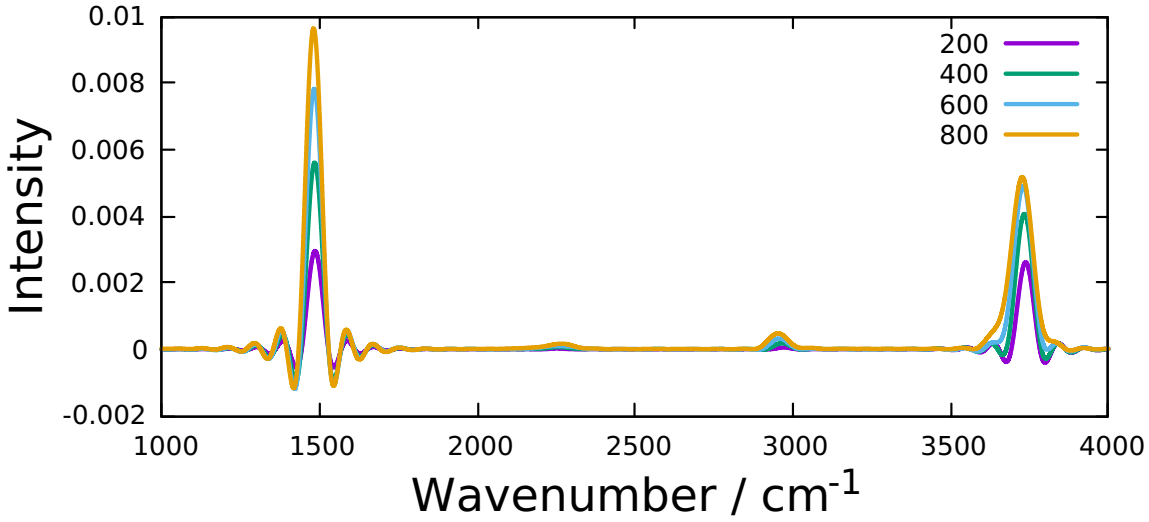

Figure 4.20: Classical spectra for the second angular test potential at 200 (purple), 400 (green), 600 (blue) and 800 K (yellow).

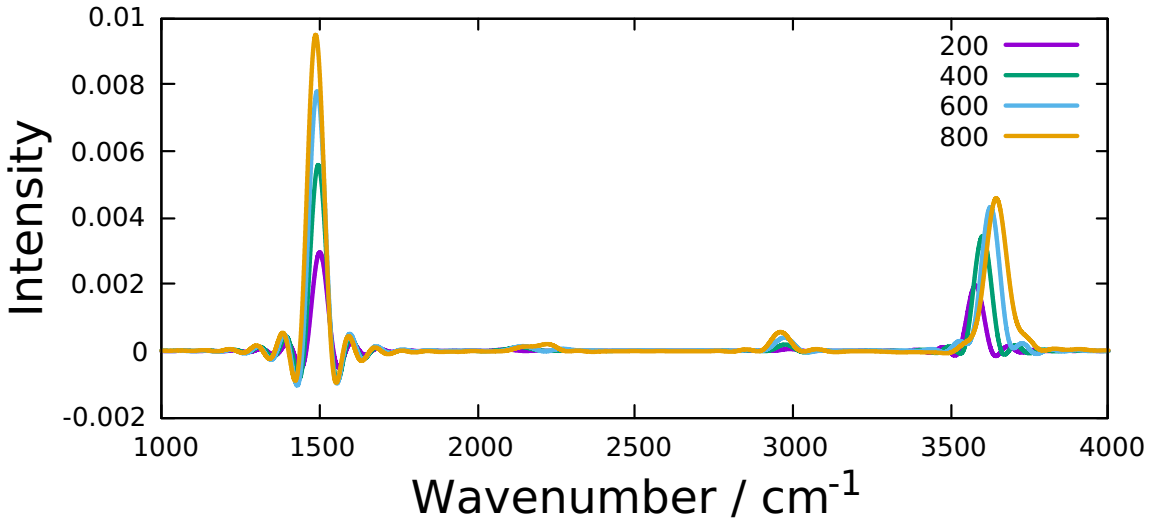

Figure 4.21: CMD spectra for the second angular test potential at 200 (purple), 400 (green), 600 (blue) and 800 K(yellow).

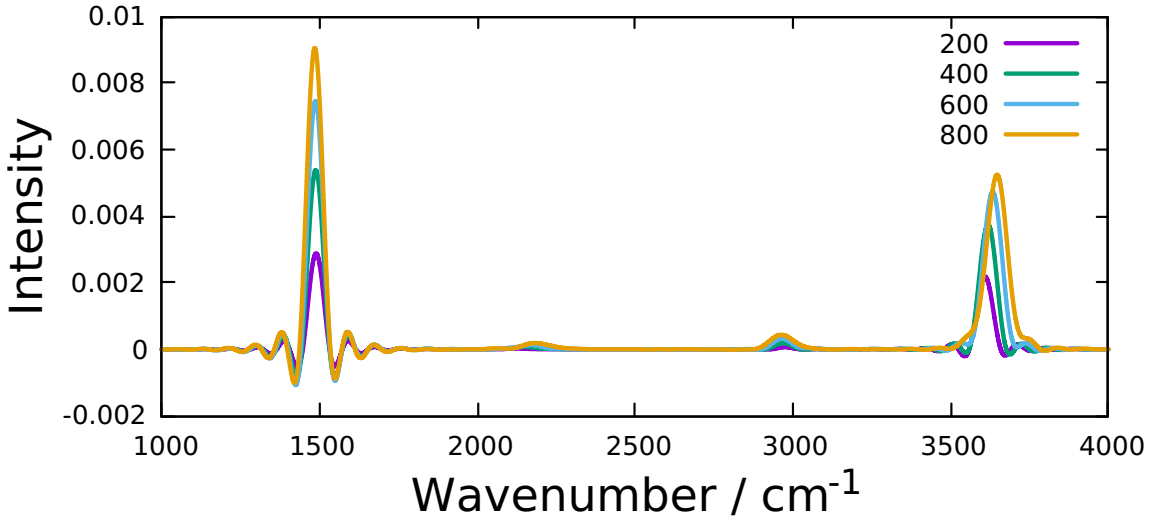

Figure 4.22: WCMD spectra for the second angular test potential at 200 (purple), 400 (green), 600 (blue), 800 K (yellow).

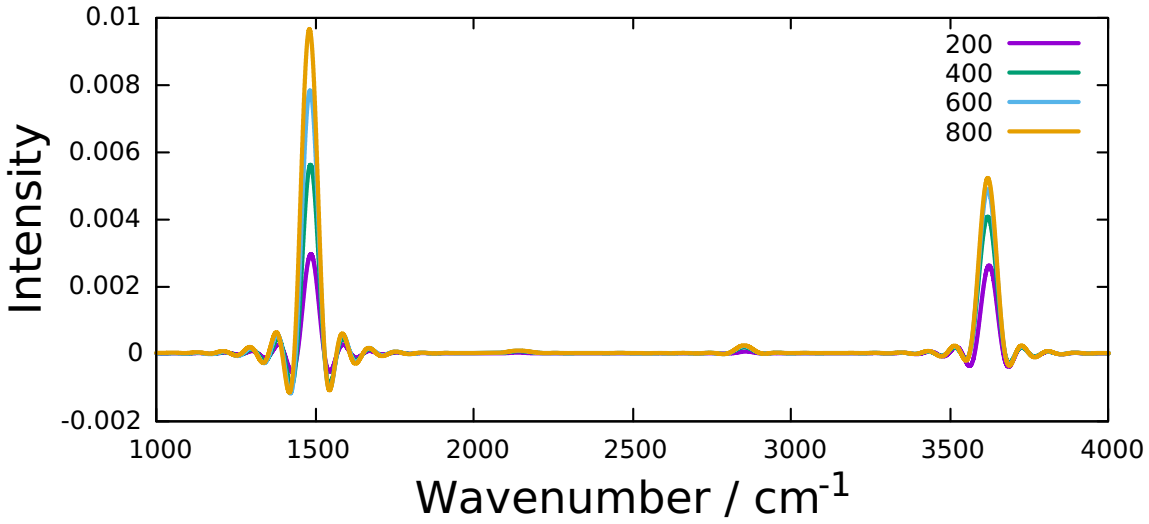

Figure 4.23: Quantum spectra for the second angular test potential at 200 (purple), 400 (green), 600 (blue) and 800 K (yellow).

T/K	Classical	CMD	WCMD	Quantum
200	3737	3579	3610	3622
400	3734	3601	3620	3620
600	3730	3625	3634	3620
800	3728	3646	3647	3620

Table 4.2: Position of the maximum of the high frequency peak in wavenumbers (cm^{-1}) for the second angular test potential.

Blue Shift in the Low Frequency Peak

As previously mentioned, a blue shift of approximately 15 cm^{-1} is observed in the lower frequency peak between CMD and the classical result (Fig. (4.24) and (4.25)). This phenomenon of a blue shift in the CMD spectral peak has not previously been reported and we believe that it is due to a vibration-rotation coupling effect due to this potential. The potential is r and θ dependent and so it is likely that the application of a centroid constraint results in the formation of ring-polymers which spread out into delocalised polymers along this potential surface in such a way that they lower their energies. These delocalised polymers manifest themselves as a blueshift in the low frequency peak. The application of the window function filters out these ring polymers and removes this blue shift.

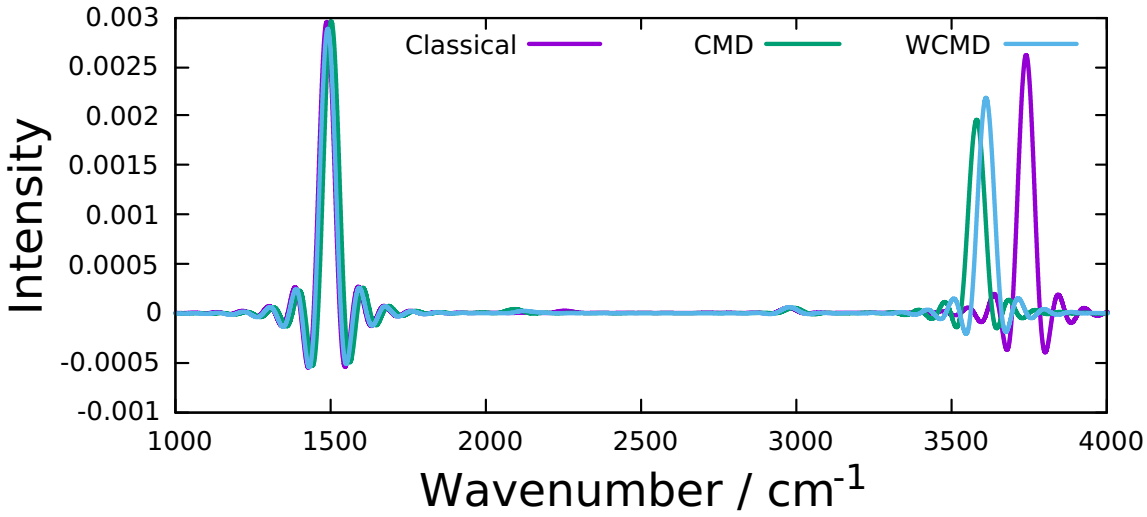

Figure 4.24: Plot of the spectra for the second angular test potential at 200 K. Classical (purple), CMD (green) and WCMD (blue).

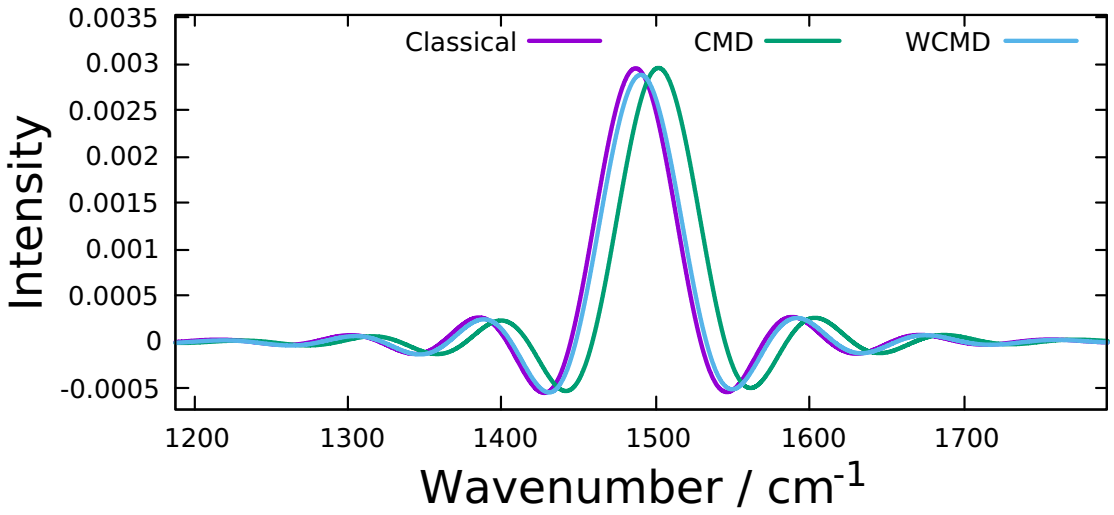

Figure 4.25: Enhanced plot of the low frequency peak for the second angular test potential depicting the blue shift in the CMD result (green) when compared to the classical (purple) and WCMD (blue) result.

4.3 Conclusions and Future work

We have proposed a new method, windowed centroid molecular dynamics (WCMD). This modification to CMD through the application of a window function prevents extremely delocalised ring polymers from contributing to the calculation of the potential of mean force. This method has been tested on two-dimensional systems, both radially symmetric and angular-dependent over a range of temperatures between 200 K and 800 K.

In the high temperature limit, the WCMD result tends towards the CMD result. This is not a surprise as the artificial instantons which cause the spectral red shift for the vibrational peaks in the spectrum of the two-dimensional champagne-bottle Morse potential are not problematic in this regime. In the low temperature limit, the CMD breakdown is avoided, i.e. the method prevents the formation of artificial instantons due to the centroid constraint which is shown in spectra by the elimination of the red shift exhibited in the vibrational peak.

In the case of angular dependent potentials, we see that for the high frequency peak, CMD again displays a red shift in the peak position at low temperatures. This again is improved by the addition of the window function. Furthermore in the second angular test potential mimicking the bend-like behaviour in water, we see a slight blue shift in the low frequency peak for the CMD result. This is an interesting result, which to the best of our knowledge, has not been reported before. This again is due to the centroid constraint in CMD causing ring polymers to delocalise along the potential surface in such a way that they lower their energy. The window function is able to filter out these ring polymers and correctly calculates the spectral peak position.

The WCMD method has shown to be very promising for the two dimensional systems tested, namely the rotationally symmetric Morse potential and the angular dependent potentials. For the Morse potential the method is able to replicate QCMD results, but has the advantage that it is conceptually simpler in addition to being algorithmically much easier to implement. The method also does well for angular dependent potentials and reduces the artefactual red shift due to CMD (e.g. from 42 cm^{-1} to 12cm^{-1} for the second angular potential at 200 K).

Future work in the development of this method therefore is likely to be focused on the extension and implementation of the method to larger more realistic systems such as gas phase water, this is likely to focus on the implementation of the window function to more generalised coordinates. This would demonstrate if WCMD is able to compete with QCMD as a practical and simple method for combining quantum statistics and classical dynamics.

Chapter 5

Conclusions and Future Work

In this thesis we have looked at three different approaches for approximating quantum time-correlations functions. The first of these approaches is constant uncertainty molecular dynamics (CUMD).[85] CUMD is conceptually interesting and the results obtained for the toy systems in the original publications were promising. In Chapter 2 we found that, although CUMD is presented as simple and efficient, the application of a non-holonomic constraint requires an ad hoc fix to the algorithm which results in the method being extremely sensitive to a Lagrange multiplier. Furthermore the dynamics do not conserve the energy and require extremely small time steps to prevent individual trajectories from becoming numerically unstable. The application of the constraint thus makes the method impractical when applied to more realistic systems. To get around this problem we tried modifying CUMD by employing just the initial step of the method in which the momenta of the initial bead distribution are recalculated, then allowing the distribution to evolve classically. This modification gives reasonable results in the calculation of position autocorrelation functions in the toy systems considered, but when applied to a more realistic two-dimensional system we find that although the method correctly predicts the positions of peaks in the vibrational spectrum, it overpredicts the absorption intensities by two orders of magnitude. As a result, neither the original nor the modified version of CUMD can be extended to treat systems more realistic than the simplest toy models.

The second approach tested is the Fitted Harmonic approximation (FHA), a new locally harmonic approximation to LSC-IVR proposed in this work. We first tested this approach on 1D toy systems and found that it yields time correlation functions which are very close to the results of the LGA approximation to LSC-IVR of Liu and Miller.[32] On extending the methodology to two dimensions we found that the implementation of the method becomes significantly more difficult but again gives

results which are comparable to the LGA over a wide range of temperatures. The current implementation of the FHA is a proof of principle and is not practical and so is limited to the test systems considered. However, we find that the FHA TCFs are as good as if not better than the LGA TCFs. The FHA and LGA frequencies are different, and so in future work it may be of potential interest to further investigate and perhaps to develop alternate ways in which the frequency can be chosen in the LGA and whether this can improve the result. At present the choice of using the local second derivative for the frequencies in the LGA is made due to its simplicity; a more detailed investigation into this choice may provide more insight into improving the method.

Thirdly, we have developed a new method, windowed centroid molecular dynamics (WCMD) which modifies centroid molecular dynamics (CMD) by the application of a window function. The motivation behind this is the artificial red shift in the O-H spectral peak of water predicted by CMD. This breakdown of CMD was understood to be due to the centroid constraint used which results in the formation of extremely delocalised ring polymers. The QCMD method of ref.[79] was developed to overcome this issue by using a radial quasi-centroid constraint rather than the cartesian constraint, but QCMD is significantly more difficult to implement and algorithmically more challenging than CMD. In WCMD, we apply a window function which is a function of the spread of the ring polymer in the direction tangential to the centroid radial coordinate. Tests on the champagne-bottle Morse potential modelling the stretch of an O-H unit show that the window function is able to remove contributions of delocalised ring polymers in the CMD distribution which cause the red shift in spectral peaks over a wide range of temperatures. We have also tested the method on angular-dependent potentials which have been constructed to mimic the bend like behaviour in water; surprisingly we find that CMD results in a blue shift for the low frequency peak when compared to the classical result, but WCMD is again able to correct this artifact. The WCMD method is a very simple fix to CMD and thus likely to be practical. In future work, it will be interesting to implement WCMD on larger more realistic systems such as gas phase and liquid water to see if the method can be scaled up and become more efficient than QCMD—the current gold standard of path integral based methods.

Appendix A

Methodological Details

A.1 Exact Quantum Calculations

The exact quantum mechanical results generated in this thesis were calculated using the discrete variable representation (DVR) of Colbert and Miller.[2] The calculations return energy eigenvalues, E_n, and corresponding eigenfunctions, ψ_n, evaluated at points on an equally spaced DVR grid. The Kubo time-correlation function is obtained

$$\widetilde{C}_{xx}(t) = \frac{1}{Z}\sum_{n,m} e^{-\beta E_n}|x_{nm}|^2 \frac{e^{\beta E_{nm}}-1}{\beta E_{nm}}\cos(\omega_{nm}t) \tag{A.1}$$

where

$$x_{nm} = \langle\psi_n|\, x\, |\psi_m\rangle \tag{A.2}$$

and $Z = \sum_n e^{-\beta E_n}$, $E_{nm} = E_n - E_m$ and $\omega_{nm} = E_{nm}/\hbar$.

A.2 Determining the Lagrange Multiplier

Initially a value of 0 is chosen for the Lagrange multiplier Sec.(2.3.3). If the absolute value of the constraint $|g|$ is below that of the tolerance, the constraint is satisfied for that time step and one proceeds to the next time step. If this is not the case, the Lagrange multiplier is updated using Newton-Raphson update formula.

$$\lambda_{n+1} = \lambda_n - \frac{g(t)}{\dot{g}(t)dt} \tag{A.3}$$

where $g(t)$ is the value of the constraint and $\dot{g}(t)$ is the time derivative of the constraint. This procedure is repeated until the absolute value $|g|$ is below that of the

tolerance.

Note that the time step dt is included in the denominator as this speeds up the convergence of the Lagrange multiplier with number of iterations. Calculations were repeated without the time step in the denominator resulted in identical trajectories.

Appendix B

Time-Derivative of the Constant-Uncertainty Constraint

The constraint is of the form

$$g(t) = \left(\left\langle p^2 \right\rangle (t) - (\langle p \rangle (t))^2\right)\left(\left\langle q^2 \right\rangle (t) - (\langle q \rangle (t))^2\right) - (\langle pq \rangle (t) - \langle p \rangle (t) \langle q \rangle (t))^2 \tag{B.1}$$

where we have $g(t) - g(0) = 0$. This is non-linear in p and so cannot be treated by the non-holonomic extension to RATTLE. Splitting up this equation

$$(1) = \left(\left\langle p^2 \right\rangle - \langle p \rangle^2\right) \tag{B.2a}$$

$$(2) = \left(\left\langle q^2 \right\rangle - \langle q \rangle^2\right) \tag{B.2b}$$

$$(3) = (\langle pq \rangle - \langle p \rangle \langle q \rangle)^2 \tag{B.2c}$$

then taking the derivative with respect to time, we get

$$(1)' = \left(\left\langle 2p\frac{\partial p}{\partial t} \right\rangle - 2 \langle p \rangle \left\langle \frac{\partial p}{\partial t} \right\rangle\right) \tag{B.3a}$$

$$(2)' = \left(\left\langle 2q\frac{\partial q}{\partial t} \right\rangle - 2 \langle q \rangle \left\langle \frac{\partial q}{\partial t} \right\rangle\right) \tag{B.3b}$$

$$(3)' = 2\left(\left\langle p\frac{\partial q}{\partial t} \right\rangle + \left\langle q\frac{\partial p}{\partial t} \right\rangle - \langle p \rangle \left\langle \frac{\partial q}{\partial t} \right\rangle - \left\langle \frac{\partial p}{\partial t} \right\rangle \langle q \rangle\right)(\langle pq \rangle - \langle p \rangle \langle q \rangle) \tag{B.3c}$$

where the primes indicate the time derivative. The total derivative can then be written as

$$\frac{dg}{dt} = (1)'(2) + (2)'(1) - (3)' \tag{B.4}$$

which gives

$$\frac{dg}{dt} = \left(\left\langle 2p\frac{\partial p}{\partial t}\right\rangle - 2\left\langle p\right\rangle\left\langle \frac{\partial p}{\partial t}\right\rangle\right)\left(\left\langle q^2\right\rangle - \left\langle q\right\rangle^2\right) + \left(\left\langle 2q\frac{\partial q}{\partial t}\right\rangle - 2\left\langle q\right\rangle\left\langle \frac{\partial q}{\partial t}\right\rangle\right)\left(\left\langle p^2\right\rangle - \left\langle p\right\rangle^2\right) - 2\left(\left\langle p\frac{\partial q}{\partial t}\right\rangle + \left\langle q\frac{\partial p}{\partial t}\right\rangle - \left\langle p\right\rangle\left\langle \frac{\partial q}{\partial t}\right\rangle - \left\langle \frac{\partial p}{\partial t}\right\rangle\left\langle q\right\rangle\right)\left(\left\langle pq\right\rangle - \left\langle p\right\rangle\left\langle q\right\rangle\right) = 0 \tag{B.5}$$

We then note that, assuming that $m = 1$,

$$\left\langle \frac{\partial q}{\partial t}\right\rangle = \left\langle p\right\rangle \tag{B.6}$$

and

$$\left\langle \frac{\partial p}{\partial t}\right\rangle = \left\langle \frac{\partial V}{\partial q}\right\rangle \tag{B.7}$$

This gives

$$\frac{dg}{dt} = 2\left(\left\langle p\frac{\partial V}{\partial q}\right\rangle - \left\langle p\right\rangle\left\langle \frac{\partial V}{\partial q}\right\rangle\right)\left(\left\langle q^2\right\rangle - \left\langle q\right\rangle^2\right) + 2\left(\left\langle qp\right\rangle - \left\langle q\right\rangle\left\langle p\right\rangle\right)\left(\left\langle p^2\right\rangle - \left\langle p\right\rangle^2\right) - 2\left(\left\langle p^2\right\rangle + \left\langle q\frac{\partial V}{\partial q}\right\rangle - \left\langle p\right\rangle^2 - \left\langle \frac{\partial V}{\partial q}\right\rangle\left\langle q\right\rangle\right)\left(\left\langle pq\right\rangle - \left\langle p\right\rangle\left\langle q\right\rangle\right) = 0 \tag{B.8}$$

which simplifies to

$$\frac{dg}{dt} = \left(\left\langle p\frac{\partial V}{\partial q}\right\rangle - \left\langle p\right\rangle\left\langle \frac{\partial V}{\partial q}\right\rangle\right)\left(\left\langle q^2\right\rangle - \left\langle q\right\rangle^2\right) - \left(\left\langle q\frac{\partial V}{\partial q}\right\rangle - \left\langle q\right\rangle\left\langle \frac{\partial V}{\partial q}\right\rangle\right)\left(\left\langle pq\right\rangle - \left\langle p\right\rangle\left\langle q\right\rangle\right) = 0 \tag{B.9}$$

which is the derivative of the constraint given in ref.[85]. This expression is linear in p, since it can be written in the form $\sum_i \mu(q_i)\dot{q}$, with

$$\mu(q_i) = \left(\frac{\partial V}{\partial q_i} - \left\langle \frac{\partial V}{\partial q}\right\rangle\right)\left(\left\langle q^2\right\rangle - \left\langle q\right\rangle^2\right) - \left(\left\langle q\frac{\partial V}{\partial q}\right\rangle - \left\langle q\right\rangle\left\langle \frac{\partial V}{\partial q}\right\rangle\right)\left(q_i - \left\langle q\right\rangle\right) \tag{B.10}$$

and thus can be treated by the non-holonomic extension to RATTLE of ref.[99].

Appendix C

Normal Modes

For the molecular dynamics simulation of a ring polymer consisting of N beads, a transformation can be made from bead positions to normal mode coordinates which describe the collective motion of individual bead coordinates.[73; 110] These normal mode coordinates are linear combinations of individual bead coordinates which make the free-ring polymer hamiltonian diagonal in p and q.

$$T_N(\mathbf{p},\mathbf{x}) = \frac{\mathbf{p}^2}{2m} + \frac{m}{2(\beta_N\hbar)^2}\sum_{i=1}^{N}(q_{i+1} - q_i)^2. \tag{C.1}$$

For odd N, the normal modes are

$$P_n = \sum_{l=1}^{N} T_{ln} p_l \ , \qquad Q_n = \sum_{l=1}^{N} T_{ln} q_l, \qquad n = 0, \pm 1, \ldots, \pm(N-1)/2 \tag{C.2}$$

where

$$T_{ln} = \begin{cases} \sqrt{1/N} & n = 0 \\ \sqrt{2/N}\sin(2\pi ln/N) & n = 1, \ldots, (N-1)/2 \\ \sqrt{2/N}\cos(2\pi ln/N) & n = -1 \ldots, -(N-1)/2 \end{cases} \tag{C.3}$$

The associated normal frequencies are given by

$$\omega_n = \frac{2}{\beta_N\hbar}\sin\left(\frac{n\pi}{N}\right) \tag{C.4}$$

Applying this transformation speeds up the RPMD code for two reasons: first, the updates in the position and momenta of the ring polymer are known analytically in the absence of an external potential; second, the transformation between bead coordinates and normal modes can be made extremely efficient by the use of fast fourier transform routines (FFT) rather than direct matrix multiplication which

reduces the computational expense of the transformation from $\mathcal{O}(N^2)$ operations to $\mathcal{O}(N \log N)$. In addition, working in ring-polymer normal modes is useful because thermostats such as the Langevin thermostat are designed to work in these coordinates.[110]

Appendix D

DVR Interpolation Functions

In the limit that the total number of DVR functions tends to infinity, the wavefunction can simply be constructed as the coefficient of the eigenvector at a particular point i.e. the DVR functions tend towards a dirac delta function centred on a point. However, in practise a finite number of points needs to be used, when this number is small these functions are zero at the other DVR points, however they have non zero amplitude in between these points. For the finite box (with ends at a and b), these functions are:

$$\xi_i(x) = \sqrt{\Delta} \sum_{n=1}^{N-1} \phi_n(x_i)\phi_n(x), \qquad i = 1, ...N-1 \tag{D.1}$$

where

$$\phi_n(x) = \left(\frac{2}{(b-a)}\right)^{1/2} \sin\left[\frac{n\pi(x-a)}{(b-a)}\right] \tag{D.2}$$

$$x_i = a + (b-a)i/N \tag{D.3}$$

$$\Delta = (b-a)/N \tag{D.4}$$

These functions $\xi_i(x)$ have the property that they are orthogonal to each other and look like broadened dirac delta functions centred at the i-th node of all of the others.

$$\int_a^b \xi_i(x)\xi_j(x) = \delta_{ij} \tag{D.5}$$

The wavefunctions can then be constructed as a sum of these functions multiplied by the eigenvector coefficients.

References

[1] D. Frenkel, B. Smit, Understanding Molecular Simulation, San Diego, Academic, 2002.

[2] D. T. Colbert, W. H. Miller, *J. Chem. Phys.* **96** (1992) 1982.

[3] D. C. Clary, *Science* **329** (2008) 789.

[4] J. C. Light, T. Carrington Jr, *Adv. Chem. Phys.* **114** (2000) 263.

[5] J. Tennyson et al., *Comput. Phys. Commun.* **163** (2004) 85.

[6] C. Lanczos, An iteration method for the eigenvalue problem of linear differential and integral operators, United States Government Press Office, Los Angeles, CA, 2059.

[7] H. Liu, Y. Wang, J. M. Bowman, *J. Am. Chem. Soc.* **136** (2014) 5888.

[8] H. Liu, Y. Wang, J. M. Bowman, *J. Phys. Chem.* **118** (2014) 14124.

[9] E. J. Heller, *Acc. Chem. Res.* **39** (2006) 127.

[10] E. J. Heller, *J. Chem. Phys.* **75** (1981) 2923.

[11] D. V. Shalashilin, I. Burghardt, *J. Chem. Phys.* **129** (2008) 084104.

[12] S. Habershon, *J. Chem. Phys.* **136** (2012) 014109.

[13] M. Ben-Nun, J. Quenneville, T. J. Martinez, *J. Chem. Phys.* **104** (2000) 5161.

[14] H. Meyer, U. Manthe, L. Cederbaum, *Chem. Phys. Lett.* **165** (1990) 74.

[15] M. H. Beck, A. Jäckle, G. A. Worth, H.-D. Meyer, *Phys. Rep.* **324** (2000) 1.

[16] G. A. Worth, *Comput. Phys. Commun.* **248** (2020) 107040.

[17] R. P. Feynman, A. R. Hibbs, D. F. Styer, Quantum Mechanics and Path Integrals, Dover, 2010.

[18] D. Chandler, P. G. Wolynes, *J. Chem. Phys.* **74** (1981) 4078.

[19] M. Parrinello, A. Rahman, *J. Chem. Phys.* **80** (1984) 860.

[20] M. Ceriotti et al., *Chem. Rev.* **116** (2016) 7529.

[21] M. Ceriotti, J. Cuny, M. Parrinello, D. E. Manolopoulos, *Proc. Natl. Acad. Sci.* **110** (2013) 15591.

[22] T. E. Markland, D. E. Manolopoulos, *J. Chem. Phys.* **129** (2008) 024105.

[23] T. E. Markland, D. E. Manolopoulos, *Chem. Phys. Lett.* **464** (2008) 256.

[24] M. Ceriotti, D. E. Manolopoulos, M. Parrinello, *J. Chem. Phys.* **134** (2011) 084104.

[25] M. Ceriotti, D. E. Manolopoulos, *Phys. Rev. Lett.* **109** (2012) 100604.

[26] V. Kapil, J. Behler, M. Ceriotti, *J. Chem. Phys.* **145** (2016) 234103.

[27] V. Kapil, J. VandeVondele, M. Ceriotti., *J. Chem. Phys.* **144** (2016) 054111.

[28] J. Liu, *Int. J. Quantum Chem.* **115** (2015) 657.

[29] J. Liu, W. H. Miller, F. Paesani, W. Zhang, D. A. Case, *J. Chem. Phys.* **131** (2009) 164509.

[30] J. Liu, W. H. Miller, G. S. Fanourgakis, S. S. Xantheas, S. Imoto, S. Saito, *J. Chem. Phys.* **135** (2011) 244503.

[31] X. Liu, J. Liu, *Mol. Phys.* **116** (2018) 755.

[32] J. Liu, W. H. Miller, *J. Chem. Phys.* **131** (2009) 074113.

[33] S. Nielsen, R. Kapral, G. Ciccotti, *J. Chem. Phys.* **115** (2001) 6543.

[34] E. Wigner, *Phys. Rev.* **40** (1932) 749.

[35] W. B. Case, *Am. J. Phys.* **76** (2008) 937.

[36] Q. Shi, E. Geva, *J. Chem. Phys.* **118** (2003) 8173.

[37] E. Pollak, J. L. Liao, *J. Chem. Phys.* **108** (1998) 2733.

[38] R. Hernandez, G. A. Voth, *Chem. Phys.* **233** (1998) 243.

[39] J. A. Poulsen, G. Nyman, P. J. Rossky, *J. Chem. Phys.* **119** (2003) 12179.

[40] J. A. Poulsen, G. Nyman, P. J. Rossky, *J. Chem. Theory Comput.* **2** (2006) 1482.

[41] S. Bonella, D. Montemayor, D. F. Coker, *Proc. Natl. Acad. Sci. USA* **102** (2005) 6715.

[42] M. S. Causo, G. Ciccotti, D. Montemayor, S. Bonella, D. F. Coker, *J. Phys. Chem. B* **109** (2005) 6855.

[43] B. Hellsing, S. I. Sawada, H. Metiu, *J. Phys. Condens. Matt.* **122** (1985) 303.

[44] P. Frantsuzov, A. Neumaier, V. A. Mandelshtam, *Chem. Phys. Lett.* **381** (2003) 117.

[45] J. Shao, E. Pollak, *J. Chem. Phys.* **125** (2003) 133502.

[46] R. P. Feynman, H. Kleinert, *Phys. Rev. A* **54** (1986) 5080.

[47] A. Cuccoli, R. Giachetti, V. Tognetti, R. Vaia, P. Verrucchi, *J. Phys. Condens. Matt.* **7** (1995) 7891.

[48] S. Habershon, D. E. Manolopoulos, *J. Chem. Phys.* **131** (2009) 244518.

[49] W. H. Miller, *J. Chem. Phys.* **125** (2006) 132305.

[50] R. L. Benson, G. Trenins, S. C. Althorpe, *Faraday. Discuss.* **221** (2019) 350.

[51] H. Wang, X. Sun, W. H. Miller, *J. Chem. Phys.* **108** (1998) 9726.

[52] X. Sun, H. Wang, W. H. Miller, *J. Chem. Phys.* **109** (1998) 4190.

[53] X. Sun, H. Wang, W. H. Miller, *J. Chem. Phys.* **109** (1998) 7064.

[54] W. H. Miller, *J. Chem. Phys. A* **105** (2001) 2942.

[55] I. R. Craig, D. E. Manolopoulos, *J. Chem. Phys.* **121** (2004) 3368.

[56] I. R. Craig, D. E. Manolopoulos, *J. Chem. Phys.* **122** (2005) 084106.

[57] I. R. Craig, D. E. Manolopoulos, *J. Chem. Phys.* **121** (2005) 034102.

[58] S. Habershon, G. S. Fanourgakis, D. E. Manolopoulos, *J. Chem. Phys.* **129** (2008) 074501.

[59] S. Habershon, T. E. Markland, D. E. Manolopoulos, *J. Chem. Phys.* **131** (2009) 024501.

[60] N. Boekelheide, R. Salomon-Ferrer, T. F. Miller, *Proc. Natl. Acad. Sci.* **108** (2011) 16159.

[61] J. B. Rommel, T. P. M. Goumans, J. Kästner, *J. Chem. Theory Comput.* **7** (2011) 690.

[62] S. Habershon, D. E. Manolopoulos, T. E. Markland, T. F. Miller, *Annu. Rev. Phys. Chem.* **64** (2013) 387.

[63] M. Rossi, M. Ceriotti, D. E. Manolopoulos, *J. Chem. Phys.* **140** (2014) 234116.

[64] M. Rossi, H. Liu, F. Paesani, J. Bowman, M. Ceriotti, *J. Chem. Phys.* **141** (2013) 181101.

[65] G. R. Medders, F. Paesani, *J. Chem. Theory Comput.* **11** (2015) 1145.

[66] S. C. Althorpe et al., *Faraday Discuss.* **195** (2016) 671.

[67] Y. V. Suleimanov, F. J. Aoiz, H. Guo, *J. Phys. Chem. A* **120** (2016) 8488.

[68] S. K. Reddy, D. R. Moberg, S. C. Straight, F. Paesani, *J. Chem. Phys.* **147** (2017) 244504.

[69] B. Cheng, E. A. Engel, J. Behler, C. Dellago, M. Ceriotti, *Proc. Natl. Acad. Sci.* **116** (2019) 1110.

[70] S. Jang, G. A. Voth, *J. Chem. Phys.* **111** (1999) 2371.

[71] J. Cao, G. A. Voth, *J. Chem. Phys.* **100** (1994) 5106.

[72] S. Habershon, D. E. Manolopoulos, T. E. Markand, T. F. Miller, *Annu. Rev. Phys. Chem.* **64** (2013) 387.

[73] T. J. H. Hele, M. J. Willatt, A. Muolo, S. C. Althorpe, *J. Chem. Phys.* **142** (2015) 134103.

[74] T. J. H. Hele, *Mol. Phys.* **115** (2017) 1435.

[75] T. J. H. Hele, M. J. Willatt, A. Muolo, S. C. Althorpe, *J. Chem. Phys.* **142** (2015) 191101.

[76] M. J. Willatt, Matsubara Dynamics and its Practical Implementation, PhD Thesis, University of Cambridge, 2017.

[77] M. J. Willatt, M. Ceriotti, S. C. Althorpe, *J. Chem. Phys.* **148** (2018) 102336.

[78] G. Trenins, S. C. Althorpe, *J. Chem. Phys.* **149** (2018) 014102.

[79] G. Trenins, M. J. Willatt, S. C. Althorpe, *J. Chem. Phys.* **151** (2019) 054109.

[80] A. Horikoshi, K. Kinugawa, *J. Chem. Phys.* **122** (2005) 174104.

[81] T. J. H. Hele, *Mol. Phys.* **114** (2016) 1461.

[82] A. Witt, S. D. Ivanov, M. Shiga, H. Forbert, D. Marx, *J. Chem. Phys.* **130** (2009) 194510.

[83] S. D. Ivanov, A. Witt, M. Shiga, D. Marx, *J. Chem. Phys.* **132** (2010) 031101.

[84] G. Trenins, Quasi Centroid Molecular Dynamics, PhD Thesis, University of Cambridge, 2020.

[85] T. Hasegawa, *J. Chem. Phys.* **145** (2016) 171101.

[86] J. O. Richardson, Ring Polymer Approaches to Instanton Theory, PhD Thesis, University of Cambridge, 2012.

[87] I. Craig, D. E. Manolopoulos, *J. Chem. Phys.* **122** (2005) 084106.

[88] R. Nityananda, *Resonance* **4** (1999) 24.

[89] H. C. Andersen, *J. Comput. Phys.* **52** (1983) 24.

[90] D. J. Evans, W. G. Hoover, B. H. Failor, B. Moran, A. J. C. Ladd, *Phys. Rev. A.* **28** (1983) 1016.

[91] H. Hiscock, Approximating quantum dynamics using classical simulations, Part III thesis, University of Cambridge, 2014.

[92] D. M. Ceperley, *Rev. Mod. Phys.* **67** (1995) 279.

[93] M. F. Herman, E. J. Bruskin, B. J. Berne, *J. Chem. Phys.* **76** (1982) 5150.

[94] M. Tuckerman, Statistical Mechanics: Theory and Molecular Simulation, Oxford University Press, 2010.

[95] J.-P. Ryckaert, G. Ciccotti, H. J. C. Berendsen, *J. Comput. Phys.* **23** (1977) 327.

[96] T. Stecher, Benchmark Studies of Ring-Polymer Molecular Dynamics Rate Theory, PhD Thesis, University of Cambridge, 2010.

[97] W. G. Hoover, A. J. C. Ladd, B. Moran, *Phys. Rev. Lett.* **48** (1982) 1818.

[98] A. M. Bloch, Nonholonomic mechanics and control, Springer New York, 2003.

[99] S. Ferraro, D. Iglesias-Ponte, D. M. D. Diego, *Discrete. Contin. Dyn. Syst. Supplement* (2009) 220.

[100] R. McLachlan, M. Perlmutter, *J. Nonlinear Sci.* **16** (2006) 283.

[101] M. Hillery, R. F. Connell, M. O. Scully, E. P. Wigner, *Phys. Rep.* **106** (1984) 121.

[102] T. J. H. Hele, S. C. Althorpe, *J. Chem. Phys.* **138** (2013) 084108.

[103] D. A. Case et al., *J. Comput. Chem.* **26** (2005) 1668.

[104] Q. Shi, E. Geva, *J. Phys. Chem. A* **107** (2003) 9059.

[105] 2D implementation of the LGA provided by R. Benson which was modified for the calculation of the FHA 2D results.

[106] S. C. Althorpe, Personal communication (2020).

[107] G. R. Medders, F. Paesani, *J. Chem. Theory. Comput.* **11** (2015) 1145.

[108] QCMD data for the Champagne-bottle Morse potential provided by S. C. Althorpe. (2020).

[109] QCMD PMF data provided by C. Haggard. (2020).

[110] M. Ceriotti, M. Parrinello, T. E. Markland, D. E. Manolopoulos, *J. Chem. Phys.* **133** (2010) 124104.